Title
MOCVD Growth and Loss Optimization for Tunnel Junction Contacts for III-Nitride Laser Diodes

Author
Hamdy, Shereen

Publication Date
2021

UNIVERSITY OF CALIFORNIA

Santa Barbara

MOCVD Growth and Loss Optimization for Tunnel Junction Contacts for III-Nitride Laser Diodes

A dissertation submitted in partial satisfaction
of the requirements for the degree

Doctor of Philosophy
in
Electrical and Computer Engineering

by

Shereen W. Hamdy

Committee in charge:

Professor Shuji Nakamura, Chair
Professor Steven P. DenBaars
Professor James S. Speck
Professor Umesh K. Mishra

December 2021

The dissertation of Shereen W. Hamdy is approved.

Professor Steven P. DenBaars

Professor James S. Speck

Professor Umesh K. Mishra

Professor Shuji Nakamura, Committee Chair

November 2021

MOCVD Growth and Loss Optimization for Tunnel Junction Contacts for III-Nitride Laser Diodes

by

Shereen W. Hamdy

Acknowledgements

I would like to begin my acknowledgements by thanking my advisor, Prof. Shuji Nakamura, for inviting me to join his research group, for introducing me both to the Nitrides field and my first mentors here, and for always being available to respond to emails and to meet, however small the question. Thank you also to my committee: Prof. Steve DenBaars, for always knowing of a helpful book or paper or solution for the research question at hand; Prof. Jim Speck, for all of the in-depth discussions and career advice; Prof. Umesh Mishra, who elevated my understanding of semiconductor devices more than I knew was possible. I am a better scientist thanks to the interactions that I had with each of my committee members, and I am grateful for all of the opportunities and experiences over the years.

Thanks also to the administrative staff at SSLEEC and the ECE and Materials Departments, whose work is vital to more or less everything else that happens here. I am grateful to have variously worked with and received administrative support from Tara, Yukina, Fukiko, Emi, and Tal at SSLEEC, and from Val at the ECE Department, in my time at UCSB.

I cannot sufficiently express my thanks to Michael Iza, Stacia Keller, David Whitlatch, and Brian Carralejo at the MOCVD lab; Tom Mates, Youli Lee, and Miguel Zepeda-Rosales at the CNSI/MRL facilities; Demis John and Brian Thibeault and all of the rest of the staff at the cleanroom. So many projects would not have been remotely possible without their patient and consistent support of countless pieces of equipment in labs all over campus.

Science is a fundamentally communal activity, and in this light this work would not have been possible without the many mentors and peers I met here. I want to thank Dan Becerra and Ben Yonkee for teaching me a full suite of crystal growth and nanofabrication skills, as well as Erin Young, Abdullah Alhassan, and Shlomo Mehari for all of the collaborations and discussions. I particularly want to thank Dan Cohen for so much invaluable feedback and guidance over the course of my time here, both in group meetings and in the one-on-one meetings for which he would always find the time. Philip, Joonho, Jianfeng, Ryan, Nate, Haojun, Arwa, and so many others not mentioned here have also all given my research a helping hand or a needed perspective at one point or another. So often, I found myself feeling stuck or confused about my project - and then one of the people named here would simply ask how my research was going, and we would talk, and I would find my work moving again soon afterwards. Thanks, all of you.

In my time at UCSB, when I was not in the lab I was often organizing or teaching for one science outreach event or another. These events were almost all with the Photonics Society at UCSB and/or the Center for Science and Engineering Partnerships at CNSI, and I left every one feeling fulfilled and whole. Thank you to Wendy Ibsen and Carli Ruskauff and everyone else at CSEP involved in putting together so many FUSE nights and SST classes and other outreach events that we did together. Thanks to Marilyn Garza at SBUSD for her collaboration with and support of our outreach work, and thanks again to Yukina for the outreach opportunities over the years. Thank you to everyone with whom I got to work through the Photonics Society at UCSB: Takako, Victoria, Philip, Warren, Demis, Andy, Caroline, and too many more names to name. I have heard it said a few times that one does not fully understand their work until they have to teach the subject matter to someone outside their field, and so I am profoundly grateful to all of you for both the professional development and the personal fulfillment.

To Airlia, (Jared) Claypoole, Caroline, Léa, Mike, Shana, David Z., Arwa, Ashima, Nioshi, Mimi, everyone I met at LP, everyone I lived with at QT Castle - I am lucky to know you, and I will always be grateful for your friendship.

These acknowledgements would not be complete if I did not thank my parents, without whose encouragement I would not have completed this degree, and my younger siblings, who never let me take myself too seriously nor let me feel too alone.

Thank you to my Kakima and Kaku for being a welcoming and loving presence in my life for as long as I have known them.

I cannot fathom how I would have made it through the trials of the last six and some years of grad school and life had Pratiti not been there to unconditionally support me through them, nor can I imagine care any more thoughtful and patient than what I received (and continue to receive) from her. One day soon it will be my turn to do the supporting and hers to do the dissertation-writing, and I hope I can do even half the job that she did. To my found family, my proudest supporter, my best friend - thank you.

Curriculum Vitæ
Shereen W. Hamdy

Education

2021	Ph.D. in Electrical and Computer Engineering, University of California, Santa Barbara.
2017	M.S. in Electrical and Computer Engineering, University of California, Santa Barbara.
2015	B.S. in Engineering Physics (*magna cum laude*), Cornell University

Publications

2021	**Designs for III-Nitride Edge-Emitting Laser Diodes with Tunnel Junction Contacts for Low Internal Optical Absorption Loss** S. W. Hamdy, S. P. DenBaars, J. S. Speck, S. Nakamura Submitted.
2019	**Light-based educational outreach activities for pre-university students** S. W. Hamdy, T. Hirokawa, P. Chan, W. Jin, V. M. Rosborough, E. J. Stanton, A. Netherton, M. Garza, W. Ibsen, D. D. John, J. E. Bowers Proceedings Volume 11143, Fifteenth Conference on Education and Training in Optics and Photonics: ETOP 2019; 111432R (2019).
2019	**Efficient tunnel junction contacts for high-power semipolar III-nitride edge-emitting laser diodes** S. W. Hamdy, E. C. Young, A. I. Alhassan, D. L. Becerra, S. P. DenBaars, J. S. Speck, S. Nakamura Optics Express **27** 8327-8334 (2019).

Conference Presentations

2019	**Light-based educational outreach activities for pre-university students** S. W. Hamdy, T. Hirokawa, P. Chan, W. Jin, V. M. Rosborough, E. J. Stanton, A. Netherton, M. Garza, W. Ibsen, D. D. John, J. E. Bowers Fifteenth Conference on Education and Training in Optics and Photonics (ETOP 2019), 2019, Quebec City, Quebec, Canada.

2018 **High-Efficiency Tunnel Junction Contacts for High-Power III-Nitride Edge-Emitting Laser Diodes**
S. W. Hamdy, E. C. Young, A. I. Alhassan, D. L. Becerra, S. P. DenBaars, J. S. Speck, S. Nakamura
International Workshop on Nitride Semiconductors 2018 (IWN 2018), 2018, Kanazawa, Japan.

Research Experience

2016 – 2021 **NSF Graduate Research Fellow, Nakamura Research Group, UC Santa Barbara, Santa Barbara, CA**
Tunnel junction contacts for III-Nitride semipolar laser diodes. MOCVD crystal growth, cleanroom nanofabrication, and electrical, optical, and compositional characterization of devices. Modeled absorption loss, band structure, and distributed feedback grating designs.

Summers 2015, 2016 **Engineering Intern, Xallent LLC, Ithaca, NY**
Design and implementation of control software for scanning tunneling microscope systems.

Summers 2013, 2014 **Engineering Intern, Qualcomm, San Diego, CA**
Simulation, testing, optimization of novel analog electronic circuits for communication and wireless power delivery.

Education and Teaching Experience

Jan. 2018 – Nov. 2019 **Educational Outreach Chair, Photonics Society at UCSB, UC Santa Barbara, Santa Barbara, CA**
Coordinated programming, volunteers, activities, promotion for educational outreach events. 30+ events held; est. 1000+ community members impacted; two grants awarded; collaborated with five local organizations. Organized Women in Photonics 2018 and 2019: outreach activities, career talks, lab tours, faculty and industry talks.

Winter, Fall 2017 **Co-instructor, School for Scientific Thought, Center for Science and Engineering Partnerships, UC Santa Barbara, Santa Barbara, CA**
Designed curriculum, lesson plans for high-school-level hands-on activities on the science of light. Taught ten two-hour lessons.

Fall 2015 **Teaching Assistant, UC Santa Barbara, Santa Barbara, CA**
Upper-level electricity and magnetism course. Held discussions and office hours, graded homework and exams, wrote solution sets.

Spring 2015 **Teaching Assistant, Cornell University, Ithaca, NY**
Senior-level fluid dynamics course. Held all discussions and office hours, graded all homework and exams, wrote all solution sets.

Abstract

MOCVD Growth and Loss Optimization for Tunnel Junction Contacts for III-Nitride Laser Diodes

by

Shereen W. Hamdy

The III-Nitride edge-emitting laser diode (LD) shows promise in diverse applications such as directed illumination e.g. automotive and spot lighting, communication e.g. Li-Fi communication, fundamental science, and others. While significant recent progress has been made in improving the efficiency of the III-Nitride edge-emitting LD, continuing progress must be made for it to become and remain competitive in these applications. The tunnel junction (TJ) presents unique design opportunities for many III-Nitride devices, including in edge-emitting LDs where it is most often used as a substitute p-side contact that in principle allows p-type material on one side of the TJ to be replaced with less absorbing and more conductive n-type material on the other side. However, the TJ presents challenges in p-type GaN activation, where typical metal-organic chemical vapor deposition (MOCVD) growth conditions are known to introduce hydrogen and re-passivate p-type material. The TJ presents additional challenges in absorption, where the highly-doped layers of the TJ can contribute significant optical absorption loss to LDs, reducing device efficiencies. Both of these challenges must be addressed for the tunnel junction to be a part of viable III-Nitride edge-emitting LD designs.

In this work, we demonstrate high-power LDs using TJ contacts grown by molecular beam epitaxy (MBE), which preserves p-GaN activation, and we also demonstrate LDs using TJ contacts grown by MOCVD that employ a p-GaN activation scheme utilizing lateral diffusion of hydrogen through the LD ridge sidewalls. Next, we model the lasing mode and internal optical absorption loss profiles of III-Nitride edge-emitting LD designs using the transfer matrix method and identify new designs showing reduced modeled internal optical absorption loss in III-Nitride edge-emitting LDs using TJ contacts. Last, LDs using TJ contacts and distributed feedback (DFB) gratings in tandem are designed and evaluated in a joint film mode matching-analytical model, showing the tunnel junction facilitates DFB LD designs with higher-order gratings, benefiting fabrication tolerances and complexity.

Contents

Chapter 1

Introduction

1.1 Introduction to the III-Nitride Materials System

The group III-Nitride semiconductor materials system is famed for its unique range of direct energy bandgaps that correspond to wavelengths of light spanning infrared wavelengths through the full visible range and into ultraviolet wavelengths. Especially notable is that the III-Nitride system is also known as the material system enabling highly efficient visible-light LED solid-state lighting technologies that greatly improve upon the energy efficiencies of previously available technologies in illumination. These energy efficiencies are referred to here as power conversion efficiencies or wall-plug efficiencies.

Since the demonstration of the first efficient III-Nitride LEDs in 1991 [1], additional light-emitting devices have been demonstrated on the III-N materials system. These include additional LED devices like the micro-LED, the ultraviolet LED, and the superluminescent LED, as well as laser devices like the edge-emitting laser diode, the distributed feedback laser diode, and the vertical cavity surface-emitting laser (or VCSEL). The realization of these new devices has enabled improved energy efficiency for an increasing number of applications including general illumination, automotive illumination, spot lighting, displays and projectors, free-space Li-Fi communications, medical imaging, ultraviolet disinfection, and fundamental scientific research.

Room for improvement in device efficiency remains, however. Semiconductor devices generally require both p-type doped material and n-type doped material in order to function. Because of the high activation energy of Magnesium dopant impurities used to form p-type III-N material, p-type GaN is a material that is relatively resistive to electrical conduction [2], and at the high doping levels required to reach acceptable conductivity properties, the contribution of p-type GaN to optical absorption losses becomes significant [3], reducing device efficiency. This is especially concerning in laser diodes where optical gain must match the total internal optical absorption loss for appreciable emission of laser light to occur.

The tunnel junction was first demonstrated in 1958 by Esaki *et al.* [4]. In the III-Nitride materials system, the tunnel junction has often been used where materials with better conduction properties and lower optical absorption losses are needed. Tunnel junctions are typically formed when highly doped n-type material is formed on highly doped p-type material. In the resulting energy band structure, conduction may be achieved through electron tunneling from the valence band of the p-type material into the conduction band of the n-type material. In this way, tunnel junctions provide an additional interface between p-type GaN and n-type GaN and so can facilitate replacement of p-type GaN with n-type GaN, which has superior conduction and absorption properties. Proper utilization of the tunnel junction therefore has potential to lead to significant improvements in performance and efficiency for many device types. Use of tunnel junctions can also augment the performance of existing devices by facilitating novel designs that may yield additional improvements to efficiency. Tunnel junction contacts have been used to assist with current spreading [5] and mirror design [6] in LEDs, with current spreading [7] and current confinement [8] in micro LEDs, with current spreading and grating formation in distributed feedback laser diodes [9], and for current aperture definition [10] and loss reduction [11] in VCSELs. Tunnel junction contacts have also been demonstrated in III-Nitride LDs [12, 13, 14], facilitating novel LD devices as well. Some such devices have been realized, e.g. LDs with cascaded active regions [15], off-ridge topside contacts [16], and p-side-down devices [17].

This dissertation presents three studies that advance III-Nitride laser diode research using the tunnel junction contact. Chapter 1 “sets the table” for the rest of the dissertation by laying out key concepts and motivations for III-N tunnel junction research, describing how tunnel junctions and laser diodes are made, and giving a history of III-N tunnel junction research up to the present. Chapter 1 is intended to be relatively accessible to those who are new to and/or come from outside of this field. Chapter 2 describes a study in which edge-emitting laser diodes with tunnel junction contacts are fabricated and characterized, including one set of laser diodes utilizing, for the first time, tunnel junction contacts formed using metal-organic chemical vapor deposition (MOCVD), i.e. the same crystal growth technology used to form the rest of the laser diode epitaxial stack in that study. In Chapter 3, the flexibility introduced by the tunnel junction is used to identify and model LDs that utilize tunnel junction contacts to minimize optical absorption losses, and in Chapter 4, the tunnel junction is used in another modeling study where certain designs for laser diodes with distributed feedback gratings show emergent benefits from the combination of the tunnel junction and distributed feedback grating. Last, chapter 5 ties together these studies, offering insights and an outlook for future efficiency improvements and III-N tunnel junction research. Parts of this dissertation have appeared in two papers: (1) “Efficient tunnel junction contacts for high-power semipolar III-nitride edge-emitting laser diodes,” by Shereen W. Hamdy, Erin C. Young, Abdullah I. Alhassan, Daniel L. Becerra, Steven P. DenBaars, James S. Speck, and Shuji Nakamura, Opt. Express **27**, 8327-8334 (2019); (2) “Designs for III-Nitride Edge-Emitting Laser

Diodes with Tunnel Junction Contacts for Low Internal Optical Absorption Loss" by Shereen W. Hamdy, Steven P. DenBaars, James S. Speck, and Shuji Nakamura, at time of writing submitted on September 30, 2021 to the SPIE journal *Optical Engineering*.

1.2 III-Nitride Laser Diodes

This section of the introduction provides a motivation for III-Nitride LD research, followed by a generally accessible introduction to the physics of semiconductor laser diodes and III-Nitride laser diodes as background to the sections that follow.

1.2.1 Motivations for III-Nitride Laser Diode Research

While the III-Nitride LED represents a leap in energy efficiency over previous lighting technologies, it still possesses the fundamental material limitation of efficiency droop. Efficiency droop, attributed in 2013 to Auger recombination [18], occurs in LEDs at high current densities where high carrier densities facilitate increased Auger nonradiative recombination events, reducing the rate of radiative recombination events and in turn reducing the associated radiative efficiency.

First demonstrated in 1996 [19], the III-Nitride edge-emitting laser diode (LD) provides a workaround to the problem of efficiency droop: in LDs, at lasing threshold, carrier density clamps, and so Auger recombination and other nonradiative processes also clamp at threshold levels while light output power increases continuously with input power (up to the thermal limits of the LD at which point peak gain in the device falls with increasing temperature, degrading LD performance with increasing input power). This allows LDs to achieve power densities much higher than are achievable in LEDs, with one edge-emitting LD able to match the light output of multiple LEDs running at lower individual power to avoid efficiency droop [20]. This yields cost savings associated with reduced chip area per fully packaged device and so makes III-Nitride LDs a promising candidate for commercial applications [18, 19, 21].

Because of their highly directional, high-intensity output, III-Nitride LDs are ideal for applications in which these properties are useful, for instance automotive lighting, projection displays, and spot lighting. High-speed modulation of III-Nitride LDs has also been demonstrated [22], showing suitability for high-speed communication including free-space Li-Fi communication technologies. III-Nitride LDs also show potential for high-efficiency general illumination, particularly street illumination where the directionality of emitted light may help reduce light pollution relative to LEDs and other implementations that emit light over a broader area. Last, because of the collimated, narrow-linewidth emission characteristic of the stimulated emission that drives laser light output, III-Nitride LDs, particularly distributed feedback LDs, are also likely to have applications in scientific research.

1.2.2 Basics of Semiconductor Laser Diode Operation

To provide a foundation for understanding III-Nitride LD operation and efficiency, we discuss in this section general semiconductor laser diode operation and review the constituent parts of a semiconductor laser diode. A visual aid for the following discussion of LD operation is provided in Figure 1.1. Ref. [23] provides an in-depth, comprehensive discussion of semiconductor laser operation.

Laser operation can be very simply understood as:

1. a balance of related processes occurring within an optical cavity (i.e., a confined space, often in the shape of a rectangular bar, bounded by reflective mirrors),

2. where these processes contribute to or diminish from an optical standing wave also known as the lasing mode (i.e., a stationary or “trapped” wave of light),

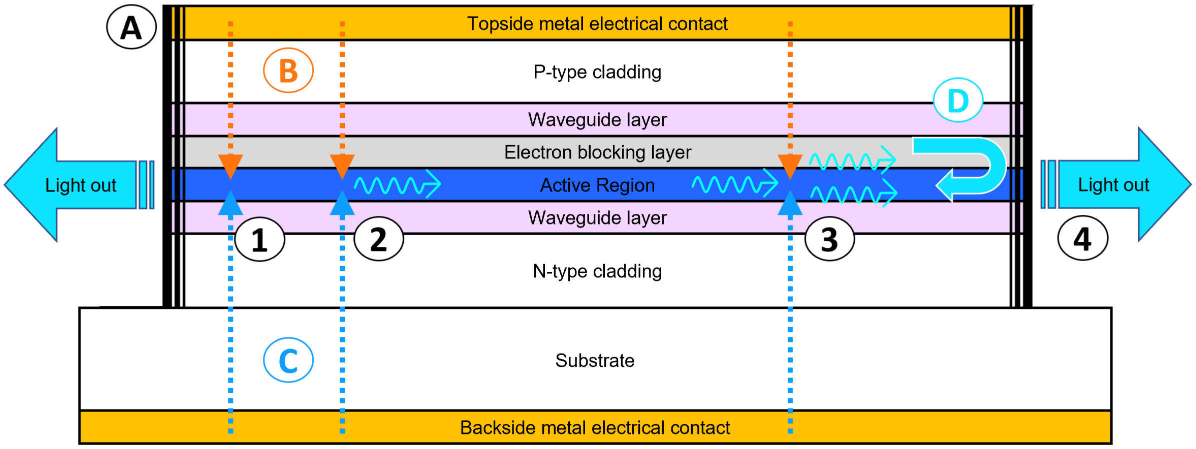

Figure 1.1: Simplified schematic two-dimensional representation of a semiconductor laser diode, showing a cross-section along the length of the laser diode bar (see Figure 1.8a). Annotations, labeled 1-4 and A-D, are discussed in subsection 1.2.2.

3. where the optical cavity also contains a gain medium (put simply, a material with the property of multiplying photons in the presence of a sufficient number of photons, in other words amplifying a wave of light).

Power may be supplied electrically (as is done/assumed for all LDs fabricated and/or modeled in this dissertation) or optically (e.g. by another laser emitting at an optical energy greater than the energy to be emitted by the laser of interest).

One principal feature of III-Nitride materials and semiconductor materials in general is the characteristic gap in allowed energy states for electrons, referred to as the band gap, which arises from quantum mechanical behavior of electrons in a crystal lattice in some materials. The set of energy states below the gap is referred to as the valence band and the set above the gap is referred to the conduction band. Electrons at energy states in the conduction band (often referred to as just electrons) and electron energy state vacancies in the valence band (often referred to as holes) are both collectively referred to as charge carriers. Electron transport can be said to dominate electrical conduction in n-type material, in which a dopant impurity contributes an extra electron per atom to the conduction band; hole transport dominates electrical conduction in p-type material, in which a dopant impurity accepts one electron per atom from the valence band. In LED and LD operation, application of a voltage across the device causes electrons and holes to converge in the active region, where they may radiatively recombine, i.e., an electron undergoes an energy transition across the set of forbidden energy states from an initial energy state in the conduction band to an energy state vacancy in the valence band. The energy difference is then released as a photon, which has an energy determined by the size of the band gap at the location the electron makes its energy transition. A visual diagram of the energy states in a PIN diode under no electrical bias is provided in Figure 1.2a, and a visual diagram of the energy states under forward bias (i.e. the device is turned on) is provided in Figure 1.2b.

Some common constituent parts of a semiconductor laser diode are:

- Topside metal electrical contact: This provides electrical access to the device i.e. helps to spread electrical current across the device area. If well-constructed, it also contributes relatively little resistance to electrical conduction through the device, helping overall efficiency.

- P-type cladding: Forward bias conduction in p-type material is dominated by valence band holes, and so the p-type cladding enables hole transport to the active region for the purpose of radiatively recombining with conduction band electrons.

- Waveguide layer: Also known as a separate confinement heterostructure (SCH) layer, this layer uses a material with a lower refractive index than most of the rest of the LD to help confine photons closer to the active region to facilitate stimulated emission events. In the LDs fabricated and modeled in this work, waveguide layers are located above and below the active region.

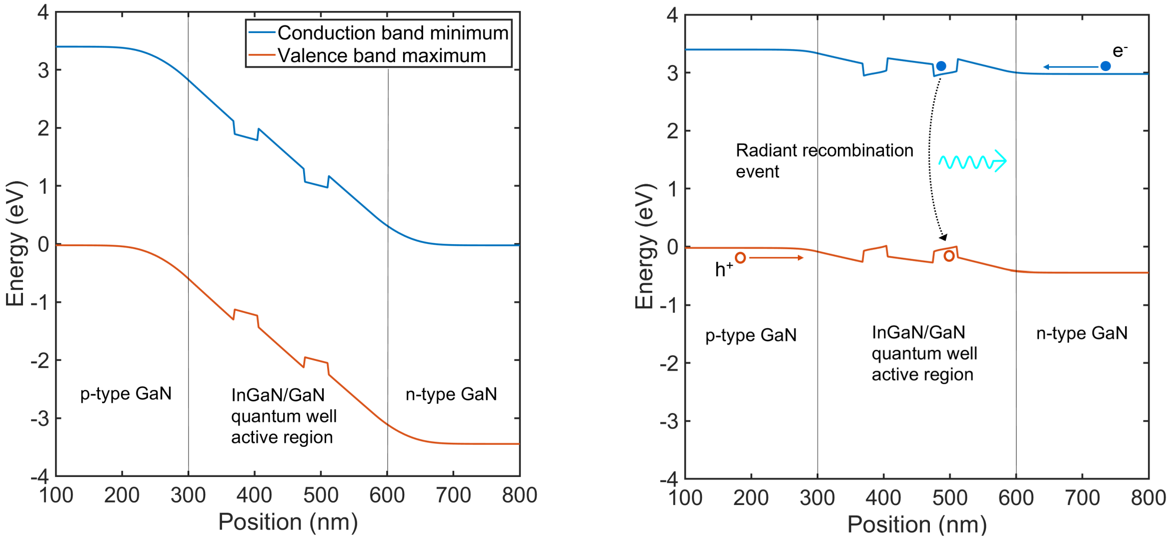

(a) (b)

Figure 1.2: Schematic representation of the energy levels (i.e. energy band diagram) of a simplified III-Nitride light-emitting device: (a) in equilibrium with no voltage applied; drift current caused by the energy topography (electrons in the conduction band move downwards, left to right; holes in the valence band move upwards, right to left) is balanced by diffusion of electrons and holes in their respective opposite directions. (b) with an applied voltage such that electrons (e^-) and holes (h^+) may recombine in the active region, as annotated over the graph. The energy barriers to diffusion for electrons and holes are lowered by the applied voltage, permitting an increased diffusion current of electrons from the electron-rich n-type material towards the active region and an increased diffusion current of holes from the hole-rich p-type material towards the active region, facilitating radiative recombination events.

- Electron blocking layer: In III-Nitride materials, orming a thin alloyed layer of AlGaN just above the active region presents an energy barrier to electrons that may otherwise overshoot the active region, improving injection efficiency i.e. the efficiency with which electrical current becomes charge carriers that reach the active region.

- Active region: The region where electrons and holes recombine to emit light. Radiative recombination may be facilitated through use of quantum wells, which are thin layers of smaller bandgap that create a well-like structure in the band diagram as seen in Figure 1.2. This well helps confine electrons and holes, facilitating radiative recombination events. Its depth, i.e. the size of the energy band gap in the well, corresponds to the wavelength of light to be emitted, and may be tuned by adjusting the alloy composition. The active region also provides a gain medium at the emission wavelength such that stimulated emission events (described below) may occur. The III-Nitride active region is a site of ongoing study and optimization [24, 25].

- N-type cladding: Forward bias conduction in n-type material is dominated by conduction band electrons, and so the n-type cladding contributes these electrons to the active region for the purpose of radiatively recombining with holes in the valence band.
- Substrate: The starting material on which crystal growth occurs. In the III-Nitrides, this may be sapphire i.e. Al_2O_3, freestanding GaN, SiC, or other materials. In this dissertation, the substrate generally is or is assumed to be freestanding semipolar $(20\bar{2}\bar{1})$ GaN.
- Backside metal electrical contact: As with the topside electrical contact, this allows electrical access to the device, completing the path for electrical current through the epitaxial structure while ideally contributing relatively little resistance to conduction through the device.
- Mirrors: Strictly speaking, this refers to the interface at the ends of the laser bar i.e. the interface between III-N material and air. Mirrors may be fabricated through dry etch processes, physical dicing and polishing, or cleaving along a crystal plane. The crystal structure of semipolar $(20\bar{2}\bar{1})$ oriented GaN does not provide an accessible plane for cleaving, and so LD facets on semipolar III-Nitride crystal planes are

generally formed through dry etching or dicing and polishing [26, 27].

Turning our attention to the processes that occur in the semiconductor LD, the first set of these processes that we consider are those that generate light in contribution to, or diminish light from, a standing wave in this optical cavity:

- Charge carrier transport: A prerequisite step to light emission. Hole transport that leads to emission is dominated by diffusion towards the active region from the p-type material, and electron transport that contributes to emission is dominated by diffusion towards the active region from the n-type material. Hole and electron transport are respectively represented by processes B and C in Figure 1.1.

- Spontaneous emission: The primary mechanism for light emission in LEDs. In LDs, spontaneously emitted light may or may not contribute to the optical standing wave that makes up the lasing mode. Represented by process 2 in Figure 1.1.

- Stimulated emission: The main mechanism for light emission in lasers, and the function of the gain medium. In a stimulated emission event, a passing optical wave causes an electron and hole to recombine, producing an additional photon that is in phase with the original wave. When the concentration of photons becomes high enough that stimulated emission events balance the optical loss mechanisms in the laser (lasing threshold), stimulated emission becomes the dominant recombination process for all additional electrons and holes, while other processes no longer increase with increased input power (i.e., they clamp at threshold). In Figure 1.1, stimulated emission is represented by process 3.

- At the mirrors (labeled A in Figure 1.1), generated photons may be reflected back into the cavity, maintaining the optical standing wave (process D in Figure 1.1), or they may exit the cavity (process 4 in Figure 1.1), contributing to emitted laser light but also diminishing from the optical standing wave. Light may escape in equal amounts at both sides of the laser, or high-reflection and/or anti-reflection facet coatings may be used to bias emission towards one facet.

- Emitted photons may be absorbed by material in the LD cavity before they may be emitted at the mirrors, unproductively diminishing the optical standing wave, i.e., the photon is lost to internal optical absorption. Generally, internal optical absorption losses are a bigger problem for more conductive materials such as metals and TCOs, as well as highly doped semiconductor layers. The optical standing wave typically has its greatest intensity at the active region, and so materials close to the active region generally have a significantly greater influence on the total internal optical absorption loss.

Other processes take place in which the input electrical energy fails to generate light in contribution with the lasing mode:

- Electrons and holes may recombine in a nonradiative process that does not emit light. Often this is assisted by a “trap” energy state, located within the band gap, into which conduction band electrons and valence band holes may fall, where this trap state is typically associated with an impurity atomic species in the crystal. Defects in the crystal structure may also contribute to nonradiative recombination processes.

- Other times, the excess energy from a recombination event excites another carrier instead of to optical emission, and this is termed Auger recombination. Auger recombination has been shown to be the dominant process behind LED droop [18], where at sufficiently high input current density, LED power conversion efficiency begins to drop. In LDs, droop clamps at threshold and so does not diminish efficiency in LDs as it does in LEDs.

Nonradiative processes are represented by process 1 in Figure 1.1.

1.2.3 Efficiency of the III-Nitride Laser Diode

While much progress has been made to advance III-Nitride LD power conversion efficiencies (PCEs) [28, 29], i.e. light output power relative to electrical input power, PCEs in LDs remain short of what is necessary for LDs to be competitive with LEDs in applications like illumination, while other technologies like the III-Nitride distributed feedback LD are also still in a developing stage towards commercial viability. This motivates research into improving the power conversion efficiency, or PCE, of the III-Nitride LD.

Having identified PCE as one limiting factor to the III-Nitride LD's commercial viability, we review below the components of PCE relevant to LD analysis and research. In LDs, PCE can be defined and subsequently broken down into components as described below:

$$\mathrm{PCE} = \frac{\text{light power out}}{\text{electrical power in}} = \frac{L_{\mathrm{out}}}{I_{\mathrm{in}} V_{\mathrm{in}}} \tag{1.1}$$

$$\mathrm{PCE} = \eta_{\mathrm{th}} \eta_d \eta_v = \left(\frac{I_{\mathrm{in}} - I_{\mathrm{th}}}{I_{\mathrm{in}}} \right) \left(\eta_i \frac{\alpha_m}{\alpha_i + \alpha_m} \right) \left(\frac{V_{\mathrm{phot.}}}{V_{\mathrm{in}}} \right) \tag{1.2}$$

where L_{out} represents the output optical power and $I_{\mathrm{in}} V_{\mathrm{in}}$ represents the product of the device terminal current and voltage, i.e., the input electrical power. That is, maximizing LD efficiency entails maximizing the output optical power L_{out} and minimizing the input electrical current I_{in} and voltage V_{in}. It is common for analyses to consider L_{out} and V_{out} data as a dependent function of corresponding I_{in} data. A typical plot visualizing this analysis, referred to here as a light-current-voltage or LIV plot, is shown in Figure 1.3.

The PCE of an LD can also be broken down into three efficiency components, as in

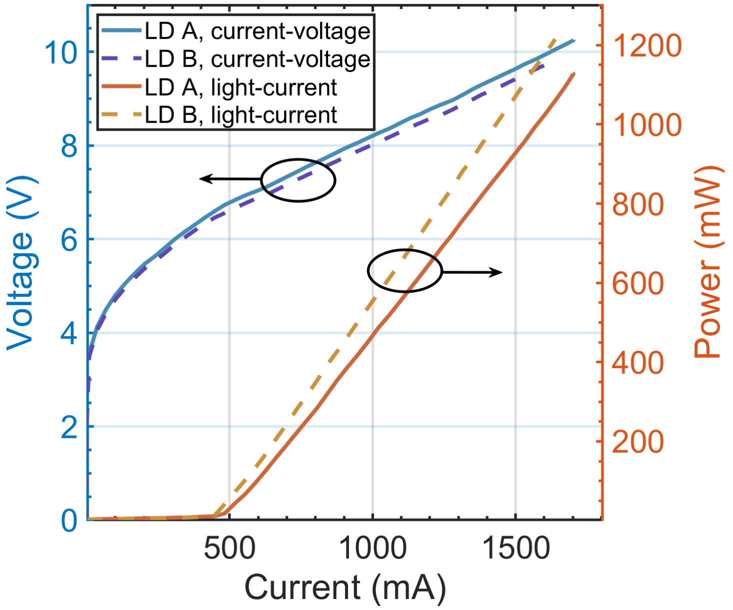

Figure 1.3: A simultaneous light-current-voltage plot, or LIV plot, of two example laser diodes (LDs) with tunnel junction contacts. Both LDs have a threshold current I_{th} of about 500 mA and a turn-on voltage of roughly 4 volts. Considering a given input current, this plot shows LD B requires a lower input operating voltage than LD A, and it emits more optical power than LD A. This makes LD B the more efficient LD.

Equation 1.2. The first efficiency component, the threshold efficiency η_{th}, quantifies the efficiency loss attributed to the threshold current I_{th}, i.e. the amount of input current that is needed just to bring the LD up to lasing threshold, i.e. emission of laser light, while not appreciably contributing to the optical power output. The second efficiency component, the differential efficiency η_d, contains (1) the injection efficiency η_i of input current that arrives as useful free charge carriers in the active region of the device (as opposed to, for example, overshooting the active region of the device or being shunted on other unintentional electrical paths), and (2) the proportion of light that escapes the laser cavity through the cavity mirrors as laser light, represented as the mirror loss α_m, relative to the total optical absorption loss, which additionally includes the *internal* optical absorption loss α_i which represents undesired absorption of light within the laser cavity before it can escape as useful light. Last, the third efficiency component, the voltage efficiency η_v, represents the proportion of applied voltage V_{in} that does useful work in generating photons. The difference between the applied voltage and the photon voltage $V_{\text{phot.}}$ is considered excess voltage and a source of inefficiency in LDs.

This analysis illuminates a few paths to improvements in PCE in LDs. First, the voltage V_{in} applied to the device may be reduced relative to the photon voltage $V_{\text{phot.}}$ by identifying and optimizing sources of series resistance (typically associated with the resistivity of materials in, and the electrical contacts to, the device) as well as components that increase the diode turn-on voltage i.e. the approximate voltage at the "bend" in a current-voltage plot like those in Figure 1.3. Typically, tunnel junctions require a finite turn-on voltage of their own for efficient conduction, and so they have been seen to increase the total LD turn-on voltage. For example, an increase of about 1.5 volts in the turn-on voltage, relative to devices without tunnel junctions, has been observed in Refs. [11] and [14]. However, tunnel junctions provide an interface between p-type GaN and n-type GaN, and so enable designs where n-type material replaces some or most p-type material, which is generally relatively more resistive to conduction [2]. In this way, while the tunnel junction contributes to turn-on voltage, it also allows the series resistance associated with p-type material to be reduced.

The threshold current I_{th} is the current at which the optical gain in the active material, related to the amount of stimulated emission, matches the total optical losses $\alpha_i + \alpha_m$ of the laser diode. The threshold current is then a function of the total internal optical absorption loss α_i, and the mirror loss α_m, which describes the amount of light that escapes the LD as useful output. We then want to minimize both the ratio α_i/α_m (to increase the differential efficiency η_d) and the sum $\alpha_i + \alpha_m$ (to increase η_d and reduce I_{th}).

The primary mechanism of concern for undesired photon absorption in III-Nitride material is free-carrier absorption, in which the energy of an absorbed photon, instead of being converted into light in a stimulated emission event, is absorbed by an electron that then transitions to an available higher energy state. Free-carrier absorption is of greater concern in materials with a high carrier density, i.e., materials that are conductive and/or have high levels of n-type or p-type doping. In particular, since typically around 2% of magnesium acceptor atoms in p-type material are ionized and can contribute to conduction [30], p-type material is often doped at relatively high levels to achieve acceptable conductivity, but as a result a large number of unionized dopant impurities are available to contribute to optical absorption. As a result, p-type material is expected to contribute relatively high amounts of loss [31]. The free carrier absorption process involving an unionized magnesium acceptor impurity atom is shown in Figure 1.4.

In semiconductor materials, the available electron energy states, or energy band structure, are approximately parabolic functions of momentum near the conduction band minimum and valence band maximum; an upward energy transition must then be matched by a specific transfer of momentum, typically an electron scattering event, for the transition to occur. Three mechanisms for momentum conservation of particular importance are:

1. phonon-assisted absorption, in which carriers scatter from vibrations in the crystal lattice;
2. alloy-assisted absorption, in which alloys of GaN e.g. $\mathrm{In}_x\mathrm{Ga}_{1-x}\mathrm{N}$ can contribute to scattering of carriers due to disordered distribution of the alloying atomic species;
3. charged-impurity-assisted absorption, in which Coulomb interactions between free carriers and impurity species can contribute to carrier scattering events.

As the density of impurities, the alloy composition, and/or or the availability of phonons (i.e. temperature) increases, free-carrier absorption events via these mechanisms become

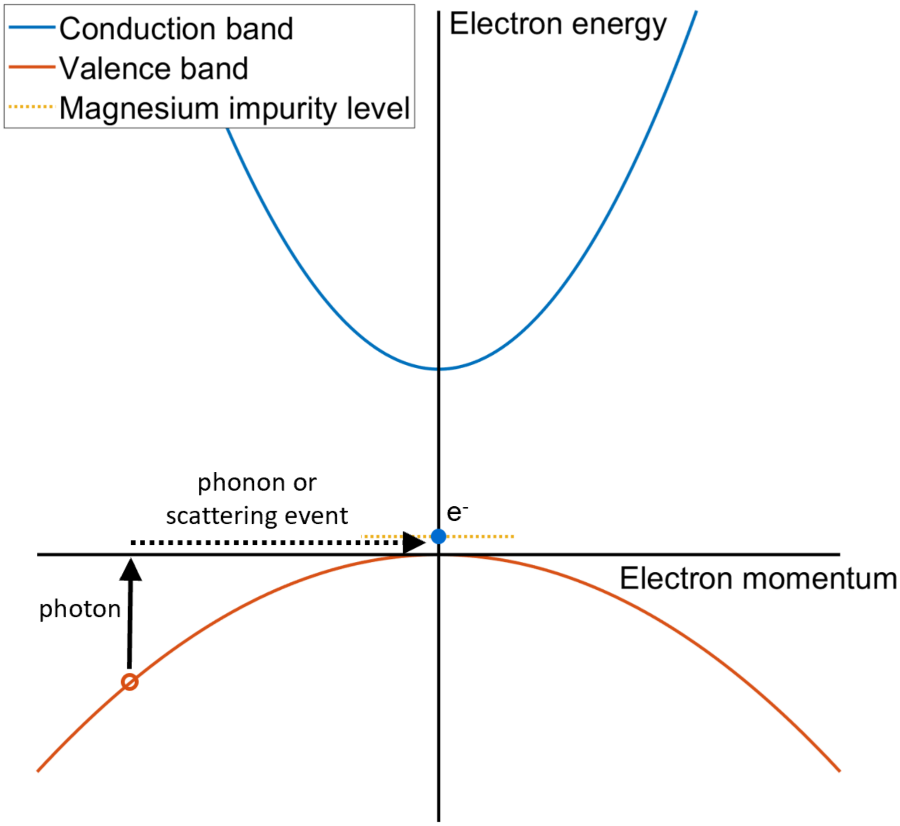

Figure 1.4: A simplified schematic diagram of the free carrier absorption event involving an unionized magnesium electron acceptor impurity: an electron in a deep valence band level receives energy from a photon and momentum from a phonon or scattering event.

more probable and so more frequent, and the internal optical absorption loss α_i increases in turn. (A more in-depth discussion of optical absorption mechanisms in III-Nitride materials is available in Refs. [31] and [32] by Kioupakis *et al.*)

Of particular concern in the context of this dissertation are the highly-doped n^{++}-GaN and p^{++}-GaN layers of a tunnel junction that contribute significantly to free-carrier absorption, since highly-doped materials generally contain higher quantities of free charge carriers, as well as to charged-impurity absorption due to their high doping levels. Metals and transparent conducting oxides (TCOs) like indium tin oxide (ITO) are also absorbing materials [33] and can contribute significantly to absorption as well. Reducing the amount of all of these materials where possible is advantageous to reducing absorption. Last, the lasing mode, i.e. the electromagnetic standing wave of photons within the laser diode, typically has its intensity maximum located by design at the active (light-emitting) region of the device in order to maximize the probability of stimulated emission events. Creating spatial separation between optically absorbing materials and the active region is then also helpful to reduce absorption.

To summarize, one of the principal goals of III-Nitride laser diode research is to maximize the total energy efficiency, or PCE, of the laser diode, and this is the principal goal of this research. This can be done by seeking optimizations that reduce the required operating voltage, or increase the light output of the device, at a given input current. The required input operating voltage can be reduced by minimizing material and interfaces that resist conduction and by optimizing the turn-on voltage of the device, and the light output can be increased by identifying and managing sources of undesired photon absorption that reduce the amount of emitted laser light. In this dissertation, we focus on the tunnel junction primarily as a means to improve LD efficiency through reduction of light absorption to processes other than stimulated emission into laser light output, i.e., the aim is to use the tunnel junction to find ways to reduce the internal optical absorption loss α_i.

1.3 The III-Nitride Tunnel Junction

1.3.1 P-Type III-Nitride Material

In the early 1990s, the formation of conductive p-type material was one of the prominent challenges in III-Nitride research. P-type material at the time was too resistive for practical devices. This changed in 1989 when Amano *et al.* demonstrated electrically active p-type material using a low-energy electron-beam irradiation (LEEBI) treatment [34], and subsequently in 1991-1992 when Nakamura *et al.* demonstrated active p-type GaN material achieved through thermal annealing above 700°C in nitrogen environments [35]. Shortly afterwards, Nakamura *et al.* also demonstrated the compensation of Mg electron acceptor dopants by hydrogen [36]. In other words, the thermal anneal allows hydrogen present in p-type material, which is typically located at the top of the epitaxial structure, to diffuse vertically upwards out of the free surface on the top of the wafer. This has led to the common practice of achieving conductive p-type material through this anneal, also referred to as a thermal activation, typically but not always at an intermediate stage in between crystal growth and nanofabrication.

As was previously discussed, today's p-type III-Nitride material still generally has poor conductive properties relative to n-type material [2], where in p-type material about 2% of dopant impurities used to facilitate electrical conduction in p-type material ultimately contribute to conduction [30]. To compensate for this, p-type material is typically doped at relatively high levels in order to achieve adequate conduction. As a result, p-type III-Nitride material is generally considered a relatively absorbing material [3] while still being relatively resistive.

One problem presented by the conductivity issues of p-type material in practical III-Nitride devices is that it not a good lateral current spreader: injecting current directly into p-type material, which in non-tunnel junction optoelectronic devices is most commonly located at the top of the device epitaxial structure, can lead to highly nonuniform lateral distribution of current flow across the device area [37]. Furthermore, in the areas through which current does flow, the resulting relatively higher current densities may lead to premature efficiency droop [18]. Because of this, III-Nitride LED devices, which often do not electrically contact the full device area for better vertical extraction of emitted light, often utilize transparent conducting oxides (TCOs) such as indium tin oxide (ITO) to spread current across the entire device area, improving device efficiency [38].

In LDs, light is emitted laterally and so vertical current injection directly into the full device area is common, unlike in LEDs. However, another issue arises: the metal contact contributes a significant amount of internal optical absorption loss to the device. Increasing the thickness of the p-type material in order to spatially separate the metal from the lasing mode would reduce the metal's contribution to optical absorption losses, but the generally poor conductive properties of p-type material mean this strategy results in an efficiency penalty in the form of increased operating voltage. Here, too, TCOs are often used: they provide a spatial separation between the metal and the lasing mode, and they are more conductive than p-type material. Also, while TCOs are a relatively optically absorbing material [33], their refractive index contrast with GaN helps to confine the optical standing wave of the lasing mode away from both the TCO and the metal, reducing their respective contributions to optical absorption losses.

1.3.2 Pros and Cons of the Tunnel Junction

The tunnel junction presents another approach to the improving conductivity and absorption properties on the p-side of III-Nitride devices:

1. form n-type material between the metal contact and the p-type material: the preferable conduction and absorption properties of n-type material allow for a greater thickness of material without a penalty to absorption or conductivity. This creates a physical separation of the highly-optically-absorbing metal layer from the active region (this also removes the need for the also highly-optically-absorbing ITO layer, which as previously described would otherwise serve a similar purpose);

2. join the n-type and p-type material with a highly-doped pn junction that achieves conduction not through forward bias diode conduction but through electron tun-

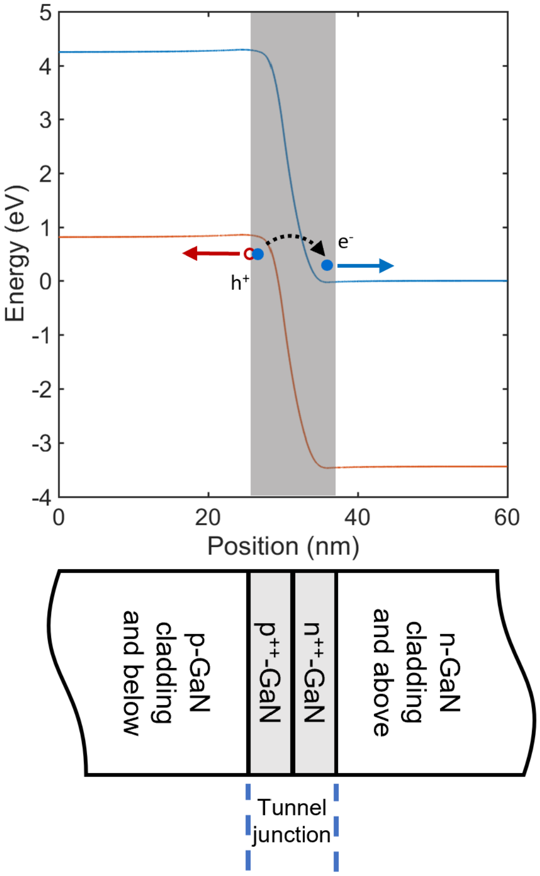

Figure 1.5: Energy state diagram of the tunnel junction. In this diagram, an electron e^- tunnels from the lower valence band of energy states, in red, from the p-type material rightwards to the higher-energy conduction band of energy states, in blue, in the n-type material; this process leaves behind an electron energy state vacancy, or hole h^+. Note that this energy state diagram depicts the tunnel junction under common operating conditions (1.5 V of reverse bias across the tunnel junction in order to improve tunneling [11, 14]).

neling from the valence band in the p-type material to the conduction band in the n-type material.

An energy band diagram illustration of the tunnel junction is pictured in Figure 1.5, and schematic illustrations of example epitaxial structures with and without a tunnel junction are provided in Figure 1.6.

The tunnel junction strategy comes with several advantages, including:

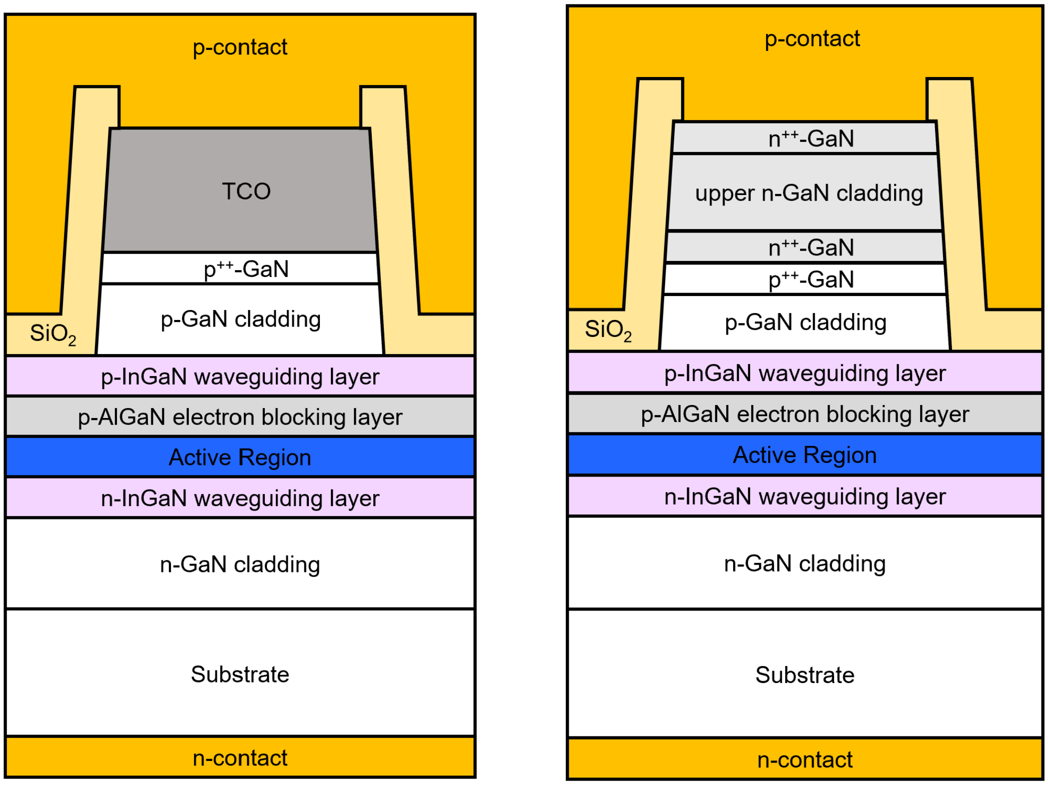

(a) (b)

Figure 1.6: Cross-sectional schematics of generic epitaxial layer stacks for III-Nitride optoelectronic devices without a tunnel junction and (b) with a tunnel junction.

- circumventing the extra absorption associated with adding a TCO layer,
- efficiently spreading current across the device area for devices with nonuniform electrical contacting such as LEDs and micro-LEDs and off-ridge contacted edge-emitting LDs [16],
- simplifying fabrication processes, reducing the time and cost of fabrication:
    - metal contacts, which are otherwise typically formed separately on n-type and p-type material, may be formed simultaneously to n-type material located above and below the active region (i.e. on devices with both contacts located on the same side of the wafer),

  - TCO deposition may be skipped entirely;
  - in some cases, tunnel junction device crystal growth may take place monolithically in one crystal growth step without removal from the reactor; this has been demonstrated on e.g. molecular beam epitaxy-grown tunnel junction devices [13] and has been researched in part on devices grown by metalorganic chemical vapor deposition [39]

- allowing replacement of the contact to p-type GaN with another contact to n-type GaN, where contacts to n-type GaN are often much less resistive than contacts to p-type GaN, benefitting device efficiency [40, 41],
- allowing an additional cladding layer of n-type GaN, as shown in Figure 1.6b, to be added above the tunnel junction; this layer may be used to spatially separate the metal contact from the active region in order to reduce the contribution of the metal to optical absorption losses.
- allowing reduction of p-type cladding material, which was previously shown to have undesirably resistive and absorptive properties.

However, significant challenges remain for tunnel junction devices:

- For efficient tunneling, the tunnel junction requires its own voltage bias in addition to that of the rest of the LD. This increases the input voltage needed for a given output power, reducing device efficiency. In most cases, this effect dominates over the reductions in voltage associated with the advantages that were discussed above.
- While p-type material is usually located at the top of the crystal growth structure such that compensating hydrogen may diffuse vertically out of the wafer during the activation anneal, a tunnel junction regrowth in metalorganic chemical vapor

deposition crystal growth conditions which are frequently hydrogen-rich exposes the p-type material to hydrogen, effectively repassivating it, and then subsequently adds n-type material on top through which the hydrogen cannot diffuse [42]. Tunnel junction device fabrication processes must address this repassivation either by using crystal growth processes that are sufficiently free of hydrogen such as molecular beam epitaxy [43, 44] or by removing the hydrogen through a lateral diffusion scheme after crystal growth is completed [5, 45, 46, 47, 48].

- For efficient tunneling, the tunnel junction also requires highly doped material in its immediate vicinity. This helps to minimize the width of the energy barrier to electron tunneling and so reduce the voltage increase associated with the tunnel junction. (For more, Ref. [49] provides a good discussion of PN junction basics.) However, highly doped material is generally also highly absorbing and has the potential to significantly increase optical absorption losses and diminish LD performance. This creates a balance problem between managing the absorption of the tunnel junction layers and the voltage increase associated with the tunnel junction turn-on voltage. Reducing the thickness of the highly doped layers to the minimum may help, and this essentially specifies the balance problem to one between managing the absorption of the tunnel junction and ensuring that there is sufficient highly doped material to support tunneling.

- The aforementioned high doping may be compensated and so in effect reduced if, for example, Mg dopants used to form the p-type GaN diffuse into the n-type GaN, where they can compensate for the n-type Si dopants. Controlling the rise and fall of the [Mg] and [Si] doping profiles of the tunnel junction is therefore also important to efficient operation. Various mechanisms for Mg diffusion have in particular been the subject of various studies in the literature [50, 51, 52, 53, 54].

Many of these challenges are at time of writing the subjects of ongoing research.

1.4 Crystal Growth of III-N Optoelectronic Devices

Having motivated the III-Nitride LD as a device and the tunnel junction as a design element for this device, and having established a foundation for how semiconductor LDs and their constituent parts function, we turn our attention in the rest of this chapter to how these devices and structures are formed.

1.4.1 Metal-Organic Chemical Vapor Deposition

Devices in this thesis were primarily grown using metal-organic chemical vapor deposition (MOCVD), a non-equilibrium crystal growth technique in which vapor-phase chemical precursors are transported to a reactor chamber held at high temperature (typical growth temperatures in this work ranged from 850°C to 1180°C). This growth is typically facilitated by carrier gases such as nitrogen and hydrogen gas that flow at high rates in order to improve transport of precursor species. In the high-temperature reactor chamber, these precursors decompose into their respective atomic species, which deposit on a substrate wafer in the chamber, and their byproducts, which are mostly removed from the growth chamber.

In this work, the metalorganic chemicals trimethyl gallium (TMG) and triethyl gallium (TEG), trimethyl aluminum (TMA), and trimethyl indium (TMI) were respectively used as gallium, aluminum, and indium precursors. Additionally, disilane (Si_2H_6) and Bis(cyclopentadienyl)magnesium (abbreviated Cp_2Mg) were used as precursors to the dopant impurities Si and Mg. Ammonia was used as the nitrogen precursor, and nitrogen and hydrogen gas were both used as carrier gases.

While the vast majority of commercial III-Nitride devices are formed on Al_2O_3 (sapphire) substrates for cost effectiveness, the devices fabricated in this dissertation were fabricated on freestanding semipolar GaN substrates that are, as is discussed below, on the $(20\bar{2}\bar{1})$ crystal plane orientation. Freestanding GaN provides the benefit of a significantly reduced density of threading dislocation crystal defects, which is critical to LD operation [55]. In this work, freestanding semipolar GaN substrates were used for all devices; these substrates were provided by Mitsubishi Chemical Company.

In tunnel junction research, where it is critical to grow thin, highly-doped layers with minimal diffusion into adjacent layers, a few concerns are present. First, while TMG is an effective gallium precursor for the thicker template and n-type GaN layers near the bottom of the epitaxial structure that are grown first, it can create issues in the active region, where it can contribute carbon impurities and reduce overall power [56], as well as in the tunnel junction, where more precise thickness control is needed for the highly doped n++ and p++ GaN layers. MOCVD-grown tunnel junctions were generally grown using TEG as the gallium precursor at relatively slow growth rates for improved thickness control, though TMG was generally used for the n-type cladding grown following tunnel junction growth. Second, magnesium is known to exhibit a “memory” effect in which it may linger in an MOCVD reactor well after any p-type material has been grown [54], and has been shown to diffuse into subsequently grown layers if not managed [50, 51]. In this work tunnel junctions were regrown following initial growth up to p-type material, removal from the reactor, and a hydrofluoric acid surface treatment. Tunnel junctions were grown after the reactor chamber had been baked out immediately prior in order to remove residual magnesium from previous growth cycles.

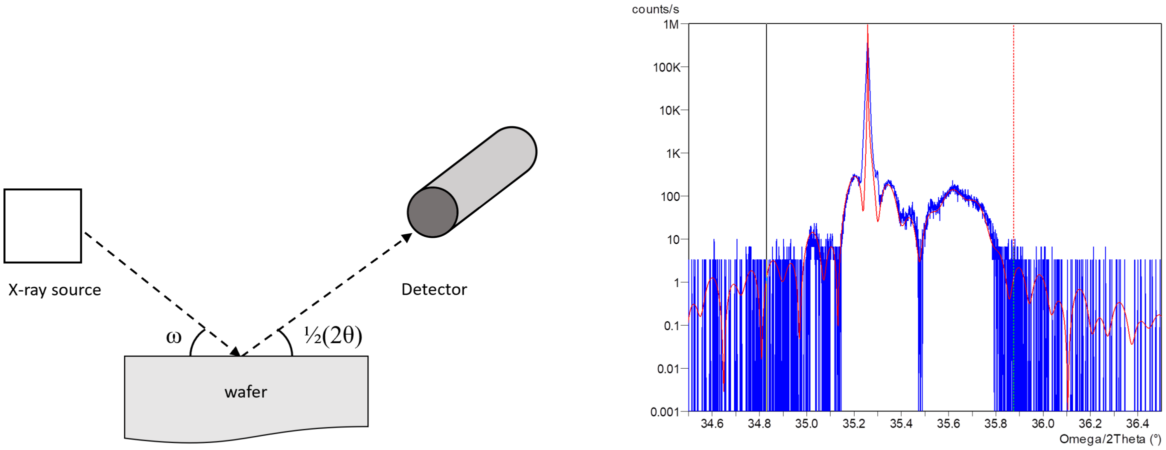

(a) (b)

Figure 1.7: (a) A simplified schematic representation of an x-ray diffraction experiment. (b) An example of the data from an x-ray diffraction experiment (blue), where parameters are extracted through fitting a modeled curve (red) [58].

1.4.2 Growth Calibrations

Growth rates and alloy compositions were calibrated using x-ray diffraction, which may be briefly summarized as a nondestructive characterization technique in which the interference patterns of x-ray radiation reflected from the surface of a wafer may be used to extract data about the structure and composition of that wafer. In this work, x-ray diffraction was used to obtain thicknesses of constituent layers on a wafer as well as their alloy compositions. This was typically done by running $\omega - 2\theta$ scans on simple structures in order to calibrate growth rates (i.e., from measured thickness and nominal growth time) and alloy compositions versus certain crystal growth parameters. To illustrate, schematic representation of an x-ray diffraction measurement is provided in Figure 1.7a, and Figure 1.7b provides an example of the result of an x-ray diffraction measurement. An in-depth discussion of x-ray diffraction physics can be found in Ref. [57]. X-ray diffraction measurements used in the course of the research described in this dissertation were carried out at the X-ray Facility at the Materials Research Laboratory at UCSB.

Doping levels were calibrated and characterized using secondary ion mass spectroscopy (SIMS) at the UCSB California Nanosystems Institute (CNSI). This compositional characterization technique bombards a small area of a wafer with ions in order to eject atoms from the surface; the SIMS system then subsequently analyzes the mass and charge of the ejected atoms in order to find the layer-by-layer concentrations of atomic species of interest. In III-Nitride research, SIMS may be used to find depth profiles of the concentrations of alloy atoms such as indium and aluminum, dopants such as magnesium and silicon, impurities such as hydrogen, oxygen, or carbon, and/or other atomic species of interest.

In this work, SIMS was primarily used to calibrate doping levels and characterize tunnel junction doping profiles. Due to the small dimensions of the highly-doped tunnel junction layers, which can nominally be under 10 nm thick, it was important to work as close to the depth resolution limit of the SIMS system as reasonably possible in order to obtain the most accurate data possible. For an example of the result of a SIMS characterization, see Figure 2.7.

1.4.3 Semipolar Crystal Planes of GaN

Materials belonging to the III-Nitride materials system, such as GaN, are crystalline materials with a repeating wurtzite structure. While most III-Nitride devices are produced using (0001) or c-plane oriented material due to availability and cost, the III-Nitrides are also a polar materials system, and polarization-related electric fields occur at the interfaces into device regions where GaN is alloyed with other III-Nitride materials, such as InN and AlN, for the desirable properties of those materials. These polarization-related electric fields occur along the axis of the c-plane and may augment or diminish performance of devices produced on this crystal orientation.

However, crystal orientations that are inclined relative to this plane have been shown to yield improved optical properties for devices, for example increased overlap of electron and hole (i.e. electron energy state vacancy) wavefunctions in the device active region [59]. This assists in light emission, i.e. improves the probability of desired radiative energy transition events. These crystal planes also show reduced wavelength shift with increasing input current density [59], which is a desirable property for commercial devices in which reliability is a concern. Last, these planes show increased material gain [60, 61]. This would help reduce the threshold current density required to bring the LD across threshold into the desired lasing operating regime. For these reasons, all devices discussed in this dissertation are fabricated and/or modeled on the $(20\bar{2}\bar{1})$ crystal plane on freestanding GaN substrates.

1.5 Nanofabrication and Characterization of III-Nitride Optoelectronic Devices

1.5.1 Nanofabrication Process

Following successful crystal growth, the researcher obtains a flat wafer with the full epitaxial stack but no topographical features, and nanofabrication techniques must be used in order to form a physical structure optimized for LD operation. This work ultimately involves (1) constructing the laser optical cavity and mirrors in order to facilitate stimulated emission events, and (2) depositing metal contact pads on the wafer such that devices may be electrically probed and operated. The devices described this dissertation were all fabricated in the UCSB Nanofabrication Facility.

Figure 1.8 shows a schematic three-dimensional illustration of this LD structure, as well as a two-dimensional schematic cross-section of an LD showing the layer-by-layer

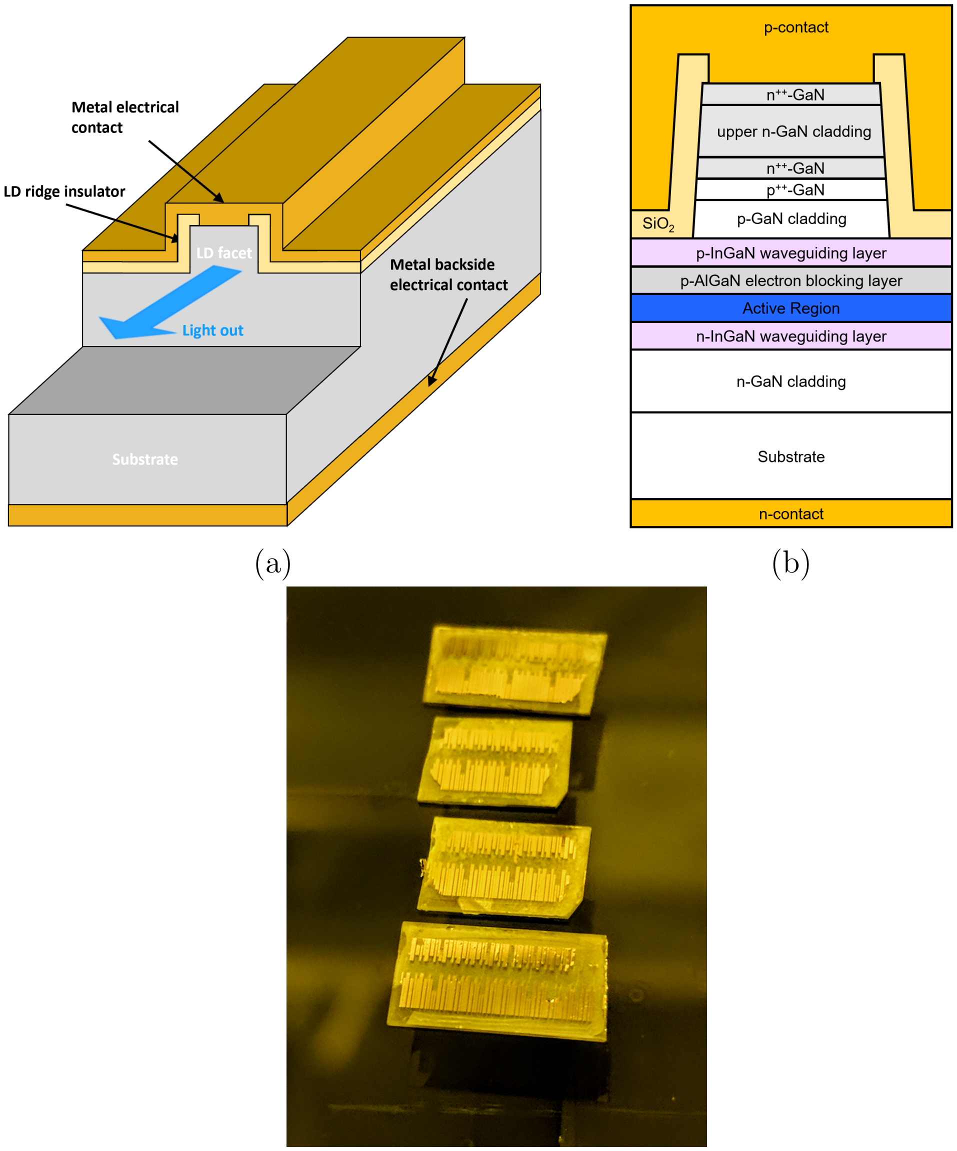

(a) (b)

(c)

Figure 1.8: (a) A three-dimensional not-to-scale model of an edge-emitting LD at the end of its fabrication process. (b) A two-dimensional cross-section of an LD in the plane of the LD facet. (c) An image of four freestanding GaN wafers at the end of the fabrication process, where each vertical metal bar indicates the location of one laser diode.

epitaxial structure, and a top-down photograph of freestanding GaN wafers that have undergone the full LD crystal growth and nanofabrication process. While LD fabrication processes and final products vary greatly by implementation, these are representative of the LDs built and modeled in this dissertation.

Most nanofabrication steps are generally able to be sorted into one of the below categories:

- Lithography: A simple lithography step generally involves (1) coating the wafer in photoresist i.e. a light-sensitive polymer; (2) aligning existing features on the wafer to a mask that selectively covers and exposes areas of the wafer in a pre-defined pattern; (3) exposing the areas of the wafer not covered by the mask to (e.g.) ultraviolet light, such that (4) the photoresist in this areas weakens and may be removed in developer that selectively dissolves the photoresist that was (or was not) been exposed. While photolithography i.e. light-based lithography is perhaps the most widespread form of lithography, other techniques exist. For example, processes requiring high precision and/or small features often use electron beam lithography, which while more costly and time intensive is generally able to deliver smaller features than what is possible with photolithography.

- Deposition: This involves deposition of a thin film of material onto the wafer surface, typically through evaporation from or scattering off a source material. Common deposition techniques involve thermal evaporation, electron beam evaporation, sputtering, ion beam deposition, and chemical vapor deposition. Over the course of this dissertation, SiO_2, indium tin oxide (ITO), and several metals were all deposited through various deposition processes. An inclusive definition of deposition would also include crystal growth techniques such as MOCVD and MBE, which of course were used in this work to deposit GaN and its alloys.

- Etch: Material may be removed from a wafer through wet etching, typically by submerging the whole wafer in acid solution, or through dry etching, i.e. exposing the wafer to a controlled plasma environment. Wet etches may be also used to treat an exposed surface for oxidation prior to steps where surface quality is important such as metal contact deposition and tunnel junction regrowth [41, 50, 51].

An in-depth discussion of nanofabrication techniques and technologies is available in Ref. [62].

A simplified explanation of the features of the full LD structure pictured in Figure 1.8a, their functions, and how they are formed, follows:

- Areas to be processed for each of the below steps are first differentiated through a lithography step.

- The rectangular bar that makes up the LD ridge defines the optical cavity. Through its refractive index contrast with its outside environment, it assists with confinement of light to an area corresponding to the lasing mode standing wave. In this work the LD ridge is formed by etching away material outside of the LD ridge in a dry etch step.

- The SiO_2 insulating layer has the primary purpose of confining current injection to the top of the LD ridge. The SiO_2 layer is formed through a deposition step.

- As previously explained, the metal contacts electrically connect to the top and bottom of the epitaxial structure and allow for efficient current injection into the device. Typically contacts to p-GaN and n-GaN are formed in two separate process steps; in tunnel junction devices where both contacts are to n-GaN and are also on the same side of the wafer, both contacts may be formed simultaneously. In this work the metal contacts are formed in two separate deposition steps, one each to the top and bottom of the wafer.

- Facets are formed through two additional dry etch steps (one for each side of the LD bar). These dry etch steps provide improved verticality over the etch that was

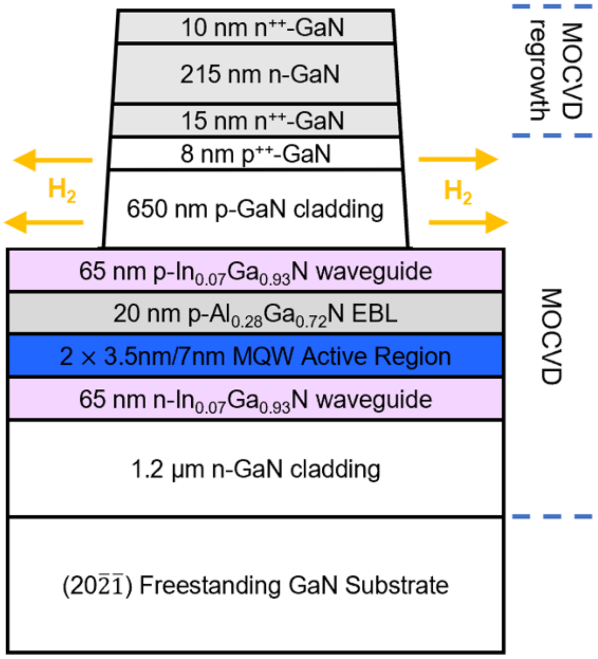

Figure 1.9: Cross-sectional schematic of the LD ridge sidewall activation scheme: After defining the LD ridge, all photoresist is removed and the LD is annealed at high temperature, allowing hydrogen to diffuse laterally out of the p-type material.

used to define the LD ridge; this helps to reduce the input electrical power required in order to achieve laser threshold i.e. threshold current [26, 63, 64].

A more thorough set of steps for the LD fabrication process used in this work is provided in Appendix A.

1.5.2 Sidewall Activation

Activation of p-type material is straightforward in III-Nitride devices with no tunnel junction above that material: an anneal immediately post-MOCVD growth and pre-nanofabrication causes hydrogen to diffuse vertically out of the wafer. Devices with an MOCVD-grown tunnel junction, however, re-expose the p-type material to a high temperature environment where hydrogen is present, and subsequently cap their p-type material with n-type material through which hydrogen cannot diffuse [42]. In order to produce III-Nitride devices that both have a tunnel junction and are viable, advanced strategies for activation are needed. These strategies generally employ lateral diffusion of hydrogen around the n-type tunnel junction material towards a free p-GaN surface where it can exit the wafer. This creates a constraint on fabrication processes: at some point during fabrication, a sufficient amount of free p-GaN surface must be exposed per device such that an anneal step may be inserted in the process for full electrical activation of the p-type material.

The strategy used in this dissertation, pictured in Figure 1.9, inserts an anneal step in between formation of the LD ridges and the deposition of the SiO_2 insulator layer, where the LD ridges are of a width such that hydrogen is feasibly able to diffuse out of the full device area. This strategy was first demonstrated in LEDs with MOCVD-grown tunnel junctions [5]. Other similar strategies have successfully realized III-Nitride devices with MOCVD-grown tunnel junctions. For example, etched vias through n-type material to the p-type material can provide windows such that hydrogen may diffuse laterally towards, and then out of, those windows; however, dry etch damage to material exposed during the etch may compensate p-type material and risks creating issues for hydrogen outdiffusion [65, 66]. Selective area growth (SAG) techniques, in which a hardmask pattern formed by (e.g.) SiO_2 on the wafer allows for III-Nitride material to be grown in select areas, have resulted in via formation that produced successful microLEDs [46, 47].

1.5.3 Characterization Techniques

During fabrication, multiple diagnostic techniques are available to the researcher that allow verification of the success of, or failure analysis for, each process step. In this work, the accuracy of lithography alignments relative to existing features on the wafer were assessed by optical microscope; dry etch rates were calibrated by laser microscopy or depth profilometry; LD facet etch rate and verticality were calibrated using a scanning electron microscope (SEM); thin film deposition rates were calibrated by ellipsometry. Last, secondary ion mass spectroscopy (SIMS), also mentioned in subsection 1.4.2, was used to measure doping levels as a function of depth in the wafer as was relevant during and after fabrication.

Following fabrication, the wafer is placed on a position-adjustable stage where LDs may be individually electrically probed. Emitted laser light is aligned with a lens such that it is collimated and directed into an optical integrating sphere that may read the total LD output optical power in tandem with other instrumentation for reading the operating voltage and supplying various levels of input electrical current. This process is repeated for each facet of each LD in order to calculate total output power and overall power conversion efficiency for each LD. A spectrometer is also used to read the lasing spectrum of the LD. Once the LD is electrically connected, data collection is mostly automated; Figure 1.3 shows an example of the end result of this process.

1.6 A Short Review of III-Nitride Tunnel Junction Research Progress

Semiconductor tunnel junction research finds its origins in research by Esaki *et al.* in which the tunnel junction was first demonstrated in Germanium in 1957 [4, 67]. The first study demonstrating tunnel junctions in the III-Nitride materials system was published by Jeon *et al.* in 2001 [68], and other studies followed later that year [69, 70]. Since then, research has expanded to address various facets of tunnel junction devices. Particularly active sites of research are (1) reducing the operating voltage of tunnel junction devices relative to non-tunnel junction devices and (2) activating p-type material or maintaining its activation in tunnel junction devices. In this section, we briefly review the research into tunnel junctions in the III-Nitrides materials system in terms of these two research fronts.

1.6.1 Managing the Tunnel Junction Voltage

As was previously discussed, reducing the voltage penalty of the tunnel junction, i.e. reducing the electron tunneling distance of the tunnel junction, is important to improving device efficiency for tunnel junction device efficiency. One strategy to do so involves using alloys of GaN to achieve polarization-enhanced tunneling. This was demonstrated in 2007 and 2009 using AlN based tunnel junctions [71, 72] and in the early 2010s using GaN-InGaN-GaN based tunnel junctions [73, 74, 75, 76, 77], where InGaN provided the additional benefit of a reduced bandgap, helping to reduce the energy barrier to tunneling. Multiple later experiments similarly showed voltage improvements through incorporation of increasing amounts of InGaN into the tunnel junction [47, 78, 79, 80], as well as through grading of the InN content of the tunnel junction [81]. In particular, tunnel junction voltage reduction through use of InGaN (i.e., reducing the tunnel junction band gap E_G by incorporating indium into the tunnel junction to achieve a lower-bandgap InGaN layer and reduced tunneling distances) is especially helpful on semipolar and nonpolar crystal planes where polarization-based strategies are unavailable.

The treatment of and composition at the interface between p++ and n++ material, which is frequently the regrowth interface for non-monolithically-grown devices, is also critical to tunnel junction research. Magnesium has been shown to have various mechanisms for diffusing into subsequently grown layers [52, 53, 54]. In tunnel junction devices, this would have the effect of compensating the n-type side of the tunnel junction, in effect increasing the depletion width and in turn the tunneling width and excess voltage of the tunnel junction. Control of this diffusion is important to achieving narrow depletion widths. In 2016, a study examined hydrofluoric acid (HF), aqua regia, and hydrochloric acid treatments, all showing reductions in voltage; the HF was additionally shown to somewhat reduce magnesium in subsequently grown layers [6]. In 2017, two additional studies showed HF surface treatments prior to MOCVD regrowth can significantly reduce diffusion of Mg into subsequent layers [50, 51]; a study published in 2021 showed the same [82]. Also, in 2014, a study attributed an increase in operating voltage (of a two-step-growth device over a monolithically grown device) to impurity incorporation at the regrowth interface [76], and in 2015, SIMS measurements of an MBE-grown tunnel junction LED showed a thin, high-concentration layer of oxygen at the interface, which was modeled to provide an n-type delta doping effect and reduce the electron tunneling distance [83].

1.6.2 Hybrid MBE-MOCVD Growth

Since MOCVD growth conditions are known to passivate p-type material with hydrogen, rendering it nonconductive [36], one often-used strategy for realizing viable tunnel junction devices is growth of the tunnel junction through molecular beam epitaxy (MBE), where MBE contains a sufficiently low pressure of hydrogen that passivation of p-type material is not a concern [43, 44]. While MOCVD is generally more suitable to use in commercial applications, use of MBE in this way allows for rapid demonstration of III-Nitride devices with tunnel junctions and also allows for experiments on other aspects of the tunnel junction that are not confounded by issues with activation of p-type material. At UC Santa Barbara, hybrid MOCVD-MBE III-Nitride tunnel junction device growth, first demonstrated by Young *et al.* in 2015 [83], has been used to demonstrate LEDs [6, 78, 82, 84], ultraviolet LEDs [85], vertical cavity surface-emitting lasers (VCSELs) [11, 86], and edge-emitting laser diodes [12, 14], and cascaded-active-region devices [87]. Similar reasoning can be used to motivate research on fully MBE-grown III-Nitride devices, and this strategy has been used to show evidence of trap-assisted Auger recombination in III-Nitride LEDs in 2019 [88], realize polarization enhanced tunnel junctions [73, 74, 75], and demonstrate ultraviolet LEDs [89, 90], cascaded LDs [15], and distributed feedback LDs [9].

1.6.3 Lateral Activation of the Tunnel Junction

The alternative strategy to MBE regrowth of the tunnel junction is to use MOCVD and subsequently remove hydrogen through lateral diffusion during an activation anneal. This was demonstrated for LEDs in 2013 [5] where a region up to 80 μm deep from the sidewall luminesced following a 30-minute anneal, suggesting devices of similar feature sizes may be feasibly fully activated with this method. This strategy was subsequently used to implement MOCVD-grown tunnel junctions on micro-LEDs in 2018 [7] and on edge-emitting LDs in 2019 [14]. Monolithically-grown tunnel junction LEDs activated in this way were also demonstrated in 2017 [37].

However, dry etch steps used to form LD ridges and LED mesas have been shown to damage exposed material, in particular compensating p-type material [65, 66]. In 2021 it was shown that surface treatments of the exposed sidewalls prior to activation, as well as multiple cycles of this process help achieve full removal of hydrogen from the entire device area in micro-LEDs [48].

While sidewall activation has yielded viable devices, its applications are limited to smaller device sizes such that hydrogen may efficiently diffuse out of the full device area.

In 2020, micro-LEDs with selective-area-growth (SAG) tunnel junctions were demonstrated [46, 47]. The SAG scheme provided vias in the tunnel junction regrowth such that hydrogen was able to diffuse laterally a short distance to a free p-GaN surface regardless of device size or geometry. This method also had the benefit of protecting most of the free p-type surface from dry etch damage.

Last, *in situ* activation of p-type material immediately prior to tunnel junction regrowth, as part of a fully-MOCVD growth process for vertical cavity surface emitting lasers (VCSELs), was shown to improve performance [39]. While not strictly an activation technique utilizing lateral diffusion of hydrogen, such a process if made sufficiently efficient would address the same issues of p-GaN activation that lateral diffusion strategies also seek to manage.

Chapter 2

Tunnel Junction Contacts for High-Power Semipolar III-Nitride Edge-Emitting Laser Diodes

This chapter is based on the following publication in *Optics Express*: “Efficient tunnel junction contacts for high-power semipolar III-nitride edge-emitting laser diodes,” by Shereen W. Hamdy, Erin C. Young, Abdullah I. Alhassan, Daniel L. Becerra, Steven P. DenBaars, James S. Speck, and Shuji Nakamura, Opt. Express **27**, 8327-8334 (2019)

2.1 Motivation

LEDs from the III-Nitride materials system currently provide energy-efficient commercially available solutions for various lighting applications. However, they show efficiency droop at elevated current densities [18]. This increases the chip area required for many applications, in turn raising associated substrate and crystal growth costs. Since their first demonstration in the 1990s [19], III-Nitride laser diodes (LDs) have offered an alternative to III-Nitride LEDs. As current density increases beyond LD lasing threshold, the light output power increases continuously with increasing current up to thermal rollover, where the peak gain is saturated and gradually reduced due to heat generation. This allows LDs to achieve power densities much higher than are achievable in LEDs, with one edge-emitting LD able to match the light output of multiple LEDs. This yields cost savings associated with reduced chip area and makes LDs a promising candidate for white lighting [21]. Use of LDs also creates new opportunities in several future applications using highly directed light such as laser projector displays, fiber-guided lighting, and visible light communication [22]. However, adoption of III-Nitride LDs into commercial products, particularly white lighting, is still limited: III-Nitride LDs currently exhibit wall plug efficiencies too low to match those of III-Nitride LEDs [28, 91]. To be competitive as a white lighting technology, LD performance must be improved through advancements in differential efficiency, threshold current density, and operating voltage.

Use of semipolar growth planes is one method to increase III-Nitride LD wall plug efficiencies. While commercial LDs are most frequently grown on the (0001) crystal plane, semipolar planes (hkil), where l and h or k are nonzero, are inclined with respect to the (0001) plane and have reduced discontinuities in total polarization at heterointerfaces. In the case of InGaN quantum wells, most semipolar crystal orientations, such as $(20\bar{2}\bar{1})$, have significantly reduced polarization-related electric fields in comparison with the (0001) plane. The reduced electric fields in the quantum wells increases the electron-hole wavefunction overlap and reduces wavelength shift with current density [59, 60, 61]. Semipolar and nonpolar crystal planes also yield increased material gain due to strain-induced splitting of the topmost two valence bands in the InGaN quantum wells and reduced hole effective mass caused by the anisotropic band structure of these planes and augmented by biaxial strain [60, 61].

There is also space for reducing the internal optical loss of III-Nitride LDs, which contributes both to low differential efficiencies and high threshold current densities. P-type GaN [31] and a transparent conducting oxide (TCO) layer, typically indium tin oxide (ITO) [92], are significant contributors to internal optical loss in LDs. Tunnel junctions offer an alternative design that reduces or eliminates the absorption of both of these layers. Instead of a TCO layer, n^{++}-GaN is grown on top of a p^{++}-GaN contact layer terminating the p-type GaN cladding layer. The resulting p-n junction has a depletion region narrow enough for electrons to tunnel through from the valence band of the p-type layer to the conduction band of the n-type layer when operating in reverse bias [83]. After the n^{++}-GaN, lightly doped n-GaN is also grown as an additional cladding layer. The resulting design replaces the TCO layer with the tunnel junction and the less absorbing lightly doped n-GaN layer. If the highly doped layers in the tunnel junction can be mostly depleted of free carriers, their optical absorption can be minimized as well.

One issue any tunnel junction implementation must resolve is the activation method for its p-type GaN. P-GaN requires post-growth annealing to electrically activate Mg dopants, which are passivated by hydrogen introduced as a carrier gas and by decomposing ammonia during MOCVD growth [36, 35]. Performing an MOCVD regrowth over activated p-GaN re-passivates the p-GaN with hydrogen, and the n-GaN regrowth presents a potential barrier as well as a diffusion barrier that prevents reintroduced hydrogen from diffusing through it during a subsequent activation step [42]. This problem may be resolved by growing the tunnel junctions using MBE, which uses an ultra-high vacuum environment with a sufficiently low pressure of ammonia to maintain active p-GaN [83]. The problem of re-passivated p-GaN by MOCVD growth conditions may also be resolved by etching features through the p-GaN and then annealing the wafer to allow hydrogen to laterally diffuse through the feature sidewalls instead of through the wafer surface. This method would be particularly attractive from a technological perspective, where MOCVD is already the industry standard crystal growth technique with significant advantages in scalability. However, this method is less effective for larger devices where hydrogen must diffuse a greater distance to realize a fully activated device [5, 7, 37].

2.2 Progress in MBE-Grown Tunnel Junction Contacts for III-Nitride Edge-Emitting Laser Diodes

2.2.1 Crystal Growth and Fabrication

In this work, we demonstrated edge-emitting LDs with MBE-grown tunnel junction p-contacts and identical LDs using ITO p-contacts instead as a baseline reference. Light-current-voltage data were measured under pulsed conditions from all devices, and the performance of these devices was analyzed and compared.

Cross-sectional schematics summarizing the common laser diode epitaxial growth, the tunnel junction regrowth, and the fabricated laser diode structures are shown in Figure 2.1. An epitaxial structure optimized for blue edge-emitting laser diodes was grown by atmospheric pressure MOCVD on freestanding $(20\bar{2}\bar{1})$ bulk GaN substrates provided by Mitsubishi Chemical Corporation. This structure consisted of, in order of growth, 1.2 μm of n-GaN, a 65 nm n-$In_{0.07}Ga_{0.93}N$ waveguiding layer with a 10 nm compositional grade to GaN on either side, a two-quantum-well active region consisting of 3.5 nm $In_{0.18}Ga_{0.82}N$ wells and 7 nm GaN barriers, a 10 nm p-$Al_{0.28}Ga_{0.72}N$ electron blocking layer (EBL) and then a 10 nm grade to p-GaN, a 65 nm p-$In_{0.07}Ga_{0.93}N$ waveguiding layer with a 10 nm compositional grade to GaN on either side, 650 nm of p-GaN cladding, and an 15 nm p^{++}-GaN contact layer. Wafers that would see a tunnel junction regrowth were grown with a thinner p^{++}-GaN contact layer thickness, calculated to minimize nondepleted p^{++}-GaN. This thickness was determined to be 8 nm after accounting for uncertainties in the growth rate calibration.

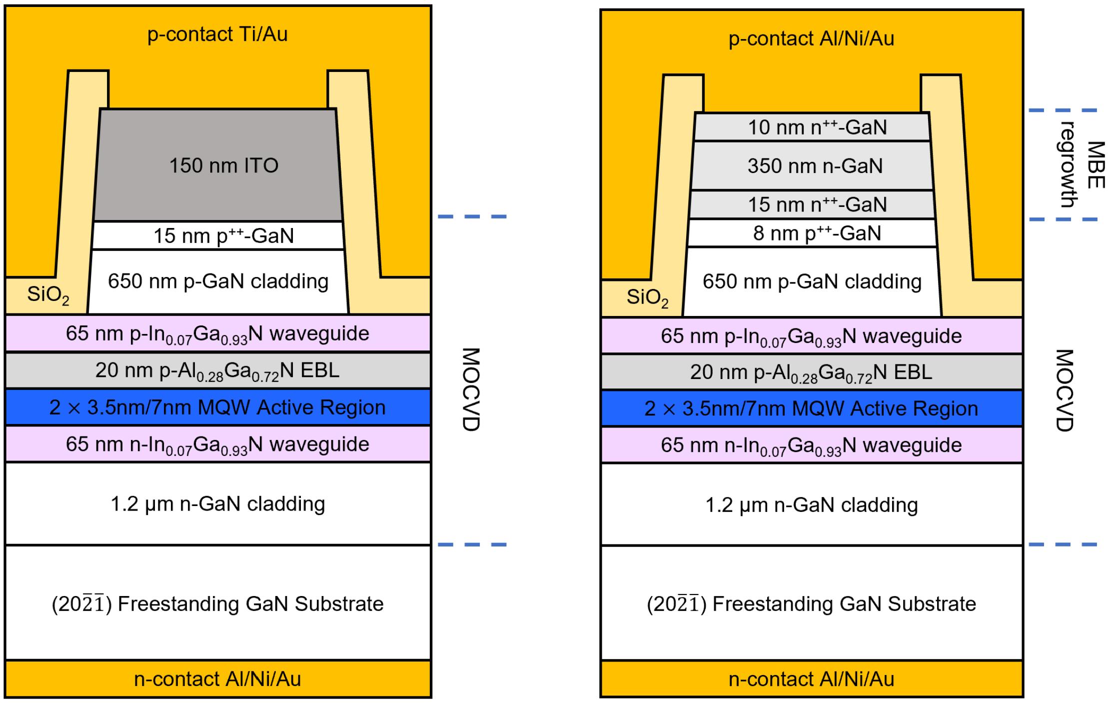

(a) (b)

Figure 2.1: Cross-sectional schematics of the fully fabricated edge-emitting LDs: (a) control devices using ITO p-contacts, and (b) devices with MBE-grown tunnel junction p-contacts. Reprinted with permission from Ref. [14] © Optica Publishing Group.

Of two wafers grown, one, to be given an indium tin oxide (ITO) p-contact, was removed from the MOCVD reactor and activated with a 15 minute anneal in air at 600°C. This wafer served as a control reference for evaluation of the performance of the tunnel junction laser diodes compared to traditional laser diodes. A second wafer was removed from the MOCVD reactor, activated under the same conditions, and then placed inside an ammonia MBE reactor, in which a 15 nm n^{++}-GaN layer, a 350 nm n-GaN cladding layer, and a 10 nm n^{++}-GaN contact layer were grown at about 725°C as measured by pyrometer.

On both wafers, ridges were defined by using a reactive ion etch (RIE) to etch to the top of the p-InGaN waveguiding layer. An SiO_2 insulating field oxide layer was then deposited immediately following the ridge-defining etch to allow for a subsequent liftoff

	Peak Wavelength (nm)	Threshold Current Density (kA/cm^2)	Voltage at 5 kA/cm^2 (V)	Differential Efficiency
ITO	440	2.3	7.2	34%
MBE-grown TJ	443	1.9	8.4	31%

Table 2.1: Device performance parameters of the LDs characterized in Figure 2.2a.

self-aligned to the ridge etch. Once the ridges were defined, the wafer with no tunnel junction regrowth was surface treated with concentrated HCl for 15 minutes. Then, a 150 nm ITO layer was blanket deposited on this wafer and the contact areas were defined by lithography and RIE etching. Contact pads of 30 nm Ti and 1000 nm Au were deposited on top of the ITO contacts. The wafer with the tunnel junction regrowth, following ridge definition, was surface treated for one minute in HCl following a lithography to define the contact areas. Then, top-side contacts to the n-GaN contact layers, consisting of 50 nm Al, 100 nm Ni, and 1000 nm Au, were deposited by electron beam evaporation.

Next, the laser facets were defined on all three wafers by a chemically assisted ion beam etch process [?]. No facet coatings were deposited. Before n-contact formation on the freestanding GaN wafer backsides, the wafer backsides were surface treated with a five-minute 400 W $SiCl_4$ etch, a one-minute buffered HF surface treatment, and a one-minute concentrated HCl surface treatment. Use of a $SiCl_4$ etch process has been shown to improve the quality of resulting n-contacts [41]. Then, n-contacts, consisting of 50 nm Al, 100 nm Ni, and 300 nm Au, were formed on both wafers by electron beam evaporation, completing the fabrication process.

2.2.2 Results and Analysis

The completed laser diode devices were tested at room temperature under two-point-probe pulsed conditions, using a pulse width of 1 μs and a duty cycle of 1%. Rather

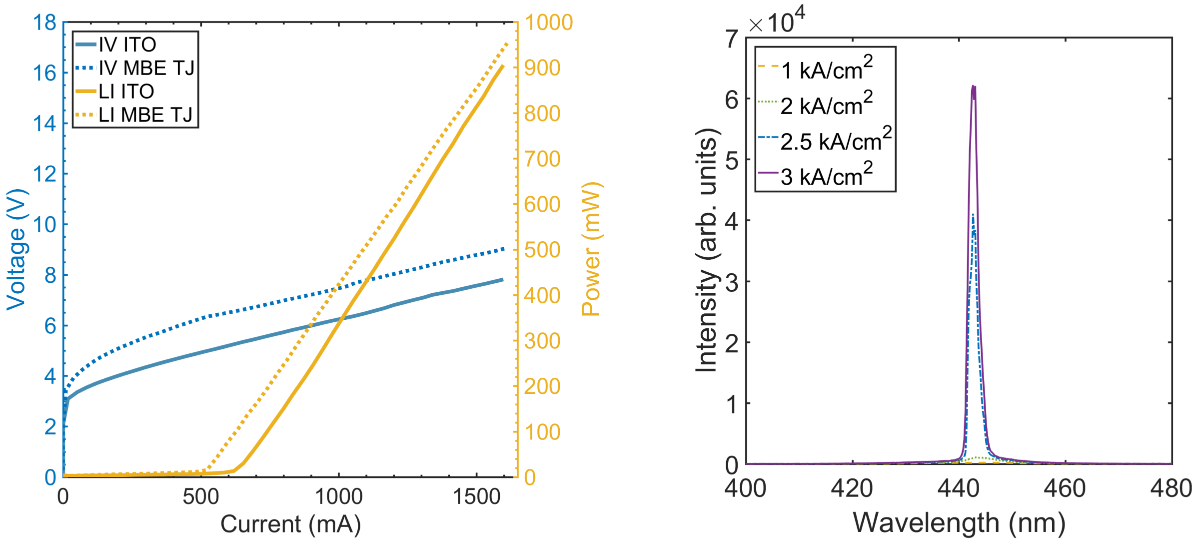

(a) (b)

Figure 2.2: (a) Current-voltage (IV) and combined two-facet light-current (LI) characteristic comparison of 1800 μm × 15 μm LDs, one with an ITO contact and the other with an MBE-grown tunnel junction contact, taken under pulsed conditions, and (b) a representative lasing spectrum of the LD with the MBE-grown TJ p-contact. Reprinted with permission from Ref. [14] © Optica Publishing Group.

than assume equal light output from each uncoated facet, the light output powers from both facets of each laser were measured and added together to give the total optical power output. The light-current-voltage characteristics of 1800 μm × 15 μm laser diodes from the wafers with ITO contact and MBE-grown tunnel junction contact devices were measured and are given in Figure 2.2a; the a representative lasing spectrum from an LD with an MBE-grown tunnel junction contact is given in Figure 2.2b. To characterize the overall performance of devices across these wafers, scatter plots of the wall-plug efficiencies and threshold current densities of all fabricated devices with ITO contacts and MBE-grown tunnel junction contacts are given in Figure 2.3. Last, device performance parameters extracted from this data are given in Table 2.1.

Overall, devices with MBE-grown tunnel junction contacts show lower threshold current densities than in devices using an ITO contact, as shown in Figure 3. We speculate

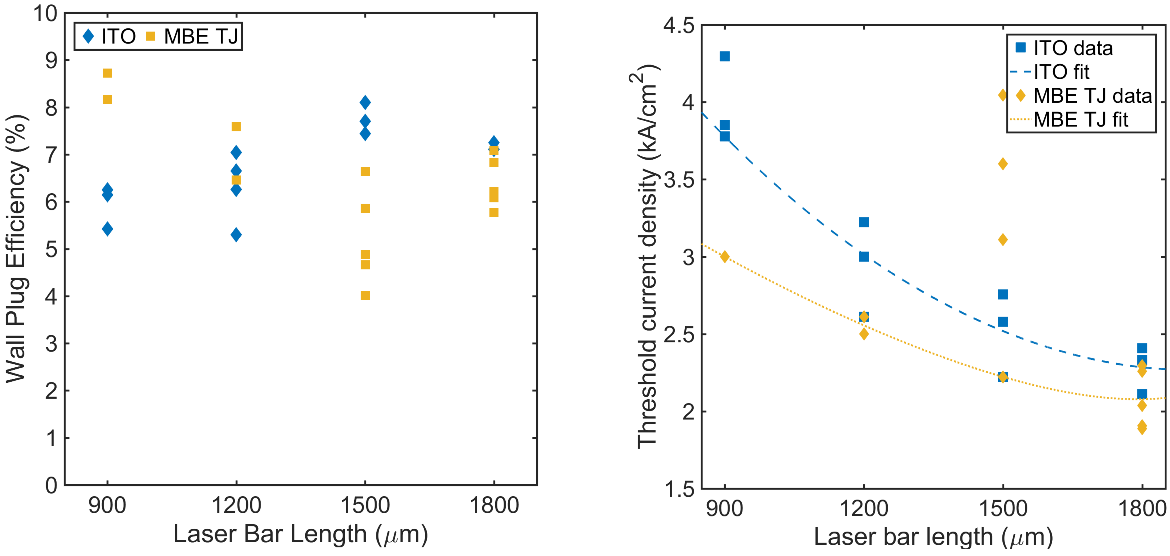

(a) (b)

Figure 2.3: Scatter plots of (a) wall plug efficiencies of all fabricated devices, and (b) threshold current density across all fabricated LDs, on the wafers with ITO contacts and MBE-grown TJ contacts. The LDs with the MBE-grown TJ p-contacts generally lower exhibit lower threshold current densities than the LDs with ITO p-contacts. Simple exponential fits excluding the outlier points, which are attributed to nonuniformities during the fabrication process, are provided just as a visual aid. Reprinted with permission from Ref. [14] © Optica Publishing Group.

this reduction in threshold current density may come from improved current spreading in the thicker tunnel junction regrowth allowing more uniform current injection throughout the laser ridges. Use of an MBE-grown tunnel junction regrowth is also shown to increase the turn-on voltage of the resulting laser diodes compared to ITO. This is consistent with previously published III-Nitride tunnel junction results [5, 7, 37, 11, 13]. The turn-on voltage increase is attributed to the tunnel junction itself, which is expected to need to operate under some fixed reverse bias "turn-on voltage" for efficient electron tunneling. This is corroborated by the similar differential resistances of the devices with an ITO layer and those with an MBE-grown tunnel junction.

2.3 Demonstration of III-Nitride Edge-Emitting Laser Diodes with Tunnel Junction Contacts Formed by MOCVD

2.3.1 Crystal Growth and Fabrication

In this work, LDs with MOCVD-grown tunnel junction p-contacts, with p-GaN activated through lateral diffusion of hydrogen through laser ridge sidewalls, were demonstrated; these LDs were grown, fabricated, and characterized for light-current-voltage data under pulsed conditions. Secondary ion mass spectroscopy (SIMS) measurements were then conducted to assist understanding of the results.

A cross-sectional schematic summarizing the laser diode epitaxial growth, the tunnel junction regrowth, and the fabricated laser diode structure is shown in Figure 2.4. The laser diode epitaxial structure below the tunnel junction was the same as that described in the previous section. Following removal from the MOCVD reactor, this wafer was surface treated for two-minutes with concentrated HF to remove surface magnesium, activated under the same conditions, and finally placed back into the MOCVD reactor, in which a 15 nm n^{++}-GaN layer, a 210 nm n-GaN cladding layer, and a 15 nm n^{++}-GaN contact layer were grown at growth temperatures varying between 800°C and 980°C. The concentrated HF surface treatment used here before the MOCVD tunnel junction regrowth was used to reduce the surface Mg concentration and thus reduce the Mg tail during subsequent growth of the n^{++}-GaN tunnel junction contact layer. Treatments of concentrated HF have been previously shown to have this effect [54]. Since Mg propagation has been shown to be greatly reduced by comparison in MBE regrowths [30], no HF surface treatment was used on the wafer that received the MBE regrowth.

On this wafer, ridges were also defined by using RIE to etch to the top of the p-InGaN

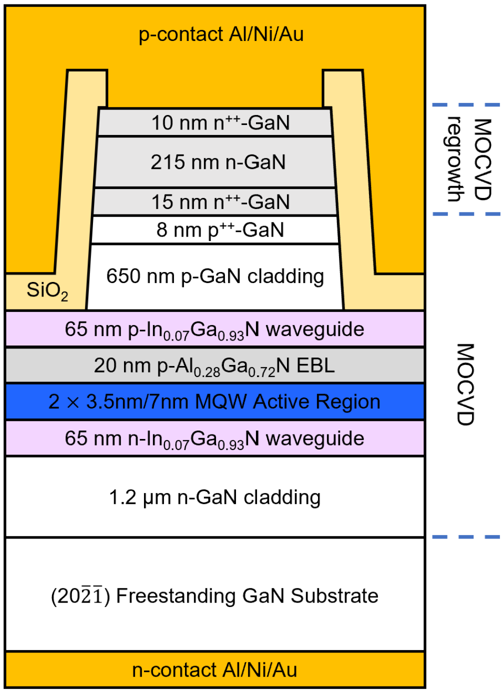

Figure 2.4: Cross-sectional schematics of the fully fabricated edge-emitting LDs with MOCVD-grown tunnel junction p-contacts. Reprinted with permission from Ref. [14] © Optica Publishing Group.

waveguiding layer. The photoresist used in this process step was stripped off immediately afterwards to allow the wafer to be annealed to reactivate the p-GaN that was passivated during the MOCVD regrowth. This reactivation step consisted of a 30 minute anneal in air at 700°C, a two-minute buffered HF surface treatment, and a second 30 minute anneal in air at 700°C. This activation step allowed for hydrogen reintroduced by the MOCVD tunnel junction regrowth to diffuse out of the ridge sidewalls and was expected to have fully activated the p-GaN in the 15 μm wide ridge [5, 7]. Following this step, SiO_2 was blanket deposited onto this wafer and vias through the SiO_2 to the tops of the laser ridges were defined by a HF wet etch. Laser facets were defined and backside contacts were deposited as described in the previous section.

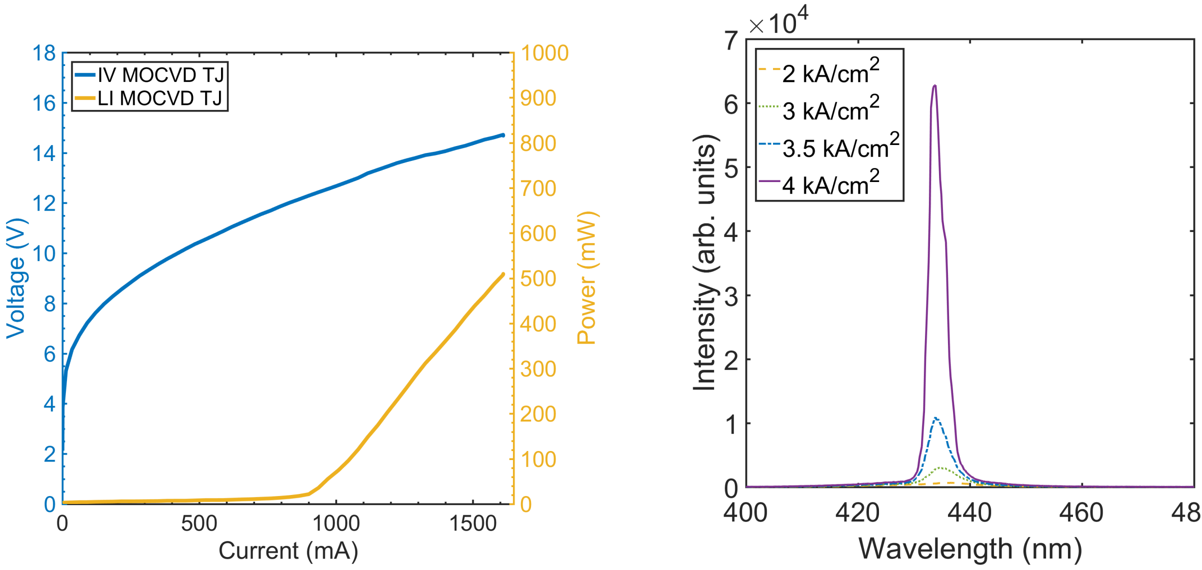

(a) (b)

Figure 2.5: (a) Current-voltage (IV) and combined two-facet light-current (LI) characteristic comparison of a representative 1800 μm × 15 μm LD with an MOCVD-grown tunnel junction contact, taken under pulsed conditions, and (b) a representative lasing spectrum from this wafer. Reprinted with permission from Ref. [14] © Optica Publishing Group.

2.3.2 Results and Analysis

The pulsed light-current-voltage characteristic of a representative 1800 μm × 15 μm LD with the MOCVD-grown tunnel junction contact is given in Figure 2.5a; a representative lasing spectrum from this wafer is given in Figure 2.5b. This device showed a threshold current density of 3.3 kA/cm^2, a voltage of 14 V at 5 kA/cm^2, and a differential efficiency of 25%. To characterize the overall performance of devices across this wafer, a scatter plot of the wall-plug efficiencies of all fabricated devices with MOCVD-grown tunnel junction contacts is given in Figure 2.6. Last, secondary ion mass spectroscopy (SIMS) data was taken from the MOCVD-grown TJ as well as the MBE-grown TJ; this data is pictured in Figure 2.7. We note that the devices with MOCVD-grown tunnel junction contacts were grown at a later time than the devices on the other two wafers and so are not otherwise compared side-by-side with those devices.

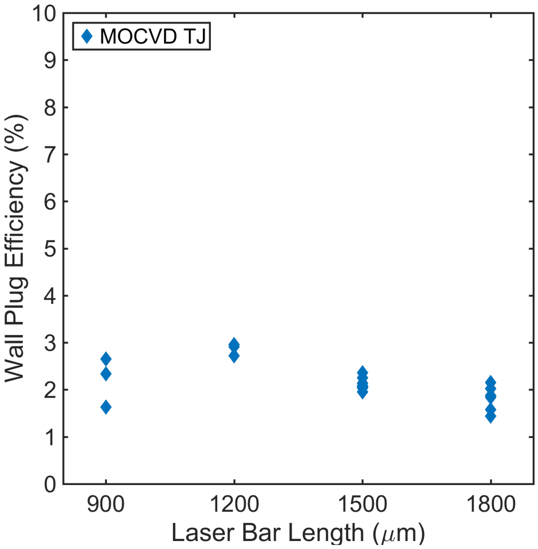

Figure 2.6: A scatter plot of all measured wall plug efficiencies for devices with MOCVD-grown tunnel junction contacts. Reprinted with permission from Ref. [14] © Optica Publishing Group.

Devices with MOCVD-grown tunnel junction contacts performed with high threshold current densities and operating voltages, and lower differential efficiencies overall, motivating SIMS measurements to investigate possible causes of this performance. As shown in the SIMS data in Figure 2.7, the falling edge profile of [Mg] in the MOCVD-grown tunnel junction regrowth is quite steep as intended, with a maximum fall rate of about 2.7 nm/decade. However, the [Mg] peak only reaches 5.3×10^{19} cm^{-3}, well under the calibrated value of 2×10^{20} cm^{-3}. As a result, [Mg] never exceeds [Si] in the highly-doped layers, which should enlarge the tunneling width. This doping profile is therefore expected to be the primary cause of the high operating voltage in devices with the MOCVD tunnel junction regrowth. Further investigation is needed to confirm the cause of this behavior, but because surface treatments involving HF have been shown to lower [Mg] peaks [7], we speculate that the HF treatment preceding the MOCVD tunnel junction regrowth removed an excessive amount of surface magnesium before it could incorporate during the regrowth, lowering the [Mg] profile peak.

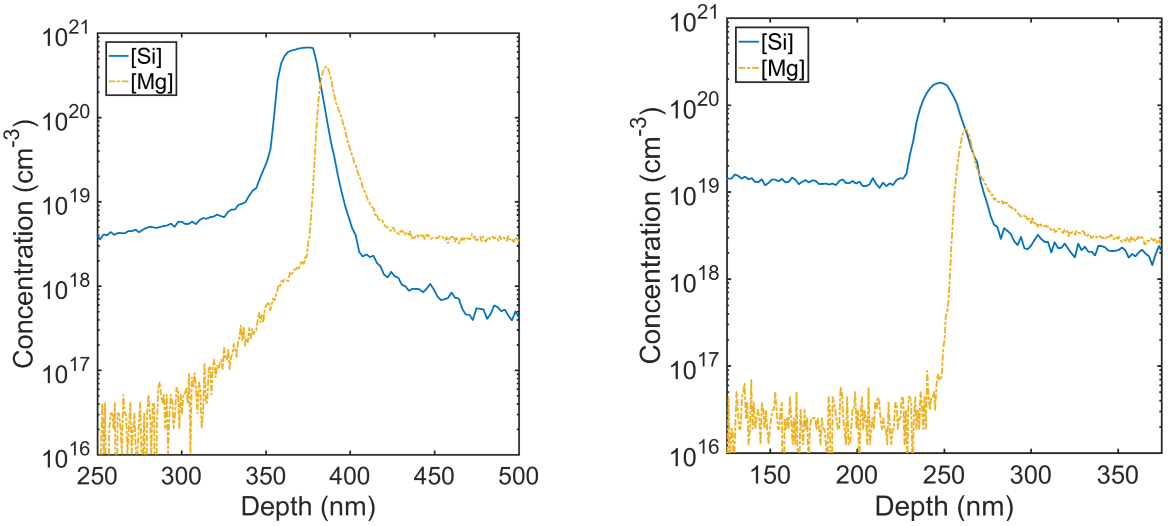

(a) (b)

Figure 2.7: SIMS profiles of [Si] and [Mg] near the regrowth interfaces of the tunnel junctions grown by (a) MBE and (b) MOCVD, plotted simultaneously for each wafer. Reprinted with permission from Ref. [14] © Optica Publishing Group.

Last, we speculate one possible cause of the low output power may be the higher temperatures sustained during the MOCVD tunnel junction regrowth of at or over 950°C for about 15 minutes. Relatively high temperatures were also sustained during the p-GaN sidewall activation unique to this wafer in which this wafer was annealed at 700°C for a cumulative total of one hour with the intention of achieving complete sidewall activation. By comparison, growth temperatures of about 725°C were used during the MBE tunnel junction regrowth. These sustained elevated temperatures are expected to have degraded the crystal quality of the InGaN quantum wells. This would reduce the carrier lifetime associated with nonradiative recombination and raise threshold current density.

2.4 Conclusions

This work demonstrated an MBE-grown tunnel junction contact for III-Nitride edge emitting laser diodes that achieved lower threshold current densities than control devices with ITO contacts. This work also demonstrated laser diodes using an MOCVD-grown tunnel junction contact fabricated using a sidewall activation method and a HF surface treatment to control the Mg memory effect. These laser diodes were characterized by high operating voltages and threshold currents and low differential efficiencies, indicating that there is room for further development of the involved growth, activation, and fabrication processes. Last, doping profiles measured by SIMS indicated that while Mg diffusion was successfully suppressed, further work is needed to optimize the MOCVD-grown tunnel junction doping profile for efficient tunneling.

Chapter 3

Designs for III-Nitride Edge-Emitting Laser Diodes with Tunnel Junction Contacts for Low Internal Optical Absorption Loss

This chapter is based on a paper titled “Designs for III-Nitride Edge-Emitting Laser Diodes with Tunnel Junction Contacts for Low Internal Optical Absorption Loss” by Shereen W. Hamdy, Steven P. DenBaars, James S. Speck, and Shuji Nakamura, at time of writing submitted on September 30 2021 to the SPIE journal Optical Engineering.

3.1 Motivation

Significant progress has been made in recent years towards efficiency improvements for the III-Nitride edge-emitting laser diode (LD) [21, 28, 29]. Still, one of the contributing factors to internal optical absorption losses in many III-Nitride LD designs is the optical absorption associated with p-type layers [31, 3] and transparent conducting oxide layers [92, 93, 94]. Unmitigated, the absorption losses of these layers contribute to the threshold gain, increase the threshold current density, and reduce the differential efficiency, and thus lower the wall-plug efficiency in LDs. This limits the LD's viability for relevant emerging applications in efficient illumination, high-speed Li-Fi communication, and other technologies.

In this work, we use degrees of freedom unique to LDs utilizing a tunnel junction contact to investigate LD designs that minimize the internal optical absorption loss contributions from the p-side of the epitaxial stack. We model these devices using the transfer matrix method [95, 96, 97] to calculate depth profiles of the lasing mode and internal optical absorption losses. We support these models with additional band diagram modeling in the Bandeng software package [98]. We ultimately locate pathways towards minimization of the p-side contributions to loss made uniquely possible by the tunnel junction contact. These pathways show potential for substantial reductions in internal optical absorption loss in many real LD designs.

3.2 Background

The models used in this study estimate the dimensions of the tunnel junction depletion region using the analytical expressions for the p-type and n-type depletion widths in pn junctions, which are provided below:

$$w_p(V_{\mathrm{bi}} - V_{\mathrm{bias}}) = \sqrt{\frac{2\epsilon}{q_0}(V_{\mathrm{bi}} - V_{\mathrm{bias}})\left[\frac{\mathrm{N_D}}{\mathrm{N_A}(\mathrm{N_D} + N_A)}\right]} \tag{3.1}$$

$$w_n(V_{\mathrm{bi}} - V_{\mathrm{bias}}) = \sqrt{\frac{2\epsilon}{q_0}(V_{\mathrm{bi}} - V_{\mathrm{bias}})\left[\frac{\mathrm{N_A}}{\mathrm{N_D}(\mathrm{N_D} + \mathrm{N_A})}\right]} \tag{3.2}$$

In the depletion region of a pn junction, all acceptors and donors are fully ionized (neglecting effects at the depletion edges). Thus, for the case of GaN, all Mg acceptors are in a single negative charge state corresponding to $\mathrm{N_A^-}$ and all donors are in a positive charge state $\mathrm{N_D^+}$. Thus in the depletion region there are no neutral acceptors available for optical absorption from deeper valence band states nor are there any neutral donors, nor any free holes or electrons. This means thicknesses of the p++-GaN and n++-GaN layers of the tunnel junction that minimize the internal optical absorption loss are expected to be close to the theoretical junction depletion widths such that the numbers of neutral dopants and undepleted free carriers are minimized. However, in real devices, profile spreading effects like the Magnesium (Mg) memory effect [54] and Mg diffusion through threading dislocations [52, 53] in III-Nitride tunnel junction layers grown by metal-organic chemical vapor deposition, as well as finite turn-on and turn-off slopes of dopant profiles, and finite turn-on slopes of the depletion profiles associated with the Debye lengths comprising a significant portion of junction layer thicknesses, complicate the dopant profiles and depletion profiles of the tunnel junction somewhat. Additionally, the built-in potential of the tunnel junction must be fully dropped within the highly-doped tunnel junction layers. This constraint ensures the tunnel junction depletion region does not extend into lower-doped layers where a greater material thickness would be required to drop the remaining potential. This situation would result in a wider depletion region and so a wider tunneling distance, reducing electron tunneling probabilities. A higher reverse bias operating voltage would be needed to compensate, yielding a negative impact on the voltage performance of the tunnel junction if this constraint is not met.

A viable III-Nitride tunnel junction implementation must also address activation of p-type material, which is known to be passivated by hydrogen in MOCVD growth conditions in which hydrogen is present as a byproduct of ammonia decomposition and often also as a carrier gas [36]. This passivation renders Mg atoms inactive as dopant impurities, reducing the acceptor dopant concentration N_A. This increases the width of the depletion region and so increases the electron tunneling distance of the tunnel junction. As a result, tunnel junction devices with inactive p-type material typically have high operating voltages. In many studies, the tunnel junction is grown by molecular beam epitaxy (MBE), where growth conditions in MBE maintain a sufficiently low pressure of hydrogen and so preserve activation of p-type material [44]. In other studies, the tunnel junction is grown by MOCVD and subsequently reactivated through lateral diffusion of hydrogen through the sidewalls of partially or fully fabricated devices. This latter process has been achieved for multiple different device types and geometries [5, 48]. Additionally, selective area tunnel junction regrowth processes were also recently demonstrated, in which p-type material is efficiently activated through joint lateral-vertical diffusion towards vias in the tunnel junction regrowth [46, 47]. As such, in this analysis, we assume devices with fully activated p-type material.

In this analysis, we treat any profile spreading in the dopant and depletion profiles, relative to the epitaxial designs and analytical solutions, as occurring on length scales much smaller than the characteristic length scale of the lasing mode profile, and so (1) we assume this profile spreading is negligible in the context of an analysis of internal optical absorption losses; (2) we treat these profile spreading effects as problems of implementation outside the scope of this paper that are the subject of ongoing research [54, 52, 53, 51]. We consider the depletion region to be of size defined by (3.1) and (3.2) and to be depleted of free carriers and unavailable to contribute to absorption. Because the size of the depletion region is dependent on the applied bias across the tunnel junction, the contribution of the tunnel junction to loss is then dependent on the bias across the tunnel junction as well, and so we evaluate tunnel junction depletion width values at a reverse bias across the tunnel junction of 1.5 V that is typical for operating current densities used in LDs. This operating bias has been observed as an approximately constant (at operating current densities) increase in operating voltage in an LD with a tunnel junction contact over that of an otherwise identical LD fabricated instead with an ITO p-contact and operated at the same current density [11, 14]. Band diagrams are modeled in the Bandeng software package [98] to verify that the built-in potential drop of the tunnel junction is fully contained within the highly-doped layers in these designs. Last, we assume fully activated p-type material as has already been demonstrated in the various III-Nitride tunnel junction studies cited here.

3.2.1 Designs

We modeled five illustrative designs that should result in reduced internal optical absorption loss. The first, model A, shown in Figure 3.1a, is an indium tin oxide (ITO) clad LD with an epitaxial stack below that is typical for III-Nitride LDs [99, 92]. To maintain consistency with the other models, we treat the upper 4 nm of the p++-GaN contact layer as depleted of free carriers, where the theoretical depletion width of p-GaN at an ITO contact may be calculated based on the relevant physical parameters of both materials [38, 33].

Model B, shown in Figure 3.1b, replaces the ITO layer with a tunnel junction stack typical to tunnel junction contact implementations [83]. This stack consists of a 10 nm n++-GaN layer that completes the tunnel junction, a 400 nm n-GaN layer, and a 10 nm n++-GaN contact layer. Using equations 3.1 and 3.2 and the dopant concentrations in Table 3.1, we assume the first 3.7 nm of the n++-GaN tunnel junction layer, and the last 1.8 nm of the preceding p++-GaN layer, to be depleted of free carriers and therefore unavailable to contribute to absorption, as discussed in the previous section.

Model C, shown in Figure 3.1c, aims to show the effects of optimizing the tunnel junction thickness for low loss and reducing the p-GaN thickness in tandem. First,

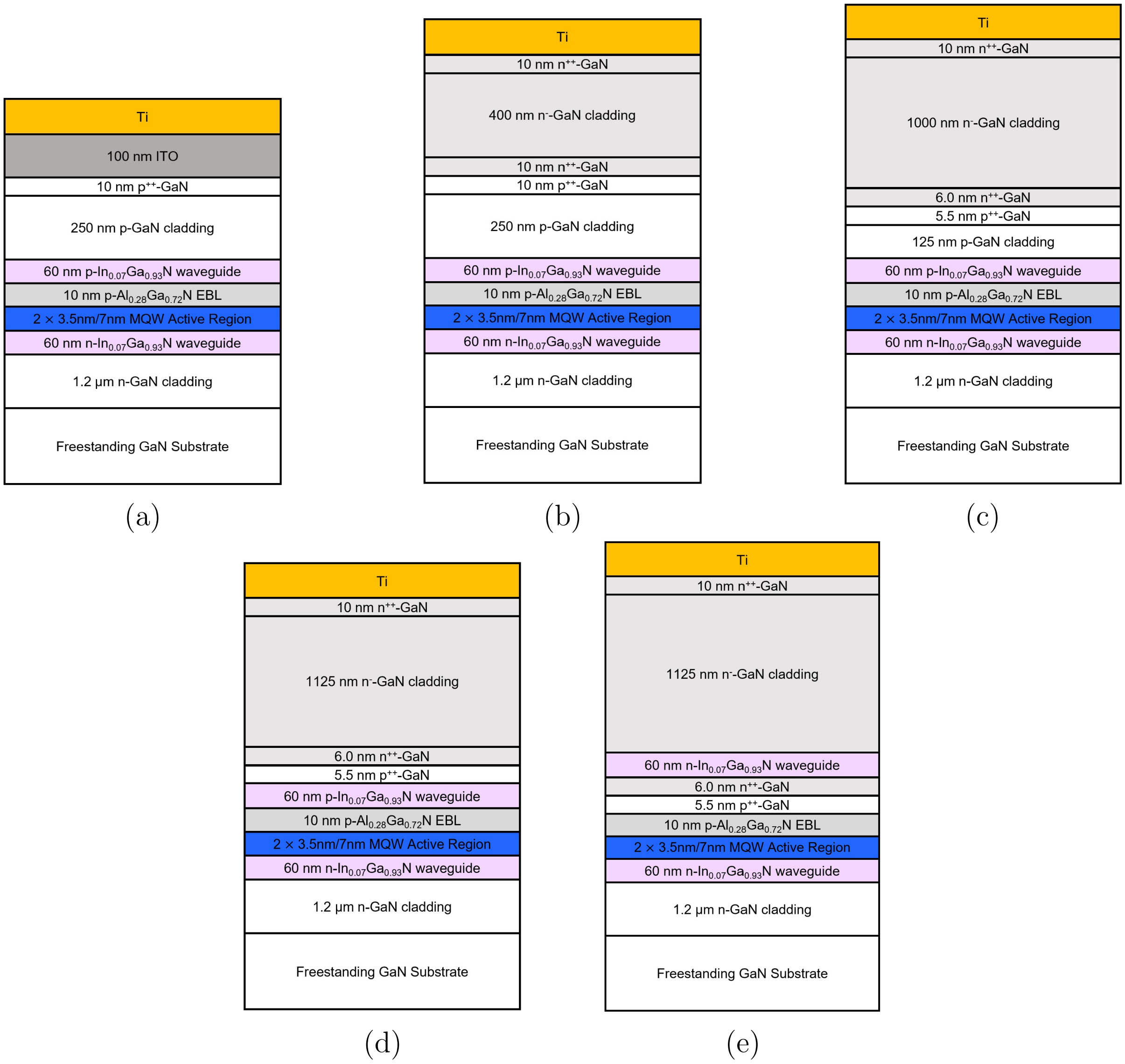

(a) (b) (c)

(d) (e)

Figure 3.1: Visual representations (not to scale) of the LD epitaxial designs modeled: (a) an ITO-clad LD; (b) the former LD with the ITO layer replaced by a typical implementation of a tunnel junction contact [83]; (c) a redesign of model B found to minimize internal optical absorption losses; (d) a redesign of model B that eliminates the p-GaN cladding layer; (e) a redesign of model D that replaces the p-InGaN waveguiding layer with an n-InGaN waveguiding layer located above the tunnel junction.

model C reduces the thickness of the second n-GaN cladding layer to 1000 nm, from 400 nm in model B. This moves the metal contact well outside of the optical mode to reduce its contribution to internal optical absorption. Model C also halves the thickness of the

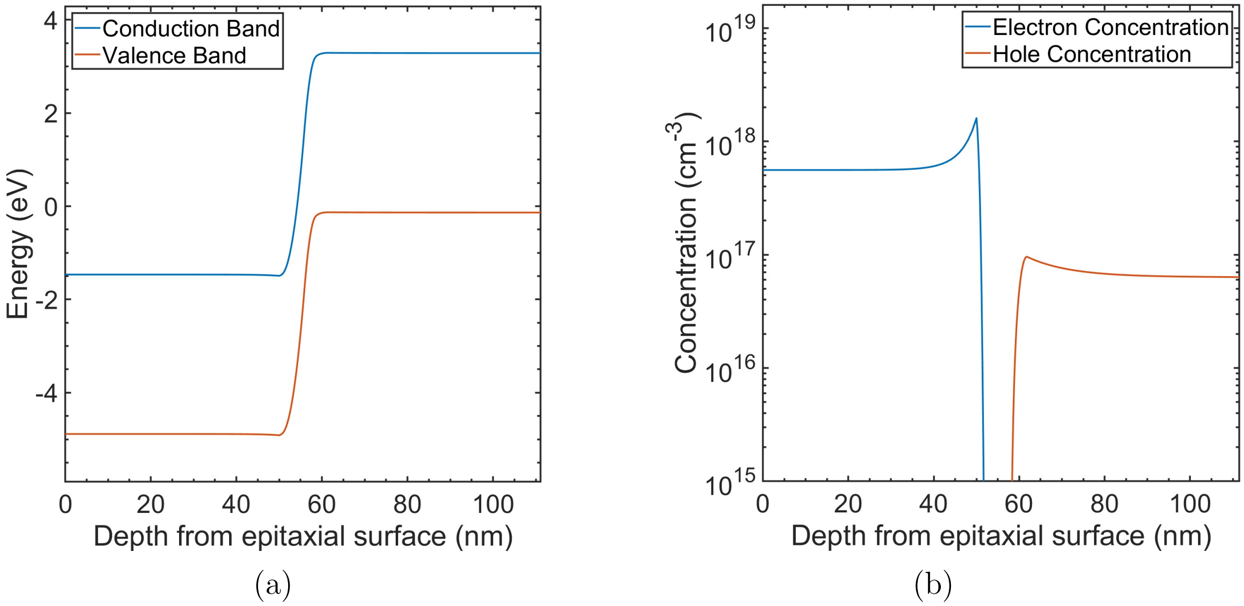

(a)

(b)

Figure 3.2: Plots of (a) the band diagram and (b) the carrier concentrations in the tunnel junction used in model C, evaluated at 1.5 V of reverse bias, as modeled in the Bandeng software package [98]. This model demonstrates that the extent of the tunnel junction depletion region in model C is not expected to significantly extend into the lower-doped regions outside of the tunnel junction.

p-GaN cladding layer located above the active region to 125 nm, from 250 nm in model B, in order to reduce its contribution to optical absorption loss as well. Last, we model the tunnel junction in model C to be as thin as possible while still supporting the built-in potential drop within the highly-doped layers as previously discussed. Band diagram simulations in the Bandeng software package [98], pictured in Figure 3.2, were used to find the minimum p++-GaN and n++-GaN thicknesses satisfying these conditions as about 5.1 nm and 5.5 nm, respectively. In practical consideration of uncertainties in measured growth rates and doping levels in common crystal growth techniques, and the bias dependence of the depletion widths in a PN junction, slightly larger thicknesses of 5.5 nm and 6.0 nm were used for the p++-GaN and n++-GaN layers, respectively. As in model B, we assume the analytical depletion region, 1.8 nm wide on the p side of the junction and 3.7 nm wide on the n side of the junction, to be depleted of free carriers

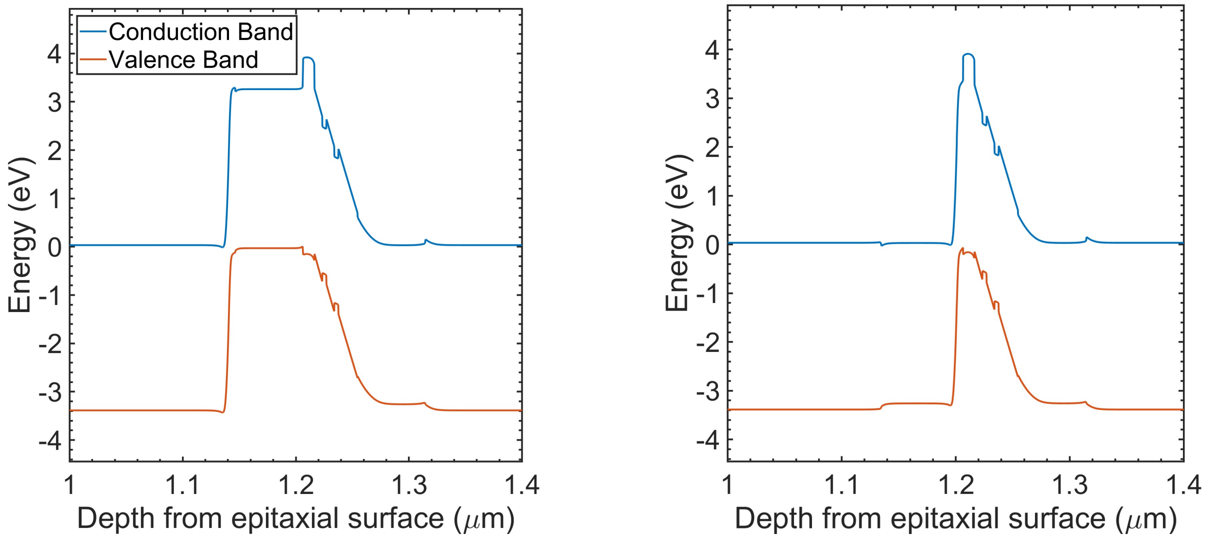

(a)

(b)

Figure 3.3: Equilibrium band diagram plots of regions of interest in (a) model D and (b) model E, as modeled in the Bandeng software package [98]. These models show that the full built-in potential is dropped across both the tunnel junction and the active region in both models, supporting the presence of both electrons and holes for conduction and optical emission even as the amount of p-type material is reduced.

and therefore unavailable to contribute to absorption.

Last, Model D, shown in Figure 3.1d, is a version of model C that eliminates the 125 nm p-GaN cladding layer and adds the same thickness to the upper n-GaN cladding layer; Model E, shown in Figure 3.1e, is a version of model D that further eliminates p-type material by additionally replacing the p-InGaN waveguiding layer with an n-InGaN waveguiding layer above the tunnel junction. Further band diagram simulations, pictured in Figure 3.3, were done to verify that the remaining amount of p-type material would be enough to drop the full built-in potential of both the tunnel junction and the active region.

All features not mentioned in these descriptions are assumed to be identical between all three designs. Parameters corresponding to the $(20\bar{2}\bar{1})$ crystal plane were used in all models, corresponding to the LD designs on which these models were based [14, 99]. The doping levels for the epitaxial layers considered in this study are provided in Table 3.1. The emission wavelength was assumed to be 440 nm in all devices, and absorption values were calculated using the parametrizations in [31]. These designs were modeled using the transfer matrix method, which in this implementation yields lasing mode distributions and ultimately one-dimensional layer-by-layer profiles of internal optical absorption losses [95, 96, 97].

3.3 Results

Plots showing the calculated lasing mode profiles and internal optical absorption profiles of each design are provided in Figure 3.4, and optical absorption losses associated with individual layers of interest are provided in Table 3.1. The total modeled internal optical absorption losses are 8.14 cm^{-1} in model A (the TCO contact LD), 8.41 cm^{-1} in model B (the unoptimized tunnel junction contact LD), and 7.12 cm^{-1} in model C (the optimized tunnel junction contact LD). Model D, which eliminates p-GaN cladding layer, sees a total of 8.93 cm^{-1} of loss; model E sees a total of 8.05 cm^{-1}. An additional visualization of the material absorption coefficient in the vicinity of the tunnel junction in models B and C is provided in Figure 3.5.

3.4 Discussion

These models demonstrate the possibility for metal and TCO contacts to contribute avoidable internal loss, as illustrated in Figures 3.4a and 3.4b. We also note that the reduced refractive index of ITO relative to that of GaN assists in confining the mode in model A away from the metal contact. As a result, the loss contribution from the metal contact in model B increases relative to model A by 0.46 cm^{-1}, even at a greater total

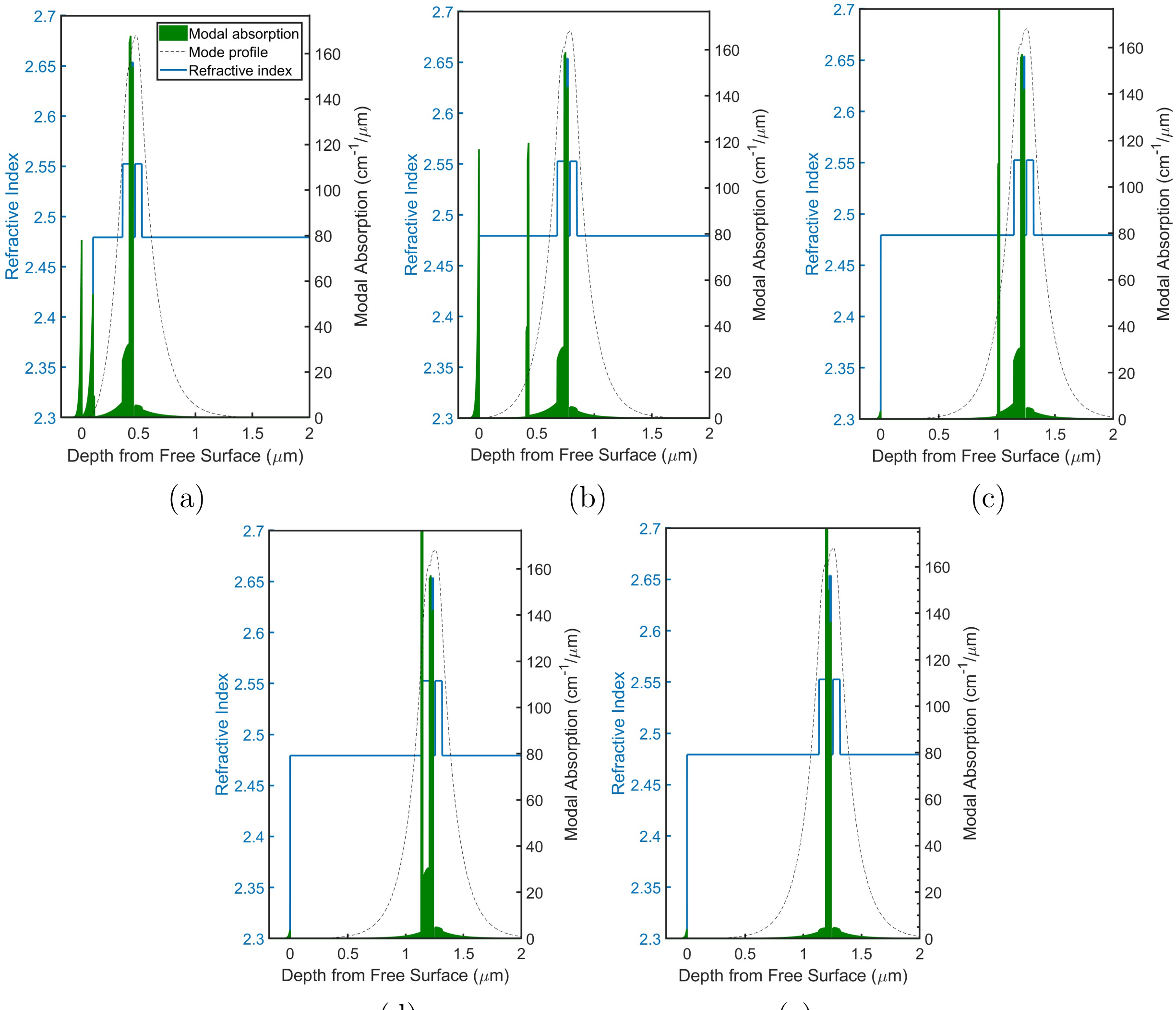

(a) (b) (c)

(d) (e)

Figure 3.4: Depth profiles of absorption loss, refractive index, and the lasing mode (in arbitrary units) for each of the LD designs modeled: (a) the ITO-clad LD; (b) the former LD with the ITO layer replaced by a typical implementation of a tunnel junction contact [83]; (c) a redesign of model B found to minimize total internal optical absorption losses, total internal loss 7.12 cm^{-1}; (d) a redesign of model C that eliminates the p-GaN cladding layer; (e) a redesign of model D that replaces the p-InGaN waveguiding layer with an n-InGaN waveguiding layer located above the tunnel junction. We note that the clipped peaks in the absorption profiles in Figures 3.4c, 3.4d, and 3.4e correspond to the nearly-fully-depleted, highly-doped tunnel junction close to the active region that causes two tall but narrow spikes in the absorption profile. These spikes peak at about 317, 802, and 936 cm^{-1}/μm in the undepleted p++-GaN, and peak at about 110, 278, and 349 cm^{-1}/μm in the undepleted n++-GaN, in Figures 3.4c, 3.4d, and 3.4e, respectively.

Layer	Dopant conc. (cm^{-3})	Model A	Model B	Model C	Model D	Model E
		Loss values by layer (cm^{-1})				
Metal	—	0.925	1.39	0.0423	0.0423	0.0489
ITO	—	1.24	—	—	—	—
Upper n-GaN cladding	10^{18}	—	0.0397	0.141	0.357	0.381
n-InGaN	10^{18}	—	—	—	—	0.251
n++-GaN	10^{20}	—	0.245	0.257	0.649	0.820
p++-GaN	2.0×10^{20}	0.052	0.950	1.15	2.90	3.43
p-GaN	1.7×10^{18}	0.595	0.765	0.550	—	—
p-InGaN	5.0×10^{18}	1.78	1.74	1.73	1.73	—
Total loss (cm^{-1})		8.14	8.41	7.12	8.93	8.05
Confinement factor (%)		2.13	2.00	1.97	1.97	1.89

Table 3.1: Calculated loss contributions from metal, ITO, and epitaxial layers of interest for each LD model. Values of the total internal optical absorption loss, confinement factor, and dopant concentrations of epitaxial layers of interest are also provided.

distance from the active region.

This model subsequently shows how this loss component may be reduced by spatially separating the topside contact farther from the active region to reduce mode overlap. In LDs that do not use a tunnel junction contact, this typically requires an increase in the thickness of the p-GaN cladding layer, which comes with a voltage increase associated with the resistivity of p-GaN [2, 100] and leaves unmitigated the optical absorption loss associated with the p-GaN cladding layer itself [3, 31]. In LDs using a tunnel junction contact, the aforementioned spatial separation may be achieved by placing a lightly-doped n-type cladding layer between the tunnel junction and metal contact. This separates the metal contact from the mode such that it has negligible contribution to optical absorption

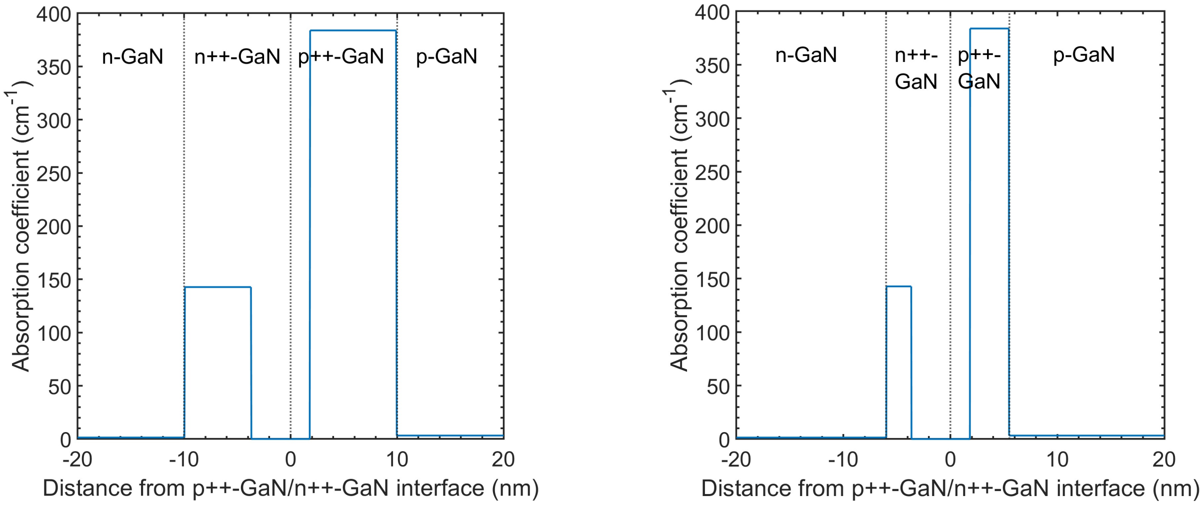

(a)

(b)

Figure 3.5: Plots of the material absorption coefficient in the vicinity of the tunnel junction (a) in model B, (b) in model C. The reduction in the thickness of the high-absorption-coefficient tunnel junction layers from model B to model C mitigates the increase in optical absorption loss due to increased proximity to the active region. We note our previous assumption that the theoretical depletion region is depleted of free carriers and unavailable to contribute to optical absorption loss, reflected in the model as a region of zero absorption coefficient within the tunnel junction. We also note that, while models D and E alter the immediate environment of the tunnel junction, the p++-GaN and n++-GaN composition and doping levels are not adjusted, and so the p++-GaN and n++-GaN absorption values in Figure 3.5b apply to these models as well.

losses with a minimal associated increase in absorption, shown in Figure 3.4c. While the metal and ITO layers combined contribute 2.17 cm^{-1} in model A, and the metal contributes 1.39 cm^{-1} in model B, in model C the metal contributes 0.0423 cm^{-1} of loss. We note that the loss contribution from the upper n-GaN cladding layer increases from 0.0397 cm^{-1} in model B to 0.141 cm^{-1} in model C due to the increased thickness of this layer, as well as the reduced confinement of the lasing mode relative to model B: without a metal layer present in the same vicinity to the active region, the lasing mode reaches farther into the p-side of the device.

Reducing the thickness of the tunnel junction also yields improvements in absorption. As previously explained, this optimization minimizes the presence of free carriers in the tunnel junction that drive the associated contribution to internal optical absorption loss. As shown in Table 1, the tunnel junction contributes 1.20 cm^{-1} in model B with the unoptimized tunnel junction contact. In the LD utilizing the reduced-thickness tunnel junction, the tunnel junction contributes an increased 1.41 cm^{-1} of absorption because of its location closer to the active region, but this 0.21 cm^{-1} loss increase was mitigated by the optimization of the tunnel junction and furthermore is matched in the model by a 0.215 cm^{-1} loss reduction corresponding to the reduced thickness of the p-GaN cladding layer in model C. In other words, designs that achieve a sufficiently low-loss tunnel junction allow the thickness of the p-type cladding layer above the active region to be reduced, yielding associated benefits for operating voltage, while maintaining a minimal net loss penalty despite the increased proximity to the active region of the highly doped tunnel junction.

Model D shows that the p-GaN may not be eliminated entirely from model C without causing a net increase in loss from increased overlap of the lasing mode with the highly-doped tunnel junction. However, model E shows that this increase may be mitigated by replacing the p-InGaN waveguiding layer with an n-type waveguiding layer above the tunnel junction. While this increases the proximity of the tunnel junction to the mode profile peak, this also distances the relatively absorbing InGaN layer from the mode profile peak and eliminates additional p-type material, yielding an overall net reduction in loss compared to model D.

The total loss values in models D and E still exceed the value achieved in model C. However, low loss and a minimum of p-type material may still be achieved simultaneously by introducing a thin UID GaN spacer layer immediately above the active region. For example, introducing a 30 nm UID GaN spacer layer yields a 0.87 cm^{-1} reduction in total internal loss. A plot of the total internal absorption loss of model E versus the thickness of this layer is provided in Figure 3.6.

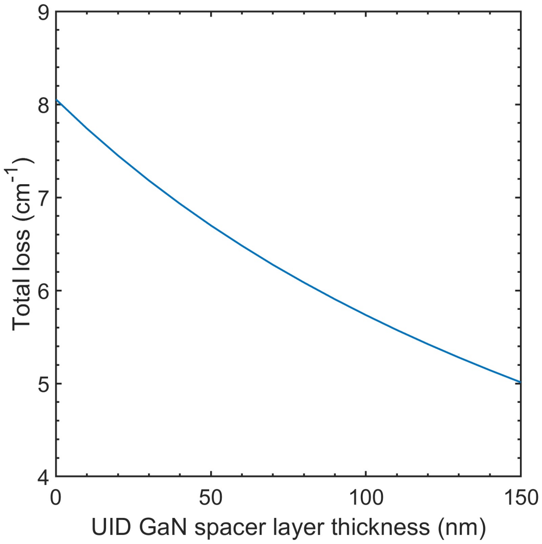

Figure 3.6: Total internal optical absorption loss in model E as a function of the thickness of a UID GaN spacer layer located immediately above the active region. With 0 nm of UID GaN (the amount used by default for reported loss values and band diagrams), the total loss is 8.05 cm^{-1}; with 30 nm, 7.18 cm^{-1}; with 150 nm, 5.01 cm^{-1}.

We note at this point that the model shows that while using InGaN for the UID spacer layer instead of GaN would additionally increase confinement, it would also increase total loss instead of reducing it as desired: a 30 nm $In_{0.07}Ga_{0.93}N$ layer increases confinement to 2.08% (up from 1.89%) but increases total internal loss by about 0.19 cm^{-1} to 8.24 cm^{-1}, indicating a loss penalty from stronger confinement causing greater mode overlap with absorbing layers near the active region such as the tunnel junction. We also expect that a UID spacer layer may add some voltage to devices, creating a trade-off situation between loss and voltage. Future calculations will evaluate the effect of this layer on voltage at different doping levels and thicknesses and also include full drift-diffusion calculations of the operating voltage.

Last, we address confinement factor: Model B shows a reduction in confinement factor relative to model A due to the ITO layer (and its associated refractive index contrast) having been removed from the structure and replaced with a thicker GaN stack. Models

C and D show subsequently lower confinement factors due to increased thickness of GaN material above the active region, and model E shows a further decrease in confinement factor with the InGaN waveguiding layer spatially separated from the active region. The confinement factor can be recovered through the use of off-ridge contact designs, as discussed in Ref. [16]. For example, a version of model E excluding all material above the bottom 400 nm of the upper n-GaN cladding layer shows a confinement factor of 3.68%, which is significantly higher than the other values reported here. We associate this increase with increased proximity of the GaN-air interface and its associated refractive index contrast; this interface can be located relatively close to the active region in off-ridge contact designs. This model also shows a total internal optical absorption loss of 8.31 cm^{-1}, up from 8.05 cm^{-1} in model E, showing a similar loss penalty effect from increased confinement as was discussed earlier. We note that two-dimensional versions of this model and the other models discussed here are needed to capture the full effect of the off-ridge design as well as to account for lateral confinement, and this will be the subject of future calculations.

3.5 Conclusions

In this study, five edge-emitting laser diode designs were modeled using the transfer matrix method, yielding depth profiles of the lasing mode and internal optical absorption losses and individual loss components associated with each epitaxial layer. These show that, in LDs with tunnel junction contacts, significant improvements in total optical absorption losses can be achieved through optimization of the tunnel junction, vertical and/or lateral distancing of the metal contact from the optical mode, and reduction of p-type material. These practices are unique to the design space available to LDs with tunnel junction contacts, and they illuminate pathways to potential future efficiency gains.

Chapter 4

Tunnel Junction Enabled Surface Gratings for III-Nitride Laser Diodes

This chapter is based on, at the time of writing, unpublished work that was presented as part of the PhD Qualifying Exam associated with this dissertation, and additional work that expands on the same.

4.1 Introduction

In optics and photonics, the photonic crystal, or distributed feedback (DFB) grating, is a periodic structure often constructed along the length of an edge-emitting LD. Two general schematic representations of a distributed feedback grating are given in Figure 4.1. The DFB grating couples a periodic refractive index profile to the optical mode of the laser diode, enabling it to strongly select for constructive feedback at one wavelength corresponding to the grating period. As a result, a DFB grating confers high spectral

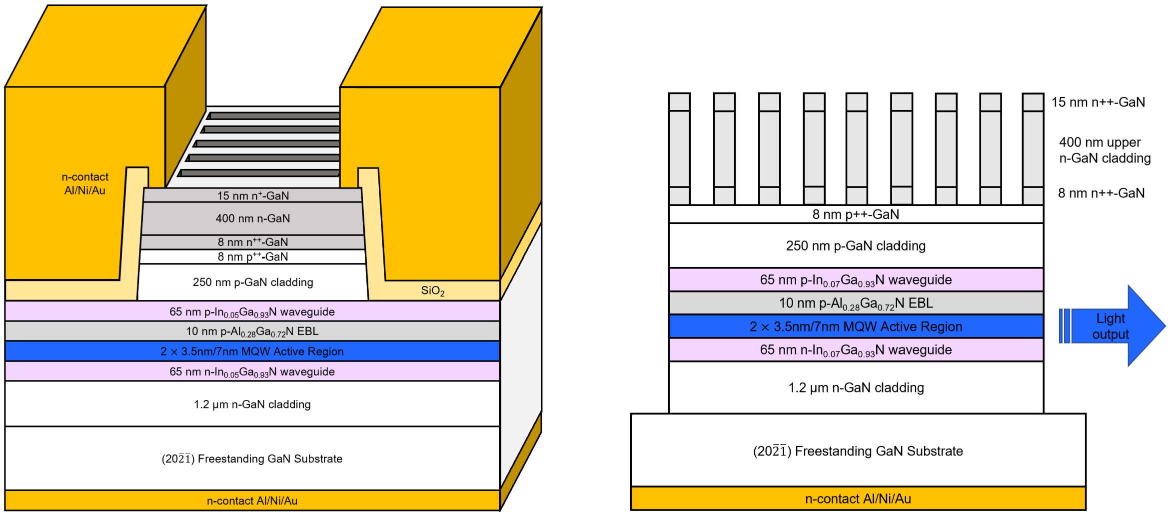

(a) (b)

Figure 4.1: (a) Three-dimensional and (b) cross-sectional example schematics of a laser diode with a distributed feedback grating, following the design considered in this work.

purity to an LD [101]. The III-Nitride DFB LD then shows potential for applications such as communications and fundamental science, where high-spectral-purity light is desired. Various DFB grating implementations have been realized in the III-Nitrides materials system, such as buried gratings [102], surface gratings formed from indium tin oxide (ITO) [103] and from photoresist [104], sidewall gratings formed in the laser ridge [105], higher-order gratings [105, 106], and a molecular-beam-epitaxy-grown DFB LD incorporating a tunnel junction [9].

Laser diodes with DFB gratings still possess limitations, however, including in the III-Nitride materials system. Assuming a square grating, the first-order grating period of a device is given as a function of wavelength and refractive indices by [23]

$$\Lambda = \frac{\lambda_0}{4}\left(\frac{1}{\bar{n}_1} + \frac{1}{\bar{n}_2}\right) \approx \frac{\lambda_0}{2\bar{n}} \tag{4.1}$$

where λ_0 is the emission wavelength in vacuum, the $\bar{n}_i$ are the effective refractive indices of each of the two vertical cross-sections of the DFB grating, and $\bar{n}$ is the average of the two $\bar{n}_i$. Given an emission wavelength of 440 nm for blue-emitting III-Nitride devices and a typical value of the effective refractive index $\bar{n}$ from those modeled in this study, the first-order grating period is around 89 nm, necessitating grating formation by electron beam lithography. This adds significant time and complexity to fabrication processes, and in commercial devices adds significant cost as well.

Higher order gratings, with grating periods equal to an integer multiple of the first-order grating period as $m\Lambda$, can be considered as a means to potentially avoid electron beam lithography by increasing the feature size of the grating, and the grating duty cycle γ, i.e. the proportion of each grating period taken up laterally by an individual ridge, offers additional flexibility. However, increasing the grating order m, or using an asymmetric duty cycle in which $\gamma \neq 0.5$, reduces the coupling κ to the lasing mode as [23, 107]

$$\kappa = \frac{2|\bar{n}_1 - \bar{n}_2|}{\lambda_0} \frac{\sin(\pi m \gamma)}{m} \tag{4.2}$$

In DFB LD designs, it is important to maintain κL_g near unity, where L_g is the length of the DFB grating. If the coupling is not strong enough and κL_g is too low, then the DFB grating only provides weak reflectivity. If coupling is too strong and κL_g is too high, the stopband (i.e. wavelength selectivity) of the grating starts to broaden, which allows side modes of the LD cavity to contribute to emission and so reduces the spectral purity of the emitted light [23].

The tunnel junction provides a means to significantly increase DFB grating coupling and so create a coupling overhead allowing higher-order gratings. If the bottom of the DFB grating is placed at the metallurgical junction of the tunnel junction, i.e. the interface between p-type and n-type material, a TJ-DFB LD can realize multiple benefits simultaneously:

- The DFB grating and tunnel junction layers may be formed simultaneously using a selective area regrowth process in which (1) the growth interrupt is placed at the tunnel junction interface and (2) the regrowth areas correspond to the teeth of the DFB grating.

- By locating the bottom of the DFB grating at the tunnel junction interface, p-type material which would have been passivated by reintroduction to MOCVD growth conditions [36] may be straightforwardly reactivated with an anneal where evacuation of hydrogen is achieved through a combination of lateral and vertical diffusion to the free p-type surface at the bottom of the grating. Similar schemes have already been demonstrated in other tunnel junction devices [5, 45, 46, 47, 48], as well as in section 2.3 of this dissertation.

- By reducing the thickness of the LD p-GaN cladding layer as is permitted in LD designs using tunnel junction contacts (and as previously discussed in chapter 3), the tunnel junction interface, and so the extent of the grating, is brought closer to the active region by the same amount. This increased proximity should significantly increase the coupling κ, allowing for higher-order gratings with wider periods.

In this way, the DFB and the tunnel junction both improve the implementation of the other design element, yielding greater-than-the-sum-of-the-parts benefits to the LD. This motivates further study on this design. We note that while other LDs with both TJ contacts and DFB gratings have been realized at the time of writing [9], they do not implement the design that is to be explored in depth here.

Last, it is important to note that this design necessarily requires some current spreading within p-type material, which is known to be typically a poor current-spreading material [2]. This nonuniform current injection, however, yields a periodic distribution of current density and in turn a periodic optical gain in the direction of the grating. It is possible that designing for a complex-coupled DFB grating may be one option for realizing a device that (1) retains the aforementioned benefits of the TJ-DFB combination and (2) addresses the issues with p-GaN current spreading by instead incorporating benefits of gain-coupling such as improved side-mode suppression ratio (SMSR), resolved wavelength degeneracy, and reduced spatial hole burning [108, 109, 110]. In this work, however, we set aside this issue as a subject of future work and optimization to be discussed in chapter 5 and to be researched further in the future.

4.2 Simulation and Calculation

In this work, we consider various DFB grating designs that all extend from the top of the p-type material (at the bottom of the grating) to the top of the n-type material (at the top of the grating), as pictured in Figure 4.2a. We assume the grating lengthwise covers the full length of the LD ridge, which we assume to be 1500 μm long, and widthwise covers the center 5 μm of LD ridge, which we assume to be 8 μm wide. We assume a 50% duty cycle ($\gamma = 0.5$), and per the work in chapter 3, we assume a low-loss, 50% depleted tunnel junction. We model designs with metal on top of the grating, as becomes feasible at high grating orders, as well as designs without metal on top of the grating that use n-GaN to spread the current, as shown in Figure 4.1. We seek designs with $0.7 \sim< \kappa L_g \sim< 1.5$ for a narrow stopband, and we seek designs with higher-order gratings for simpler fabrication. The principal variables are the p-GaN cladding thickness t_p, the total tunnel junction regrowth thickness t_n, the first-order grating period Λ, and grating order m. These variables are also indicated in Figure 4.2a.

We first model designs in two dimensions in the film-mode matching FIMMWAVE software [111] to calculate effective refractive indices. We then calculate the grating period Λ and the coupling κ using equations (4.1) and (4.2), respectively. Last, total

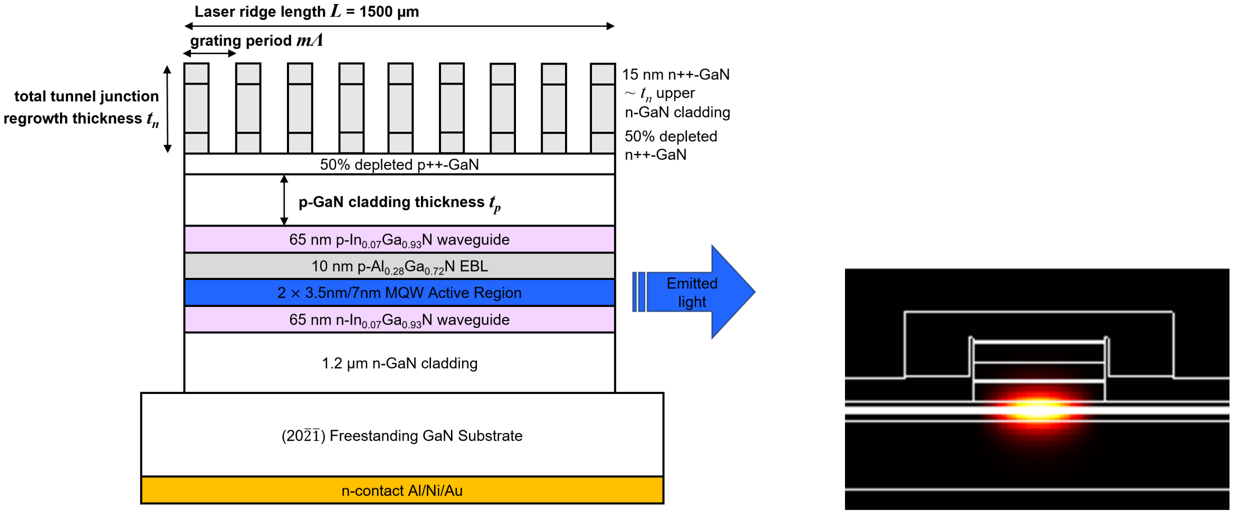

(a) (b)

Figure 4.2: (a) Cross-sectional schematic of relevant DFB grating parameters and (b) a two-dimensional color-intensity plot (arbitrary units) of a lasing mode representative of those simulated during this work.

internal absorption loss is calculated for each design (using the same transfer matrix model as was used in chapter 3) as an average weighted by the duty cycle (usually 50%) of the loss values associated with 1D models of the grating top and grating bottom cross-sections [95, 97, 96].

4.3 Results

4.3.1 First-Order Gratings

Contour plots of the calculated grating period, coupling, coupling-cavity-length product, and total internal loss, assuming a first-order grating, against TJ-DFB LD design, are provided in Figure 4.3.

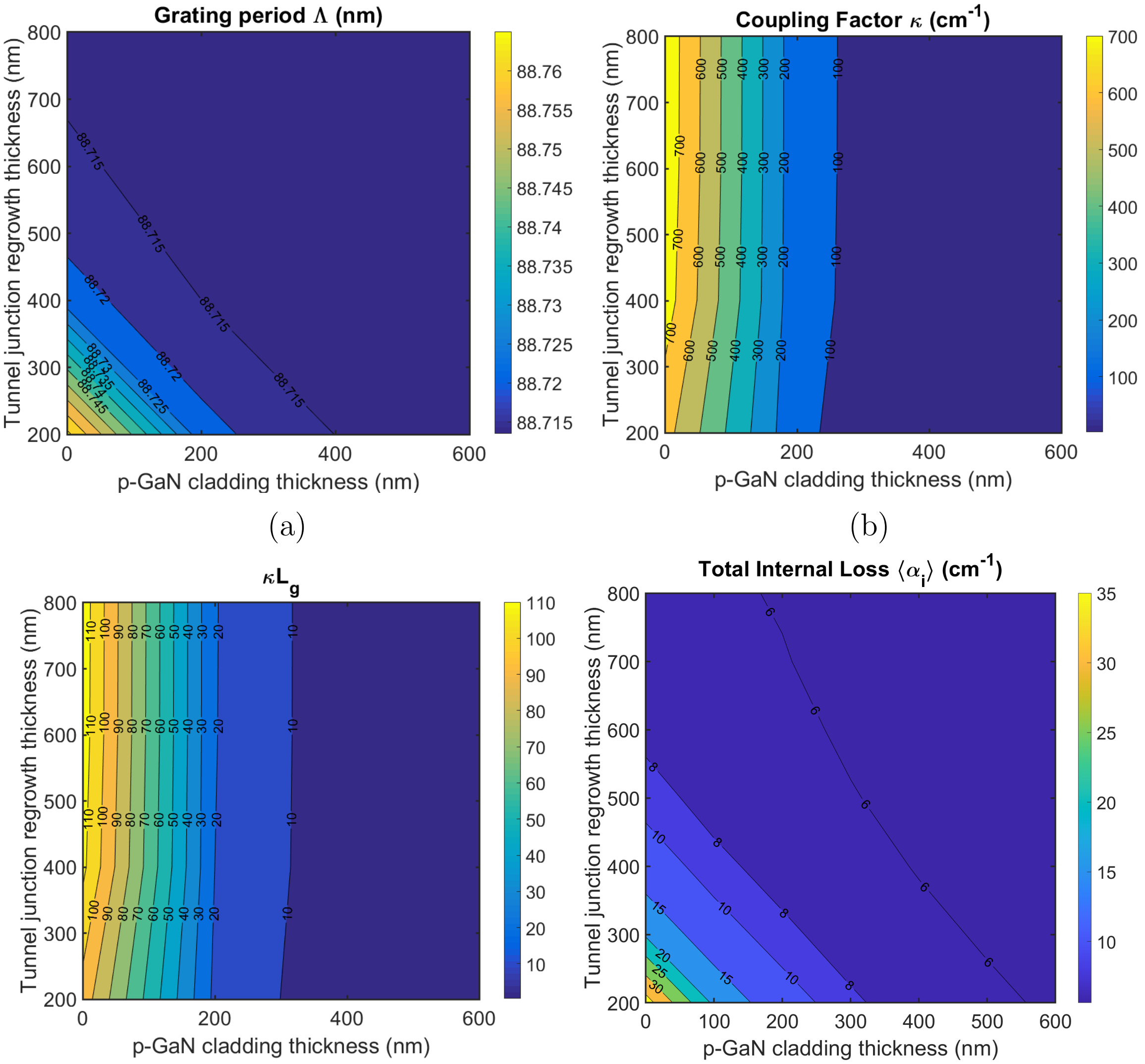

(a) (b)

(c) (d)

Figure 4.3: Contour plots of the calculated grating period Γ, coupling κ, coupling-cavity-length product κL_g, and total internal optical absorption loss α_i for a first-order grating with cross-sections defined in Figure 4.2a.

4.3.2 Higher-Order Gratings

The high coupling values modeled for a first-order grating and shown in Figure 4.3 motivate increasing the order of the grating. A plot that compares coupling, grating order, and p-GaN cladding thickness is provided in Figure 4.4a, and a simple visual aid for the linear relationship between grating period and grating order is provided in

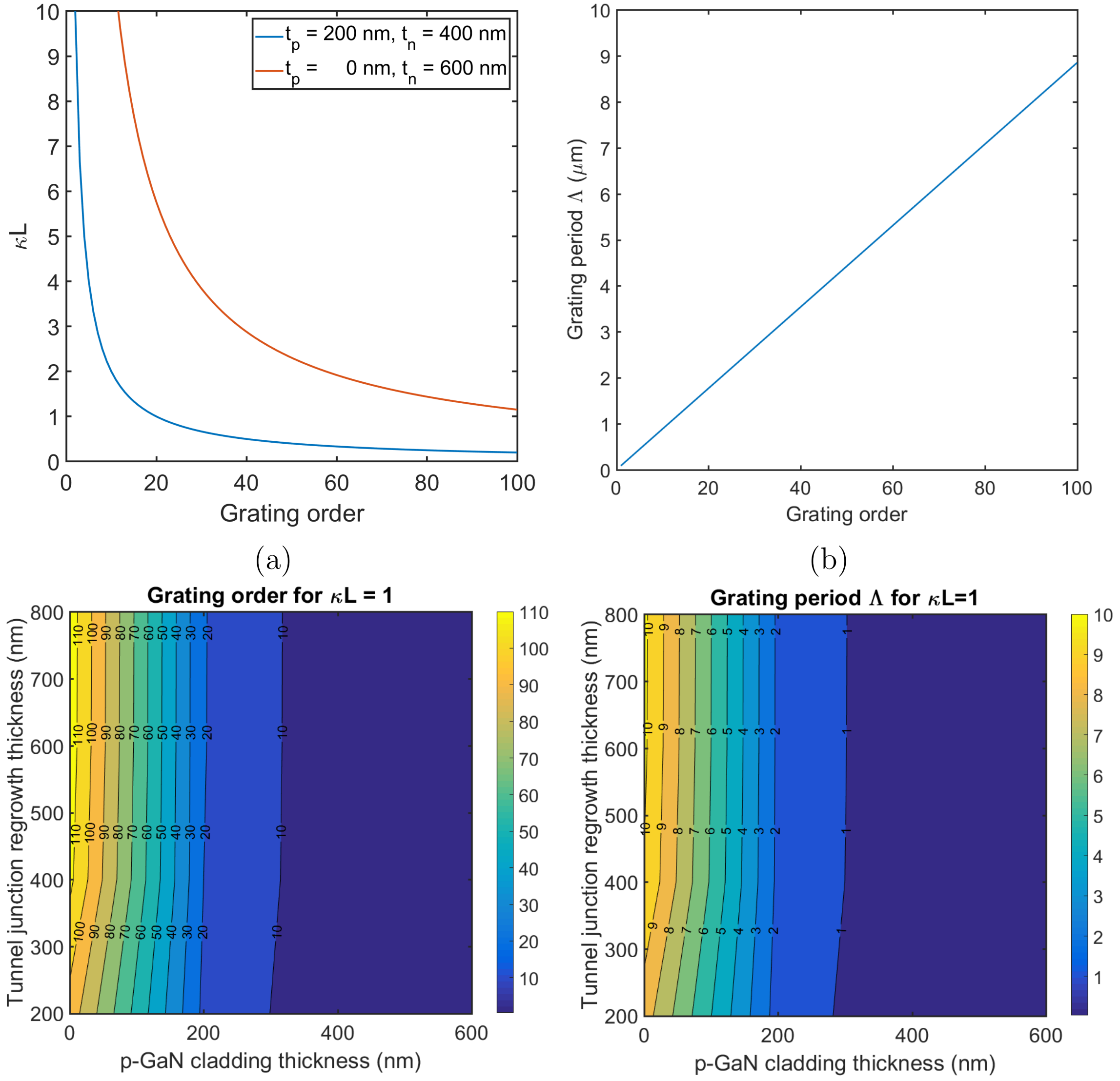

(a) (b)

(c) (d)

Figure 4.4: A set of visualizations of the coupling and grating period values accessible to the TJ-DFB design: (a) DFB order vs. coupling for two different TJ positions where grating height is held constant; (b) DFB order vs. corresponding grating period, and epitaxial design vs. (c) grating order and (d) grating period for $\kappa L_g = 1$.

Figure 4.4b. Two equivalent contour plots that give the relationship between the design parameters and the resulting values of grating period and grating order are provided in Figures 4.4c and 4.4d.

From these, we proceed to examine the following designs:

	Model 1	Model 2	Model 3	Model 4
p-GaN cladding thickness, t_p (nm)	200	0	0	0
Tunnel junction stack thickness, t_n (nm)	400	600	600	600
Grating order for $\kappa L_g = 1$, m_1	21	115	85	85
Grating period for $\kappa L_g = 1$, Γ_1 (nm)	1863	10225	7522	7522
Internal Optical Absorption Loss, α_i (cm^{-1})	6.76	7.00	7.00	6.51

Table 4.1: Design parameters for four different tunnel junction DFB grating models under the constraint $\kappa L_g = 1$.

1. $t_p = 200$ nm, $t_n = 400$ nm, and metal contacts on the tops of the grating;
2. $t_p = 0$ nm, $t_n = 600$ nm, and metal contacts on the tops of the grating;
3. $t_p = 0$ nm, $t_n = 600$ nm, and metal contacts on the tops of the grating, with effective refractive index values calculated through the transfer matrix method, as opposed to in FIMMWAVE for the previous models.
4. $t_p = 0$ nm, $t_n = 600$ nm, and no metal contacts on the tops of the grating, with effective refractive indices also calculated using the transfer matrix method.

A table of modeled and calculated parameters of interest is given in Table 4.1.

4.4 Analysis and Discussion

Figure 4.3b show that reducing the thickness of the p-GaN cladding layer, while holding constant the location of the grating bottom at the top of the p-type material, has the effect of dramatically increasing coupling, and this can be attributed to the grating being brought into close proximity with the active region. This has the effect of increasing total internal loss, per Figure 4.3d, but the model also shows that increasing the tunnel junction regrowth thickness by a similar amount may straightforwardly reduce the loss penalty without affecting coupling.

This process yields coupling values for the DFB grating as high as about $\kappa = 700$ cm^{-1}, or $\kappa L_g = 110$ for $L_g = 1500$ μm. This creates the intended overhead in coupling that allows for the use of higher grating orders. Figure 4.4a depicts modeled coupling versus grating order for two illustrative TJ DFB LD designs; notably, thinning the p-GaN cladding layer $t_p \rightarrow 0$ nm allows for up to 115th-order gratings without κL_g decreasing below unity. Figure 4.4b straightforwardly visualizes the linear relationship between order and grating period. Last, Figures 4.4c and 4.4d give the modeled grating order and period for various TJ DFB LD designs under the constraints that the DFB grating bottom is at the top of the p++-GaN layer and the coupling is fixed at $\kappa L_g = 1$. These show a strong correlation between the p-GaN cladding layer thickness and the coupling, since the p-GaN cladding layer contributes to vertical distance between the active region and the DFB grating. These also show that the coupling is nearly independent of the TJ regrowth thickness, though the dependence is somewhat stronger when the p-GaN cladding is eliminated or nearly eliminated, at which point the TJ regrowth begins to contribute to the index contrast between the grating teeth and the spaces in the grating.

Alternatively, as shown in table 4.1, moving the TJ interface and the bottom of the DFB grating 200 nm downwards by eliminating the p-GaN cladding layer allows a $\kappa L_g = 1$ grating to move from a 21st-order grating (grating period 1.863 μm) to a 115th-order grating (grating period 10.2 μm), while increasing internal optical absorption loss by 0.23 cm^{-1}, i.e. by 3.08%. Contacting the top of the grating, or omitting this contact from the design, is not shown to significantly affect coupling, as models 3 and 4 yield the same grating order and period. However, omitting top-of-grating contacts is shown to reduce internal optical absorption loss by 0.49 cm^{-1}, or by 7.00%.

4.5 Conclusions

In this work, we modeled a laser diode synthesizing the benefits of both the tunnel junction contact and the distributed feedback grating. This design was shown to yield considerable overhead in coupling which allows the DFB LD to move to higher orders and grating periods. Through the designs modeled here, gratings up to 115th-order, i.e. about 10.2 μm in period, were shown to be achievable while simultaneously maintaining $\kappa L_g = 1$.

As mentioned earlier in this chapter, current spreading remains a limitation of this design, which in its current form is likely to yield nonuniform (in the direction of the DFB grating) current injection into p-type material. We anticipate moving to a complex-coupled DFB grating design may be an effective strategy to circumvent this issue; this, and other potential solutions, will be subjects for future research.

Chapter 5

Conclusions and Future Research Directions

Much of laser diode research seeks to (1) improve power conversion efficiency and in turn improve performance of LDs, and to (2) reduce fabrication complexity and in turn reduce the cost of LD fabrication such that the LD may become a more commercially viable technology. The tunnel junction presents opportunities for both efforts, and in this dissertation, some of these opportunities were explored.

III-Nitride tunnel junctions in the literature are frequently grown by molecular beam epitaxy (MBE) [13, 16, 76, 83], which is a highly convenient growth technology for the tunnel junction because MBE growth conditions generally preserve activation of p-type material [43, 44] while ambient hydrogen in metal-organic vapor phase epitaxy (MOCVD) growth conditions has been shown to passivate p-type material [36]. However, since MOCVD as a growth technology is already widely used by industry and provides greater scalability, MOCVD-grown tunnel junctions are both attractive and necessary for commercialization of tunnel junction devices. Work is ongoing to demonstrate and refine fully MOCVD-grown tunnel junction devices that also address activation of p-type material

[5, 45, 46, 47, 48]. This dissertation advanced these efforts: in chapter 2, we demonstrated III-Nitride edge-emitting LDs with MBE-grown tunnel junctions that showed reduced threshold currents relative to an ITO-contact devices that were processed in tandem. We additionally demonstrated an edge-emitting LD with an MOCVD-grown tunnel junction utilizing lateral activation through the LD ridge sidewalls to produce electrically active p-type material.

Additionally, by providing an interface between p-type and n-type material, the tunnel junction facilitates reduction of p-type material, which in III-Nitride devices is typically relatively optically lossy [3, 31]. However, the resulting increased proximity of the highly-doped tunnel junction to the active region also brings increased internal optical absorption loss, creating an optimization problem. This dissertation explored in depth the effect of the reduction of p-type material, in conjunction with optimization of the tunnel junction doping profile, on internal optical absorption loss using transfer matrix modeling, and identified several possible low-loss designs.

Last, combined tunnel junction-distribute feedback grating (TJ-DFB) LDs were modeled, motivated by the potential for emergent benefits from a combined design that locates the bottom of the grating at the tunnel junction regrowth interface, which itself is located at the top of the p-type material. In such a design, the DFB grating provides an activation mechanism for the tunnel junction where hydrogen may diffuse out of p-type material through the grating teeth. At the same time, the tunnel junction permits designs with reduced p-GaN, providing higher coupling levels and so enabling higher-order gratings that may be fabricated through processes less expensive than electron beam lithography. Film mode matching models and additional transfer matrix and analytical modeling were used to evaluate the coupling and feasibility of various combined TJ-DFB grating models.

Additional research is still needed to fully realize the potential of tunnel junction contact implementations on edge-emitting and distributed feedback LDs. Some of this future work is discussed below.

5.1 Optimization of the Tunnel Junction Contact

In chapter 2, several sites of related future work were identified. Primary among these was optimization of the doping profile of the tunnel junction, where the turn-on and turn-off slopes of [Mg] and [Si] in the p++ and n++-doped layers may not necessarily be sufficiently steep for efficient operation. Within the tunnel junction, excess compensation can occur if the [Mg] and [Si] profiles significantly overlap, yielding a wider tunneling distance and increased excess voltage. At the edges of the tunnel junction, undepleted Mg and Si can contribute to excess internal optical absorption loss, precluding any of the optimizations discussed in chapter 3 or chapter 4 that frequently involve bringing the tunnel junction in closer proximity to the active region. While some aspects of the doping profiles in the MOCVD-grown TJ were well-controlled, others indicated room for optimization that may yield reductions in excess voltage and internal optical absorption loss. This is a site of ongoing work. For example, low-temperature flow-modulation epitaxy has been recently shown to yield more abrupt Mg doping profiles at a regrowth interface [50, 51]. Low-temperature flow modulation epitaxy also has the potential to address degradation of the InGaN quantum wells during high-temperature tunnel junction regrowths.

Work may also be conducted on incorporation of Indium into the tunnel junction. This is an optimization problem, where InGaN tunnel junctions are likely to yield both reduced excess voltage and increased optical absorption loss due to their smaller bandgap. Growth of InGaN tunnel junctions also presents sensitive materials and reproducibility problems to be investigated, as InGaN layers have been shown to experience temperature-dependent segregation at MOCVD crystal growth temperatures [112, 113]. This is also a subject of ongoing work [9, 47, 79, 80, 81, 114], and future work will continue to address the optimization of the InGaN tunnel junction for edge-emitting and distributed feedback laser diode processes and current densities.

Last, it has been shown that excess voltage in sidewall-activated tunnel junction devices may indicate incomplete activation of p-type material, leading to a larger tunnel junction depletion width, where devices with larger feature size showed higher operating voltage at a given current density [7]. It has also been proposed that some dry etch processes, which are frequently used to form LD ridges, can compensate exposed p-type material [65, 66]; since n-type layers present a barrier to diffusion of hydrogen [42], this risks diminishing of lateral diffusion out of a laser ridge formed by a dry etch process. This has motivated studies into wet etch treatments that reduce this effect [48]. Further work may be conducted on activation conditions and surface treatments to maximize lateral diffusion of hydrogen out of LD ridges and gratings, as well as on activation schemes more generally such as *in situ* activation [39].

5.2 Moving to P-Minimal Laser Diode Designs

In chapter 3, p-minimal LDs were modeled showing significant feasible reductions in p-type material and/or internal optical absorption loss. However, the lowest-loss models assume an optimized TJ in which the [Si] and [Mg] rise and fall rates associated with the n++ and p++ layers are maximized. and in which the n++ and p++ layers are grown at the minimum thickness required to fully drop the built-in potential of the PN junction. This emphasizes the importance of the previously discussed work on optimizing the doping profiles of the TJ to fully realize the benefit of the TJ contact: only once an optimized TJ is realized may p-minimal LDs be fabricated with minimal risk of significant increases in internal optical absorption losses.

Last, as discussed in chapter 3, two-dimensional modeling and calculations may also be conducted to examine the predicted electrical and optical profiles of p-minimal designs in full. Two-dimensional modeling is also likely to be of help to the TJ-DFB LD, where two-dimensional profiles of current spreading and optical absorption losses would be particular areas of interest in addition to the existing two-dimensional models of the lasing mode profile.

5.3 Fully Realizing the Tunnel Junction-Distributed Feedback Grating LD

While chapter 4 provided a motivation for LDs using the TJ-DFB combination, such LDs are yet to be realized; one site of future work would then be developing growth and fabrication processes to ultimately realize this device. For example, the DFB grating would most likely be realized by a selective area growth process to avoid damage to exposed p-GaN associated with dry etching [65, 66], or otherwise an appropriate chemical treatment would need to be developed to recover etch damage to exposed material during an etched-grating process, where similar goals have been achieved for micro-LED sidewalls [48].

The TJ-DFB design also leaves as a site for future research the issue of current spreading such that the LD active region is uniformly pumped, and an additional site of future research may be into solutions, primarily improved conductivity in p-type material, such that the benefits of the TJ-DFB design may still be realized. Alternatively, since the profile of the pumped areas of the active region would have the same periodicity as the DFB grating, the goal of uniform current spreading may be eschewed entirely for a complex-coupled TJ-DFB LD design that may potentially pick up additional benefits associated with gain-coupling such as improved side-mode suppression ratio, resolved wavelength degeneracy, and reduced spatial hole burning [108, 109, 110].

Appendix A

Fabrication Process for Sidewall-Activated Tunnel Junction Laser Diode

For more information on this fabrication process, see section 2.3 and Refs. [26, 41, 63, 115, 116].

Step	Equipment	#	Process Step	Notes
A. Ridge Formation and Sidewall Activation				
Ridges Litho	Solvent Bench	1	3' Ace, 3' Iso, 2' DI (sonicate on high) N2 dry	
	PR Bench	2	Dehydration bake on hotplate at ≥110 °C for ≥2', cool 1'	
		3	Spin **LOL 2000**, 2 krpm, 10 krpm/s, 30s (~250 nm thick)	mount small samples on blue tape, can spin multiple samples simultaneously
		4	Clean backside with EBR 100	if needed
		5	Bake on center of LH hotplate at **210 °C for 5'**, cool 1'	Actual center T ~194 °C
		6	Spin **955CM-1.8**, 3 krpm, 10 krpm/s, 30 s (~1.8 µm thick)	
		7	Clean backside with EBR 100	if needed
		8	Soft bake on hotplate **95 °C for 90 s**	
	Stepper #2 (30+')	9	Load Ridges mask (TOPNV2)	
		10	Load sample onto 2" 500 µm chuck with 130 µm shim with *c* + pointing up	
		11	"EDIT TOPNV2" Check: die size and column number	
		12	"EXEC TOPNV2", PASS: "RIDGES"	no pass shift
		13	**Expose 0.75 s**, focus = -1	
	PR Bench	14	Post-exposure bake on hotplate at **110 °C for 90 s**	
	Develop Bench	15	Develop in **726MIF for 65 s**, DI Rinse, N2 dry	
	Microscope	16	Inspect (0.3-0.5 um undercut on LOL 2000) develop more if necessary	
	UV Ozone	17	1200 s (~6 Å/min)	
Ridges Etch	RIE #5 (2+hr)	18	Load bare carrier wafer	
		19	Run BECE_00 O2 clean: 10', 50 sccm, 50 mTorr, 300 W RF; BCl3/Cl2 pretreat: 3', 20 sccm BCl3, 5 sccm Cl2, 10 mTorr, 15 W RF; Cl2 etch conditions: 2', 10 sccm, 5 mTorr, 200 W RF	no He cooling
		20	Load sample onto carrier wafer (no mounting oil)	
		21	Run BECE_01 BCl3 pretreat: 2', 10 sccm, 10 mTorr, 100 W RF; Cl2 Etch: Time TBD, 10 sccm, 5 mTorr, 200 W RF	no He cooling
	Solvent Bench	22	Soak sample in DI water, N2 dry	
	Solvent Bench	23	Soak sample in 1165 pre-heated to 80 °C for 15'	place sample face-down in beaker
		24	Move sample to 2nd 1165 pre-heated to 80 °C	
		25	Sonicate in bath at frequency: 8, intensity: 8, power: low, time~20-30 s	
		26	swish for 30'' Iso, 30'' DI, N2 dry	
		27	Inspect, repeat steps 34-37 if necessary	
	Microscope	28	Inspect	
Reactivate	RTA	29	Reactivate 15' N2/O2 at 600 °C	
SiO2 Blanket Deposition	IBD (3+ hr, start at same time as reactivation)	30	Load silicon calibration piece	
		31	Login: Earl Check and run recipe: COH_Ratetestdep for 2100'' (35')	
	Ellipsometer	32	Measure SiO2 on Si calibration thickness and index	should be ~ 125 nm (dark blue colored), n=1.47
		33	Load sample(s) and THREE silicon monitors	

	IBD	34	Calculate dep time for 225 nm SiO2. Update and run recipe: COH_SiO2 Sidewall Dep	
	Ellipsometer	35	Measure SiO2 on Si monitors (thickness and index)	should be ~ 225 nm (gold colored), n=1.47
B. Insulator Via Formation and P-Contact Formation				
Insulator Via and p-Contact Litho	Solvent Bench	36	2' in each ACE/ISO/DI swishing or sonicating on lowest settings	
	PR Bench	37	Dehydration bake on hotplate ≥110 °C ≥2', cool 1'	
		38	Spin **HMDS**, 3 krpm, 10 krpm/s, 30 s (let HMDS sit for 20 s before spinning)	
		39	Spin **OCG825**, 3 krpm, 10 krpm/s, 30 s (~1.5 μm thick)	
		40	Clean backside of sample with EBR 100	
		41	Bake on hotplate at **95 °C for 2'**	
	MJB-3 Aligner	42	Load sample onto one of the black chucks	left aligner only
		43	Flood expose 1 s	
		44	Let sample outgas for 5' (VERY IMPORTANT)	
	PR Bench	45	Bake on hotplate at **95 °C for 2'** let cool 1'	
		46	Spin **955CM-1.8**, 3 krpm, 10 krpm/s, 30 s (~1.8 μm thick)	
		47	Clean backside with EBR 100	if needed
		48	Softbake on hotplate at **95 °C for 90 s**	
	Stepper #2 (30+')	49	Load mask #2 - "EF V5.gds-Layer 7: PContPads"	
		50	Load sample onto 2" 500 μm chuck with 130 μm shim with *c* + pointing up	
		51	"EDIT TOPNV2" Check: die size, column number, right alignment die position	
		52	"EXEC RTOPNV2", PASS: "PCONTS"	no pass shift
		53	Expose **0.75 s**, focus= -1	
	Develop Bench	54	Develop in **726MIF for 55-60s** (~2 μm undercut on OCG825), DI Rinse, N2 dry	
	Microscope	55	Inspect, develop more if necessary	
	UV Ozone	56	1200 s (~6 Å/min)	
SiO2 Wet Etch1	Acid Bench	57	Etch piece of Si Monitor #1 in BHF (~200 nm/min)	
		58	Inspect monitor for hydrophobicity every 10-15s, record total etch time (should take 50 s – 1')	
		59	Etch sample in BHF for 1.1x the monitor etch time, DI rinse, N2 dry	
p-Contact Dep	Acid Bench	36	30s HCl dip, DI rinse, N2 dry	
	E-Beam #3 (2+ hr)	37	Deposit 10 kÅ Al	Yonkee et al., Semicond. Sci. Technol. 33(1), 015015 (2018).
	Solvent Bench	38	Place upside-down in 1165 heated to 80 °C for 10+', then liftoff using pipette agitation	do not leave overnight in hot 1165
		39	Move sample to fresh beaker of 1165 and agitate until visibly clean pattern (no Au strands)	
		40	swish for 30'' Iso, 30'' DI, N2 dry	
	Microscope	41	Inspect, repeat steps 91-93 if necessary	
C. P-Pad Formation				
	Solvent clean	42	2' in each ACE/ISO/DI swishing	
	PR Bench	43	Dehydration bake on hotplate ≥110 °C ≥2', cool 1'	
		44	Spin **HMDS**, 3 krpm, 10 krpm/s, 30 s (let HMDS sit for 20 s before spinning)	
		45	Spin **OCG825**, 3 krpm, 10 krpm/s, 30 s (~1.5 μm thick)	

Contact Pads Litho		46	Clean backside of sample with EBR 100	
		47	Bake on hotplate at **95 °C for 2'**	
	MJB-3 aligner	48	Load sample onto one of the black chucks	
		49	Flood expose 1 s	
		50	Let sample outgas for 5' (VERY IMPORTANT)	
	PR Bench	51	Bake on hotplate at **95 °C for 2'** let cool 1'	
		52	Spin **955CM-1.8**, 3 krpm, 10 krpm/s, 30 s (~1.8 µm thick)	
		53	Clean backside with EBR 100	if needed
		54	Softbake on hotplate at **95 °C for 90 s**	
		55	Load mask #3 - TOPNV2 PADS	
		56	Load sample onto 2" 500 µm chuck with 180 µm shim	
	Stepper #2	57	"EDIT TOPNV2" Check: die size, column number, right alignment die position	
	(30+')	58	"EXEC TOPNV2", PASS: "PCONTS"	no pass shift
		59	Expose 0.4 s, focus= +2	
	Develop bench	60	Develop in **726MIF for 55-60s** (~2 µm undercut on OCG825), DI Rinse, N2 dry	
	Microscope	61	Inspect, develop more if necessary	
	UV Ozone	62	1200 s (~6 Å/min)	
p-Pad Dep	E-Beam #3 (2+ hr)	63	Deposit 150/10,000 Å Ti/Au	more gold could be better, 1 um is ebeam 3 limit
	Solvent bench	64	Place upside-down in NMP heated to 80 °C for 10'	
		65	Liftoff using pipette agitation	
		66	swish for 1' Iso, 1' DI, N2 dry	
	Microscope	67	Inspect, repeat steps 91-93 if necessary	
D. C+ Facet Formation				
C+ Facets Litho	Solvent Bench	68	2' in each ACE/ISO/DI swishing	
	PR Bench	69	Dehydration bake on hotplate at ≥110 °C for ≥2', cool 1'	
		70	Spin **HMDS**, 3.5 krpm, 10 krpm/s, 45 s	
		71	Spin **SPR220-7.0**, 3.5 krpm, 10 krpm/s, 45 s (~6 µm thick)	
		72	Clean backside with EBR 100	if needed
		73	Soft bake on hotplate **115 °C for 120 s**	
	Stepper #2 (30+')	74	Load CAIBE mask	
		75	Load sample onto 2" 500 µm chuck with 130 µm shim with ***c* + pointing up**	orientation very important!
		76	"EDIT TOPNV2" Check: die size, column number, right alignment die position	
		77	Under CAIBE pass, Y Pass Shift = +0.016 (first etch, shifts pattern DOWN and exposes the c+)	Adjust pass shift if p-pad alignment was off by more than 400 nm in Y. Must align to metal in Y
		78	"EXEC TOPNV2", Pass: "CAIBE"	

		79	Expose 1.35 s, focus= -1	
	PR Bench	80	Let sample **outgas for 35'** IMPORTANT	preheat the hotplate at 50 °C
	PR Bench	81	Post-exposure bake on hotplate at **50 °C for 60 s**, then immediately move to **115 °C for 90 s**	
	Develop Bench	82	Develop in **726MIF for 105 s**, DI rinse, N2 dry	
	Microscope	83	Inspect lithography. Check that facets mask aligned in y does not expose any metal. Check that it is the C+ side that is exposed for etching first	
	UV Ozone	84	1200 s (~6 Å/min)	
SiO2 Wet Etch2	Acid Bench	85	Etch piece of Si Monitor #1 in BHF (~200 nm/min)	
		86	Inspect monitor for hydrophobicity every 10-15s, record total etch time (should take 50 s – 1')	
		87	Etch sample in BHF for double the monitor etch time, DI rinse, N2 dry	
C+ Facets Etch	Oxford Ion Mill (3+ hr)	88	Mount samples on chuck with Cu tape such that facets to be etched (c+ side) face LHS	when chuck is mounted into system, it rotates 180°, so the facets will then face the beam
		89	Check every parameter in recipe	
		90	Run: "Speck-Std_Ar_Cl2_norotate_10x" (-33 degrees) 75', 10x3' etch steps with 9x5' cool steps	etch rate 50-60 nm/min
		91	Gases: Ar 5 sccm to Neutralizer; Ar 10 sccm to Beam; Cl2 20 sccm to Chamber; Beam etch source 200 mA Neutralizer, 200 W RF, 150 mA, 250 Vb, 500 Va; Platen drive "Posn", Platen "Cool" 10 C chiller, Chamber "heat" 40 C	cools substrate and heats chamber walls
	Solvent bench	92	Strip mask in 1165 heated to 80 °C for 10+', agitate with pipette	place sample upside-down in beaker
		93	Move sample to fresh beaker of 1165	
		94	Soak sample in 1165 heated to 80 °C for 2', agitate with pipette	
		95	swish for 30'' Iso, 30'' DI, N2 dry	
	Microscope	96	Inspect that the surface is clean and that the correct side has been etched	
	Laser Microscope	97	Confirm the etch depth and profile	
E. C- Facet Formation				
C- Facets Litho	Solvent Bench	98	1' Ace, 1' Iso, 1' DI, N2 dry	
	PR Bench	99	Dehydration bake on hotplate at ≥110 °C for ≥2', cool 1'	
		100	Spin **HMDS**, 3.5 krpm, 10 krpm/s, 45 s	
		101	Spin **SPR220-7.0**, 3.5 krpm, 10 krpm/s, 45 s (~6 µm thick)	
		102	Clean backside with EBR 100	if needed
		103	Soft bake on hotplate **115 °C for 120 s**	
	Stepper #2 (30+')	104	Load CAIBE mask	
		105	Load sample onto 2" 500 µm chuck with 130 µm shim with ***c* + pointing up**	orientation very important!
		106	"EDIT TOPNV2" Check: die size, column number, right alignment die position	
		107	Under CAIBE pass, Y Pass Shift = -0.016 (2nd etch, shifts pattern DOWN and exposes the c-)	Adjust pass shift if p-pad alignment was off by more than 400 nm in Y. Must align to metal in Y
		108	"EXEC TOPNV2", Pass: "CAIBE"	

		109	Expose 1.35 s, focus= -1	
	PR Bench	110	Let sample **outgas for 35'** IMPORTANT	preheat the hotplate at 50 °C
	PR Bench	111	Post-exposure bake at **50 °C for 60 s**, then immediately move to **115 °C for 90 s**	
	Develop Bench	112	Develop in **726MIF for 105 s**, DI rinse, N2 dry	
	Microscope	113	Inspect lithography. Check that facets mask aligned in y does not expose any metal. Check that it is the c- side that is exposed for etching	
	UV Ozone	114	1200 s (~6 Å/min)	
SiO2 Wet Etch3	Acid Bench	115	Etch piece of Si Monitor #2 in BHF (~200 nm/min)	
		116	Inspect monitor for hydrophobicity every 10-15s, record total etch time (should take 50 s – 1')	
		117	Etch sample in BHF for double the monitor etch time, DI rinse, N2 dry	
C- Facets Etch	Oxford Ion Mill (3+ hr)	118	Mount samples on chuck with Cu tape such that facets to be etched (c- side) face LHS	(when chuck is mounted into system, it rotates 180°, so the facets will then face the beam)
		119	Check every parameter in recipe	
		120	Run: "Speck-Std_Ar_Cl2_norotate_10x" (-33 degrees) 75', 10x3' etch steps with 9x5' cool steps	etch rate 50-60 nm/min
	Solvent Bench	121	Strip mask in 1165 heated to 80 °C for 10+', agitate with pipette	place sample upside-down in beaker
		122	Move sample to fresh beaker of 1165	
		123	Soak sample in 1165 heated to 80 °C for 2', agitate with pipette	
		124	swish for 30'' Iso, 30'' DI, N2 dry	
	Microscope	125	Inspect that the surface is clean and that the correct side has been etched	
	Laser Microscope	126	Confirm the etch depth and profile	
F1. N-Contact Formation (No thinning)				
N-contact Dep & Liftoff	PR Bench	127	Mount sample upside down on Si wafer with a drop of AZ 4110	
		128	Bake on hotplate at 105 °C for >5'	
	RIE #5 (40' + 40' per sample)	129	Yonkee01 on bare carrier wafer	
		130	Yonkee02 10'	
		131	Place samples in water immediately after removing from RIE 5	
	Acid Bench	132	60s BHF dip, DI rinse, N2 dry	
	UV Ozone	133	20' (1200")	
	Acid Bench	134	30s HCl dip, DI rinse, N2 dry	
	E-beam #3 (1+ hr)	135	Deposit 10 kÅ Al	
	Solvent Bench	136	Soak sample in NMP heated to 80 °C until sample detaches	Place upside-down in beaker. Do not try to slide or pry samples off
		137	2' Iso, 2' DI, N2 dry	
	Microscope	138	Inspect, repeat NMP if necessary	
Laser Testing	Laser Test Setup	139	Preliminary testing	Consider annealing after
F2. Substrate Thinning and N-Contact Formation After Thinning				
Substrate Thinning	Packaging Lab	140	Remove backside contact with tape	
		141	Mount sample upside down on sapphire wafer with tan wax	
		142	Bake on hotplate at 120 °C	

		143	Polish samples (one at a time)	
N-contact Dep & Liftoff	Acid Bench	144	60s concentrated HF, DI rinse, N2 dry	
	Solvent Bench	145	Solvent clean	
	RIE #5 (40' + 40' per sample)	146	Yonkee01 on bare carrier wafer	
		147	Yonkee02 10'	
		148	Place samples in water immediately after removing from RIE 5	
	Acid Bench	149	60s BHF dip, DI rinse, N2 dry	
	UV Ozone	150	20' (1200")	
	Acid Bench	151	30s HCl dip, DI rinse, N2 dry	
	E-beam #3 (1+ hr)	152	Deposit 10 kÅ Al	
	Solvent Bench	153	Soak sample in NMP heated to 80 °C until sample detaches from sapphire	Place upside-down in beaker. Do not try to slide or pry samples off
		154	2' Iso, 2' DI, N2 dry	
	Microscope	155	Inspect, repeat NMP if necessary	
Heat Sink Mounting	Packaging Lab	156	Solder to Cu heatsink	
Laser Testing	Laser Test Setup	157	Laser testing	

Bibliography

[1] S. Nakamura, T. Mukai, and M. Senoh, “High-power GaN P-N junction blue-light-emitting diodes.” Japanese Journal of Applied Physics **30** (1991), no. Part 2, No. 12A L1998–L2001.

[2] U. Kaufmann, P. Schlotter, H. Obloh, K. Köhler, and M. Maier, “Hole conductivity and compensation in epitaxial GaN:Mg layers.” Phys. Rev. B **62** (2000) 10867–10872.

[3] C.-Y. Huang, Y.-D. Lin, A. Tyagi, A. Chakraborty, H. Ohta, J. S. Speck, S. P. DenBaars, and S. Nakamura, “Optical waveguide simulations for the optimization of InGaN-based green laser diodes.” Journal of Applied Physics **107** (2010), no. 2 023101.

[4] L. Esaki, “New phenomenon in narrow germanium p-n junctions.” Phys. Rev. **109** (1958) 603–604.

[5] Y. Kuwano, M. Kaga, T. Morita, K. Yamashita, K. Yagi, M. Iwaya, T. Takeuchi, S. Kamiyama, and I. Akasaki, “Lateral hydrogen diffusion at p-GaN layers in nitride-based light emitting diodes with tunnel junctions.” Japanese Journal of Applied Physics **52** (2013).

[6] B. P. Yonkee, E. C. Young, S. P. DenBaars, S. Nakamura, and J. S. Speck, “Silver free III-nitride flip chip light-emitting-diode with wall plug efficiency over 70% utilizing a GaN tunnel junction.” Applied Physics Letters **109** (2016), no. 19 191104.

[7] D. Hwang, A. J. Mughal, M. S. Wong, A. I. Alhassan, S. Nakamura, and S. P. DenBaars, “Micro-light-emitting diodes with III–nitride tunnel junction contacts grown by metalorganic chemical vapor deposition.” Applied Physics Express **11** (2017), no. 1 012102.

[8] K. Gibasiewicz, A. Bojarska-Cieślińska, G. Muzioł, C. Skierbiszewski, S. Grzanka, A. Kafar, P. Perlin, S. Najda, and T. Suski, “InGaN blue light emitting micro-diodes with current path defined by tunnel junction.” Opt. Lett. **45** (2020), no. 15 4332–4335.

[9] G. Muziol, M. Hajdel, H. Turski, K. Nomoto, M. Siekacz, K. Nowakowski-Szkudlarek, M. Żak, D. Jena, H. G. Xing, P. Perlin, and C. Skierbiszewski, "Distributed-feedback blue laser diode utilizing a tunnel junction grown by plasma-assisted molecular beam epitaxy." Opt. Express **28** (2020), no. 23 35321–35329.

[10] S. Lee, C. A. Forman, J. Kearns, J. T. Leonard, D. A. Cohen, S. Nakamura, and S. P. DenBaars, "Demonstration of GaN-based vertical-cavity surface-emitting lasers with buried tunnel junction contacts." Opt. Express **27** (2019), no. 22 31621–31628.

[11] J. T. Leonard, E. C. Young, B. P. Yonkee, D. A. Cohen, T. Margalith, S. P. DenBaars, J. S. Speck, and S. Nakamura, "Demonstration of a III-nitride vertical-cavity surface-emitting laser with a III-nitride tunnel junction intracavity contact." Applied Physics Letters **107** (2015), no. 9 091105.

[12] B. P. Yonkee, E. C. Young, C. Lee, J. T. Leonard, S. P. DenBaars, J. S. Speck, and S. Nakamura, "Demonstration of a III-nitride edge-emitting laser diode utilizing a GaN tunnel junction contact." Opt. Express **24** (2016), no. 7 7816–7822.

[13] C. Skierbiszewski, G. Muziol, K. Nowakowski-Szkudlarek, H. Turski, M. Siekacz, A. Feduniewicz-Zmuda, A. Nowakowska-Szkudlarek, M. Sawicka, and P. Perlin, "True-blue laser diodes with tunnel junctions grown monolithically by plasma-assisted molecular beam epitaxy." Applied Physics Express **11** (2018), no. 3 034103.

[14] S. W. Hamdy, E. C. Young, A. I. Alhassan, D. L. Becerra, S. P. DenBaars, J. S. Speck, and S. Nakamura, "Efficient tunnel junction contacts for high-power semipolar III-nitride edge-emitting laser diodes." Opt. Express **27** (2019), no. 6 8327–8334.

[15] M. Siekacz, G. Muziol, M. Hajdel, M. Żak, K. Nowakowski-Szkudlarek, H. Turski, M. Sawicka, P. Wolny, A. Feduniewicz-Żmuda, S. Stanczyk, J. Moneta, and C. Skierbiszewski, "Stack of two III-nitride laser diodes interconnected by a tunnel junction." Opt. Express **27** (2019), no. 4 5784–5791.

[16] M. Malinverni, C. Tardy, M. Rossetti, A. Castiglia, M. Duelk, C. Vélez, D. Martin, and N. Grandjean, "InGaN laser diode with metal-free laser ridge using n+-GaN contact layers." Applied Physics Express **9** (2016), no. 6 061004.

[17] S. Bharadwaj, J. Miller, K. Lee, J. Lederman, M. Siekacz, H. G. Xing, D. Jena, C. Skierbiszewski, and H. Turski, "Enhanced injection efficiency and light output in bottom tunnel-junction light-emitting diodes." Opt. Express **28** (2020), no. 4 4489–4500.

[18] J. Iveland, L. Martinelli, J. Peretti, J. S. Speck, and C. Weisbuch, "Direct measurement of auger electrons emitted from a semiconductor light-emitting diode under electrical injection: Identification of the dominant mechanism for efficiency droop." Phys. Rev. Lett. **110** (2013) 177406.

[19] S. Nakamura, M. Senoh, S. ichi Nagahama, N. Iwasa, T. Yamada, T. Matsushita, H. Kiyoku, and Y. Sugimoto, "InGaN-based multi-quantum-well-structure laser diodes." Japanese Journal of Applied Physics **35** (1996), no. Part 2, No. 1B L74–L76.

[20] J. J. Wierer Jr., J. Y. Tsao, and D. S. Sizov, "Comparison between blue lasers and light-emitting diodes for future solid-state lighting." Laser & Photonics Reviews **7** (2013), no. 6 963–993.

[21] L. Y. Kuritzky and J. S. Speck, "Lighting for the 21st century with laser diodes based on non-basal plane orientations of GaN." MRS Communications **5** (2015) 463–473.

[22] C. Lee, C. Zhang, M. Cantore, R. M. Farrell, S. H. Oh, T. Margalith, J. S. Speck, S. Nakamura, J. E. Bowers, and S. P. DenBaars, "4 Gbps direct modulation of 450 nm GaN laser for high-speed visible light communication." Opt. Express **23** (2015), no. 12 16232–16237.

[23] L. Coldren, S. Corzine, and M. Mashanovitch, Diode Lasers and Photonic Integrated Circuits. Wiley Series in Microwave and Optical Engineering. Wiley, 2012.

[24] D. L. Becerra, D. A. Cohen, R. M. Farrell, S. P. DenBaars, and S. Nakamura, "Effects of active region design on gain and carrier injection and transport of CW (20-2-1) semipolar InGaN laser diodes." Applied Physics Express **9** (2016), no. 9 092104.

[25] A. I. Alhassan, R. M. Farrell, B. Saifaddin, A. Mughal, F. Wu, S. P. DenBaars, S. Nakamura, and J. S. Speck, "High luminous efficacy green light-emitting diodes with AlGaN cap layer." Opt. Express **24** (2016), no. 16 17868–17873.

[26] L. Y. Kuritzky, D. L. Becerra, A. S. Abbas, J. Nedy, S. Nakamura, S. P. DenBaars, and D. A. Cohen, "Chemically assisted ion beam etching of laser diode facets on nonpolar and semipolar orientations of GaN." Semiconductor Science and Technology **31** (2016), no. 7 075008.

[27] A. Myzaferi, A. H. Reading, D. A. Cohen, R. M. Farrell, S. Nakamura, J. S. Speck, and S. P. DenBaars, "Transparent conducting oxide clad limited area epitaxy semipolar III-nitride laser diodes." Applied Physics Letters **109** (2016), no. 6 061109.

[28] S. Masui, Y. Nakatsu, D. Kasahara, and S. Nagahama, "Recent improvement in nitride lasers." Proc. SPIE 10104, Gallium Nitride Materials and Devices XII, 101041H (2017).

[29] M. Murayama, Y. Nakayama, K. Yamazaki, Y. Hoshina, H. Watanabe, N. Fuutagawa, H. Kawanishi, T. Uemura, and H. Narui, "Watt-class green (530 nm) and blue (465 nm) laser diodes." Phys. Status Solidi A **215** (2018), no. 10 1700513.

[30] I. P. Smorchkova, E. Haus, B. Heying, P. Kozodoy, P. Fini, J. P. Ibbetson, S. Keller, S. P. DenBaars, J. S. Speck, and U. K. Mishra, "Mg doping of GaN layers grown by plasma-assisted molecular-beam epitaxy." Applied Physics Letters **76** (2000), no. 6 718–720.

[31] E. Kioupakis, P. Rinke, and C. Van de Walle, "Determination of internal loss in nitride lasers from first principles." Applied Physics Express **3** (2010) 082101.

[32] E. Kioupakis, P. Rinke, A. Schleife, F. Bechstedt, and C. G. Van de Walle, "Free-carrier absorption in nitrides from first principles." Phys. Rev. B **81** (2010) 241201.

[33] R. Singh, K. Rajkanan, D. E. Brodie, and J. H. Morgan, "Optimization of oxide-semiconductor/base-semiconductor solar cells." IEEE Transactions on Electron Devices **27** (1980), no. 4 656–662.

[34] H. Amano, M. Kito, K. Hiramatsu, and I. Akasaki, "P-type conduction in Mg-doped GaN treated with low-energy electron beam irradiation (LEEBI)." Japanese Journal of Applied Physics **28** (1989), no. Part 2, No. 12 L2112–L2114.

[35] S. Nakamura, T. Mukai, M. Senoh, and N. Iwasa, "Thermal annealing effects on p-type Mg-doped GaN films." Japanese Journal of Applied Physics **31** (1992), no. Part 2, No. 2B L139–L142.

[36] S. Nakamura, N. Iwasa, M. Senoh, and T. Mukai, "Hole compensation mechanism of p-type GaN films." Japanese Journal of Applied Physics **31** (1992), no. Part 1, No. 5A 1258–1266.

[37] S. Neugebauer, M. P. Hoffmann, H. Witte, J. Bläsing, A. Dadgar, A. Strittmatter, T. Niermann, M. Narodovitch, and M. Lehmann, "All metalorganic chemical vapor phase epitaxy of p/n-GaN tunnel junction for blue light emitting diode applications." Applied Physics Letters **110** (2017), no. 10 102104.

[38] T. Margalith, O. Buchinsky, D. A. Cohen, A. C. Abare, M. Hansen, S. P. DenBaars, and L. A. Coldren, "Indium tin oxide contacts to gallium nitride optoelectronic devices." Applied Physics Letters **74** (1999), no. 26 3930–3932.

[39] S. Lee, C. A. Forman, C. Lee, J. Kearns, E. C. Young, J. T. Leonard, D. A. Cohen, J. S. Speck, S. Nakamura, and S. P. DenBaars, "GaN-based vertical-cavity surface-emitting lasers with tunnel junction contacts grown by metal-organic chemical vapor deposition." Applied Physics Express **11** (2018), no. 6 062703.

[40] B. P. Yonkee, R. M. Farrell, J. T. Leonard, S. P. DenBaars, J. S. Speck, and S. Nakamura, "Demonstration of low resistance ohmic contacts to p-type (20-2-1) GaN." Semiconductor Science and Technology **30** (2015), no. 7 075007.

[41] B. P. Yonkee, E. C. Young, S. P. DenBaars, J. S. Speck, and S. Nakamura, "High reflectivity ohmic contacts to n-GaN utilizing vacuum annealed aluminum." Semiconductor Science and Technology **33** (2017), no. 1 015015.

[42] J. Neugebauer and C. G. Van de Walle, "Role of hydrogen in doping of GaN." Applied Physics Letters **68** (1996), no. 13 1829–1831.

[43] A. Dussaigne, B. Damilano, J. Brault, J. Massies, E. Feltin, and N. Grandjean, "High doping level in Mg-doped GaN layers grown at low temperature." Journal of Applied Physics **103** (2008), no. 1 013110.

[44] C. A. Hurni, J. R. Lang, P. G. Burke, and J. S. Speck, "Effects of growth temperature on Mg-doped GaN grown by ammonia molecular beam epitaxy." Applied Physics Letters **101** (2012), no. 10 102106.

[45] Y. Kato, K. Miyoshi, T. Takeuchi, T. Inagaki, M. Iwaya, S. Kamiyama, and I. Akasaki, "Low threshold current density in GaInN-based laser diodes with GaN tunnel junctions." Applied Physics Express **14** (2021) 061002.

[46] P. Li, H. Zhang, H. Li, M. Iza, Y. Yao, M. S. Wong, N. Palmquist, J. S. Speck, S. Nakamura, and S. P. DenBaars, "Size-independent low voltage of InGaN micro-light-emitting diodes with epitaxial tunnel junctions using selective area growth by metalorganic chemical vapor deposition." Opt. Express **28** (2020), no. 13 18707–18712.

[47] P. Li, H. Zhang, H. Li, Y. Zhang, Y. Yao, N. Palmquist, M. Iza, J. S. Speck, S. Nakamura, and S. P. DenBaars, "Metalorganic chemical vapor deposition grown n-InGaN/n-GaN tunnel junctions for micro-light-emitting diodes with very low forward voltage." Semiconductor Science and Technology **35** (2020), no. 12 125023.

[48] M. S. Wong, J. Back, D. Hwang, C. Lee, J. Wang, S. Gandrothula, T. Margalith, J. S. Speck, S. Nakamura, and S. P. DenBaars, "Demonstration of high wall-plug efficiency III-nitride micro-light-emitting diodes with MOCVD-grown tunnel junction contacts using chemical treatments." Applied Physics Express **14** (2021), no. 8 086502.

[49] U. K. Mishra and J. Singh, Semiconductor device physics and design. Springer, 2008.

[50] A. Agarwal, M. Tahhan, T. Mates, S. Keller, and U. Mishra, "Suppression of Mg propagation into subsequent layers grown by MOCVD." Journal of Applied Physics **121** (2017), no. 2 025106.

[51] A. Agarwal, C. Gupta, A. Alhassan, T. Mates, S. Keller, and U. Mishra, "Abrupt GaN/p-GaN:Mg junctions grown via metalorganic chemical vapor deposition." Applied Physics Express **10** (2017), no. 11 111002.

[52] N. Kuroda, C. Sasaoka, A. Kimura, A. Usui, and Y. Mochizuki, "Precise control of pn-junction profiles for GaN-based LD structures using GaN substrates with low dislocation densities." Journal of Crystal Growth **189-190** (1998) 551–555.

[53] J. Chen, W. Yi, T. Kimura, S. Takashima, M. Edo, and T. Sekiguchi, "Cathodoluminescene study of Mg implanted GaN: the impact of dislocation on Mg diffusion." Applied Physics Express **12** (2019), no. 5 051010.

[54] H. Xing, D. S. Green, H. Yu, T. Mates, P. Kozodoy, S. Keller, S. P. DenBaars, and U. K. Mishra, "Memory effect and redistribution of Mg into sequentially regrown GaN layer by metalorganic chemical vapor deposition." Japanese Journal of Applied Physics **42** (2003), no. Part 1, No. 1 50–53.

[55] M. Khoury, H. Li, H. Zhang, B. Bonef, M. S. Wong, F. Wu, D. Cohen, P. De Mierry, P. Vennéguès, J. S. Speck, S. Nakamura, and S. P. DenBaars, "Demonstration of electrically injected semipolar laser diodes grown on low-cost and scalable sapphire substrates." ACS Applied Materials & Interfaces **11** (2019), no. 50 47106–47111. PMID: 31769651.

[56] C. Moe, T. Onuma, K. Vampola, N. Fellows, H. Masui, S. Newman, S. Keller, S. Chichibu, S. DenBaars, and D. Emerson, "Increased power from deep ultraviolet LEDs via precursor selection." Journal of Crystal Growth **298** (2007) 710–713. Thirteenth International Conference on Metal Organic Vapor Phase Epitaxy (ICMOVPE XIII).

[57] B. E. Warren, X-Ray Diffraction. Dover Publications, 1990.

[58] PANalytical B.V., "Epitaxy 4.3." http://www.photond.com, 2010.

[59] D. F. Feezell, J. S. Speck, S. P. DenBaars, and S. Nakamura, "Semipolar (20-2-1) InGaN/GaN light-emitting diodes for high-efficiency solid-state lighting." J. Display Technol. **9** (2013), no. 4 190–198.

[60] T. Melo, Y.-L. Hu, C. Weisbuch, M. C. Schmidt, A. David, B. Ellis, C. Poblenz, Y.-D. Lin, M. R. Krames, and J. W. Raring, "Gain comparison in polar and nonpolar/ semipolar gallium-nitride-based laser diodes." Semiconductor Science and Technology **27** (2012), no. 2.

[61] W. G. Scheibenzuber, U. T. Schwarz, R. G. Veprek, B. Witzigmann, and A. Hangleiter, "Calculation of optical eigenmodes and gain in semipolar and nonpolar InGaN/GaN laser diodes." Phys. Rev. B **80** (2009) 115320.

[62] S. A. Campbell, Fabrication Engineering at the Micro and Nanoscale. Oxford University Press, 2013.

[63] D. L. Becerra, L. Y. Kuritzky, J. Nedy, A. Saud Abbas, A. Pourhashemi, R. M. Farrell, D. A. Cohen, S. P. DenBaars, J. S. Speck, and S. Nakamura, "Measurement and analysis of internal loss and injection efficiency for continuous-wave blue semipolar (20-2-1) III-nitride laser diodes with chemically assisted ion beam etched facets." Applied Physics Letters **108** (2016), no. 9 091106.

[64] P. S. Hsu, R. M. Farrell, J. J. Weaver, K. Fujito, S. P. DenBaars, J. S. Speck, and S. Nakamura, "Comparison of polished and dry etched semipolar (11-22) III-nitride laser facets." IEEE Photonics Technology Letters **25** (2013), no. 21 2105–2107.

[65] M. Kato, K. Mikamo, M. Ichimura, M. Kanechika, O. Ishiguro, and T. Kachi, "Characterization of plasma etching damage on p-type GaN using schottky diodes." Journal of Applied Physics **103** (2008), no. 9 093701.

[66] X. A. Cao, A. P. Zhang, G. T. Dang, F. Ren, S. J. Pearton, R. J. Shul, and L. Zhang, "Schottky diode measurements of dry etch damage in n- and p-type GaN." Journal of Vacuum Science & Technology A **18** (2000), no. 4 1144–1148.

[67] T. Yajima and L. Esaki, "Excess noise in narrow germanium p-n junctions." Journal of the Physical Society of Japan **13** (1958), no. 11 1281–1287.

[68] S.-R. Jeon, Y.-H. Song, H.-J. Jang, G. M. Yang, S. W. Hwang, and S. J. Son, "Lateral current spreading in GaN-based light-emitting diodes utilizing tunnel contact junctions." Applied Physics Letters **78** (2001), no. 21 3265–3267.

[69] T. Takeuchi, G. Hasnain, S. Corzine, M. Hueschen, J. Richard P. Schneider, C. Kocot, M. Blomqvist, Y. lan Chang, D. Lefforge, M. R. Krames, L. W. Cook, and S. A. Stockman, "GaN-based light emitting diodes with tunnel junctions.".

[70] I. Ozden, E. Makarona, A. V. Nurmikko, T. Takeuchi, and M. Krames, "A dual-wavelength indium gallium nitride quantum well light emitting diode." Applied Physics Letters **79** (2001), no. 16 2532–2534.

[71] M. J. Grundmann and U. K. Mishra, "Multi-color light emitting diode using polarization-induced tunnel junctions." physica status solidi c **4** (2007), no. 7 2830–2833.

[72] J. Simon, Z. Zhang, K. Goodman, H. Xing, T. Kosel, P. Fay, and D. Jena, "Polarization-induced zener tunnel junctions in wide-band-gap heterostructures." Phys. Rev. Lett. **103** (2009) 026801.

[73] S. Krishnamoorthy, D. N. Nath, F. Akyol, P. S. Park, M. Esposto, and S. Rajan, "Polarization-engineered GaN/InGaN/GaN tunnel diodes." Applied Physics Letters **97** (2010), no. 20 203502.

[74] S. Krishnamoorthy, P. S. Park, and S. Rajan, "Demonstration of forward inter-band tunneling in GaN by polarization engineering." Applied Physics Letters **99** (2011), no. 23 233504.

[75] S. Krishnamoorthy, F. Akyol, P. S. Park, and S. Rajan, "Low resistance GaN/InGaN/GaN tunnel junctions." Applied Physics Letters **102** (2013), no. 11 113503.

[76] S. Krishnamoorthy, F. Akyol, and S. Rajan, "InGaN/GaN tunnel junctions for hole injection in GaN light emitting diodes." Applied Physics Letters **105** (2014), no. 14 141104.

[77] Z.-H. Zhang, S. Tiam Tan, Z. Kyaw, Y. Ji, W. Liu, Z. Ju, N. Hasanov, X. Wei Sun, and H. Volkan Demir, "InGaN/GaN light-emitting diode with a polarization tunnel junction." Applied Physics Letters **102** (2013), no. 19 193508.

[78] A. J. Mughal, E. C. Young, A. I. Alhassan, J. Back, S. Nakamura, J. S. Speck, and S. P. DenBaars, "Polarization-enhanced InGaN/GaN-based hybrid tunnel junction contacts to GaN p-n diodes and InGaN LEDs." Applied Physics Express **10** (2017), no. 12 121006.

[79] M. Kaga, T. Morita, Y. Kuwano, K. Yamashita, K. Yagi, M. Iwaya, T. Takeuchi, S. Kamiyama, and I. Akasaki, "GaInN-based tunnel junctions in n-p-n light emitting diodes." Japanese Journal of Applied Physics **52** (2013), no. 8S 08JH06.

[80] D. Minamikawa, M. Ino, S. Kawai, T. Takeuchi, S. Kamiyama, M. Iwaya, and I. Akasaki, "GaInN-based tunnel junctions with high InN mole fractions grown by MOVPE." physica status solidi (b) **252** (2015), no. 5 1127–1131.

[81] D. Takasuka, Y. Akatsuka, M. Ino, N. Koide, T. Takeuchi, M. Iwaya, S. Kamiyama, and I. Akasaki, "GaInN-based tunnel junctions with graded layers." Applied Physics Express **9** (2016), no. 8 081005.

[82] J. Wang, E. C. Young, W. Y. Ho, B. Bonef, T. Margalith, and J. S. Speck, "III-nitride blue light-emitting diodes utilizing hybrid tunnel junction with low excess voltage." Semiconductor Science and Technology **35** (2020), no. 12 125026.

[83] E. Young, B. Yonkee, F. Wu, S. Oh, S. Denbaars, S. Nakamura, and J. Speck, "Hybrid tunnel junction contacts to III–nitride light-emitting diodes." Applied Physics Express **9** (2016).

[84] A. I. Alhassan, E. C. Young, A. Y. Alyamani, A. Albadri, S. Nakamura, S. P. DenBaars, and J. S. Speck, "Reduced-droop green III-nitride light-emitting diodes utilizing GaN tunnel junction." Applied Physics Express **11** (2018), no. 4 042101.

[85] J. Wang, E. Young, B. SaifAddin, C. Zollner, A. Almogbel, M. Fireman, M. Izza, S. Nakamura, S. Denbaars, and J. Speck, *Hybrid III-nitride tunnel junctions for low excess voltage blue LEDs and UVC LEDs*, in 2019 Compound Semiconductor Week (CSW), 2019.

[86] C. A. Forman, S. Lee, E. C. Young, J. A. Kearns, D. A. Cohen, J. T. Leonard, T. Margalith, S. P. DenBaars, and S. Nakamura, "Continuous-wave operation of m-plane GaN-based vertical-cavity surface-emitting lasers with a tunnel junction intracavity contact." Applied Physics Letters **112** (2018), no. 11 111106.

[87] S. J. Kowsz, E. C. Young, B. P. Yonkee, C. D. Pynn, R. M. Farrell, J. S. Speck, S. P. DenBaars, and S. Nakamura, "Using tunnel junctions to grow monolithically integrated optically pumped semipolar III-nitride yellow quantum wells on top of electrically injected blue quantum wells." Opt. Express **25** (2017), no. 4 3841–3849.

[88] A. C. Espenlaub, D. J. Myers, E. C. Young, S. Marcinkevičius, C. Weisbuch, and J. S. Speck, "Evidence of trap-assisted auger recombination in low radiative efficiency MBE-grown III-nitride LEDs." Journal of Applied Physics **126** (2019), no. 18 184502.

[89] Y. Zhang, A. A. Allerman, S. Krishnamoorthy, F. Akyol, M. W. Moseley, A. M. Armstrong, and S. Rajan, "Enhanced light extraction in tunnel junction-enabled top emitting UV LEDs." Applied Physics Express **9** (2016), no. 5 052102.

[90] Y. Zhang, S. Krishnamoorthy, F. Akyol, S. Bajaj, A. A. Allerman, M. W. Moseley, A. M. Armstrong, and S. Rajan, "Tunnel-injected sub-260 nm ultraviolet light emitting diodes." Applied Physics Letters **110** (2017), no. 20 201102.

[91] C. A. Hurni, A. David, M. J. Cich, R. I. Aldaz, B. Ellis, K. Huang, A. Tyagi, R. A. DeLille, M. D. Craven, F. M. Steranka, and M. R. Krames, "Bulk GaN flip-chip violet light-emitting diodes with optimized efficiency for high-power operation." Applied Physics Letters **106** (2015), no. 3 031101.

[92] S. Mehari, D. A. Cohen, D. L. Becerra, S. Nakamura, and S. P. DenBaars, “Demonstration of enhanced continuous-wave operation of blue laser diodes on a semipolar (202¯1¯) GaN substrate using indium-tin-oxide/thin-p-GaN cladding layers.” Opt. Express **26** (2018), no. 2 1564–1572.

[93] A. Myzaferi, A. H. Reading, D. A. Cohen, R. M. Farrell, S. Nakamura, J. S. Speck, and S. P. DenBaars, “Transparent conducting oxide clad limited area epitaxy semipolar III-nitride laser diodes.” Applied Physics Letters **109** (2016), no. 6 061109.

[94] M. T. Hardy, C. O. Holder, D. F. Feezell, S. Nakamura, J. S. Speck, D. A. Cohen, and S. P. DenBaars, “Indium-tin-oxide clad blue and true green semipolar InGaN/GaN laser diodes.” Applied Physics Letters **103** (2013), no. 8 081103.

[95] V. Savona, *Linear optical properties of semiconductor microcavities with embedded quantum wells*, in Confined Photon Systems: Fundamentals and Applications (H. Benisty, J. Gerard, R. Houdre, J. Rarity, and C. Weisbuch, eds.), ch. 5, pp. 173–182. Springer Berlin Heidelberg, 1999.

[96] B. E. A. Saleh and M. C. Teich, Ray Optics, ch. 1, pp. 1–40. John Wiley & Sons, Ltd, 1991.

[97] J. G. Nedy, Dry-etched features for advanced waveguide design in GaN laser diodes. PhD thesis, University of California, Santa Barbara, 2016.

[98] M. Grundmann, *Interactive 1-D Poisson-Schrödinger solver BANDENG, University of California at Santa Barbara, Santa Barbara, California*, 2004.

[99] A. Pourhashemi, R. M. Farrell, D. A. Cohen, J. S. Speck, S. P. DenBaars, and S. Nakamura, “High-power blue laser diodes with indium tin oxide cladding on semipolar (20-2-1) GaN substrates.” Applied Physics Letters **106** (2015), no. 11 111105.

[100] P. Kozodoy, H. Xing, S. P. DenBaars, U. K. Mishra, A. Saxler, R. Perrin, S. Elhamri, and W. C. Mitchel, “Heavy doping effects in Mg-doped GaN.” Journal of Applied Physics **87** (2000), no. 4 1832–1835.

[101] H. Kogelnik and C. V. Shank, “Coupled-wave theory of distributed feedback lasers.” Journal of Applied Physics **43** (1972), no. 5 2327–2335.

[102] S. Masui, K. Tsukayama, T. Yanamoto, T. Kozaki, S. ichi Nagahama, and T. Mukai, “CW operation of the first-order AlInGaN 405 nm distributed feedback laser diodes.” Japanese Journal of Applied Physics **45** (2006), no. No. 46 L1223–L1225.

[103] H. Zhang, D. A. Cohen, P. Chan, M. S. Wong, S. Mehari, D. L. Becerra, S. Nakamura, and S. P. DenBaars, "Continuous-wave operation of a semipolar InGaN distributed-feedback blue laser diode with a first-order indium tin oxide surface grating." Opt. Lett. **44** (2019), no. 12 3106–3109.

[104] H. Zhang, D. A. Cohen, P. Chan, M. S. Wong, P. Li, H. Li, S. Nakamura, and S. P. Denbaars, "High performance of a semipolar InGaN laser with a phase-shifted embedded hydrogen silsesquioxane (HSQ) grating." Opt. Lett. **45** (2020), no. 20 5844–5847.

[105] T. J. Slight, A. Yadav, O. Odedina, W. Meredith, K. E. Docherty, E. Rafailov, and A. E. Kelly, "InGaN/GaN laser diodes with high order notched gratings." IEEE Photonics Technology Letters **29** (2017), no. 23 2020–2022.

[106] J. A. Holguín-Lerma, T. K. Ng, and B. S. Ooi, "Narrow-line InGaN/GaN green laser diode with high-order distributed-feedback surface grating." Applied Physics Express **12** (2019), no. 4 042007.

[107] A. Laakso, M. Dumitrescu, J. Viheriälä, J. Karinen, M. Suominen, and M. Pessa, "Optical modeling of laterally-corrugated ridge-waveguide gratings." Optical and Quantum Electronics **40** (2008), no. 11 907–920.

[108] G. Morthier, P. Vankwikelberge, K. David, and R. Baets, "Improved performance of AR-coated DFB lasers for the introduction of gain coupling." IEEE Photonics Technology Letters **2** (1990), no. 3 170–172.

[109] W. Tsang, F. Choa, M. Wu, Y. Chen, R. Logan, A. Sergent, and C. Burrus, "Long-wavelength InGaAsP/InP distributed feedback lasers incorporating gain-coupled mechanism." IEEE Photonics Technology Letters **4** (1992), no. 3 212–215.

[110] W. T. Tsang, F. S. Choa, M. C. Wu, Y. K. Chen, R. A. Logan, S. N. G. Chu, A. M. Sergent, and C. A. Burrus, "Semiconductor distributed feedback lasers with quantum well or superlattice gratings for index or gain-coupled optical feedback." Applied Physics Letters **60** (1992), no. 21 2580–2582.

[111] Photon Design Ltd., "FIMMWAVE 6.6." http://www.photond.com, 2018.

[112] Z. Li, J. Liu, M. Feng, K. Zhou, S. Zhang, H. Wang, D. Li, L. Zhang, D. Zhao, D. Jiang, H. Wang, and H. Yang, "Suppression of thermal degradation of InGaN/GaN quantum wells in green laser diode structures during the epitaxial growth." Applied Physics Letters **103** (2013), no. 15 152109.

[113] Y.-T. Moon, D.-J. Kim, K.-M. Song, C.-J. Choi, S.-H. Han, T.-Y. Seong, and S.-J. Park, "Effects of thermal and hydrogen treatment on indium segregation in

InGaN/GaN multiple quantum wells." Journal of Applied Physics **89** (2001), no. 11 6514–6518.

[114] S. Okawara, Y. Aoki, M. Kuwabara, Y. Takagi, J. Maeda, and H. Yoshida, "Nitride-based stacked laser diodes with a tunnel junction." Applied Physics Express **11** (2017), no. 1 012701.

[115] D. L. Becerra, High Power High Efficiency Semipolar InGaN Light Emitting Devices for Solid State Lighting. PhD thesis, University of California, Santa Barbara, 2016.

[116] R. M. Farrell, Growth, Fabrication, and Characterization of Continuous-Wave Aluminum Gallium Nitride-Cladding-Free m-plane Indium Gallium Nitride / Gallium Nitride Laser Diodes. PhD thesis, University of California, Santa Barbara, 2010.